

Studying the Altered Reactivity of Electrochemical Systems in Room Temperature Ionic Liquids

Sven Ernst

St John's College

DPhil Thesis

Physical and Theoretical Chemistry

University of Oxford

Michaelmas Term 2013

Abstract

The work presented in this thesis examines the electrochemical behaviour of a number of species, both surface-bound and in the solution phase, in various room-temperature ionic liquids (RTILs), in order to identify systems which show altered reactivities in room-temperature ionic liquids, compared to that in conventional, molecular, aprotic solvents. The fundamentals of electrochemistry are outlined and an introduction to room-temperature ionic liquids is given, after which the results of six original investigations are presented, as follows;

- The electrochemical response of surface-bound anthraquinonyl films was investigated as a function of RTIL cation size.
- The reduction of oxygen to superoxide in the $[C_2mim][NTf_2]$ RTIL was studied at different carbon electrodes.
- The mechanisms of electrodeposition and stripping of Zn(II) onto bulk zinc deposits, on glassy carbon electrodes, in the $[C_4mPyrr][NTf_2]$ RTIL were investigated.
- A novel and successful method for the fabrication of zinc microdisk electrodes was developed and the electrochemical behaviour of these electrodes was investigated.
- The mechanisms for the electrochemical reductions of some bromo- and nitro-benzenes at platinum microelectrodes were determined in the $[C_4mPyrr][NTf_2]$

ionic liquid, in order to identify systems which displayed changed reactivities in RTILs compared to those in molecular aprotic solvents.

- The altered reactivity of 1-bromo-4-nitrobenzene in the $[C_4mPyrr][NTf_2]$ ionic liquid was utilised *via* electrochemical reduction at zinc microelectrodes in order to form arylzinc compounds.

The work presented in this thesis shows that the oft-taken view that the reactivity of a given species in an ionic liquid will mimic that in conventional aprotic solvents is not always the case. Reactivities can be markedly different between RTILs and aprotic solvents and can also be highly dependent on the specific ionic liquid employed.

Acknowledgements

First and foremost I would like to thank my supervisor, Professor Richard G. Compton for welcoming me into his group and for his continued guidance these last three years. I feel very privileged for my time in the group, at St John's and in Oxford in general, none of which I would have been able to experience if it wasn't for him.

I would also like to thank all of the post-docs in the group, past and present, and in particular Dr Leigh Aldous, who helped supervise me in my first year and Dr Chris Batchelor-McAuley, who has always been happy to help me with work matters and with a few pints thereafter. Also to Ben and Lin, who I had the pleasure of supervising and who provided many "tin-foil hat" moments.

I would also like to thank my collaborators, Professor Chris Hardacre and Dr Sarah Norman for synthesising all of the ionic liquids I required, and also Kris Ward for writing the simulation program I needed. Furthermore, I would like to thank former group-member Debbie Silvester-Dean for convincing me to apply to Oxford in the first place. In addition, I would like to thank all of the members in the group who I've had the great pleasure of working with.

Finally, I would like to say a big thankyou to my parents and brother for all of their encouragement and support, and also to all of my friends at St John's and in general who have made my time here so memorable.

Table of Contents

Abstract ..... **i**

Acknowledgements ..... **iii**

Table of Contents ..... **iv**

Glossary ..... **ix**

1. Introduction to Electrochemistry **1**

1.1 Equilibrium Electrochemistry 1

1.2 Dynamic Electrochemistry 3

1.2.1 Faradaic Processes 4

1.2.2 Non-Faradaic Processes 5

1.2.3 The Electrical Double Layer 6

1.2.4 Adsorption and Desorption Processes 8

1.3 Mass Transport 9

1.3.1 Diffusion 9

1.3.2 Convection 11

1.3.3 Migration 12

1.4 Heterogeneous Electron Transfer 13

1.4.1 The Butler-Volmer Model 14

1.4.2 Electrochemical Reversibility 15

1.4.3 The Tafel Law 17

1.4.4 Multi-Step Electron Transfer....18

1.5 Homogeneous Processes....20

1.5.1 EC Mechanism....20

1.5.2 ECE Mechanism....21

1.5.3 DISP Mechanism....22

1.6 Electrochemical Cells....23

1.6.1 Microelectrodes....24

1.6.2 Reference Electrodes....27

1.6.3 Counter Electrodes....28

1.7 Electrochemical Techniques....28

1.7.1 Potential Step Chronoamperometry....29

1.7.2 Cyclic Voltammetry....30

1.7.3 Modelling Electrochemical Processes....35

References....36

2. Introduction to Room Temperature Ionic Liquids....38

2.1 Introduction....38

2.2 Synthesis of RTILs....40

2.3 Properties of RTILs....41

2.3.1 Viscosity....41

2.3.2 Density....42

2.3.3 Conductivity 42

2.3.4 Electrochemical Window 43

2.3.5 Melting Points, Thermal Stability and Volatility 44

2.4 The Effects of Impurities 46

2.4.1 Water 47

2.4.2 Halides and Other Unreacted Starting Materials 47

2.4.3 Dissolved Gasses 48

2.5 Fundamental Electrochemistry in RTILs 49

2.5.1 Mass Transport 49

2.5.2 Electron Transfer Kinetics 51

2.5.3 The Electrochemical Double Layer 53

References 56

3. Experimental Methods 62

3.1 Chemical Reagents 62

3.2. Instrumentation and electrodes 66

3.3 Apparatus 68

3.4 Chronoamperometric Experiments 71

References 72

4. Influence of Cation Size on Voltammetry in RTILs 73

4.1 Introduction 74

4.2 Experimental 76

4.3 Results and Discussion 77

4.4 Conclusions 89

References 90

5. Oxygen Reduction in RTILs at Different Electrodes 93

5.1 Introduction 93

5.2 Experimental 96

5.3 Results and Discussion 97

5.4 Conclusions 108

References 109

6. Electrodeposition and Stripping of Zn(II) in $[C_4mPyrr][NTf_2]$ 112

6.1 Introduction 112

6.2 Experimental 117

6.3 Results and Discussion 117

6.4 Conclusions 124

References 125

7. Fabrication of Zinc Microelectrodes 127

7.1 Introduction 127

7.2 Experimental 128

7.3 Voltammetry of Zinc Microelectrodes in Aqueous KOH Solutions 130

7.4 Voltammetry of Zinc Microelectrodes in ionic liquids 132

7.5 Conclusions 135

References 136

8. Reduction of 1-Bromo-4-nitrobenzene at Platinum Microelectrodes: Probing Altered Reactivity in Room-Temperature Ionic Liquids 137

8.1 Introduction 137

8.2 Experimental 139

8.3 Results and Discussion 141

8.4 Conclusions 157

References 158

9. Reduction of 1-Bromo-4-nitrobenzene at Zinc Microelectrodes: Utilising the Changed Reactivity of 1-Bromo-4-nitrobenzene in RTILs to Form Arylzincs ... 161

9.1 Introduction 161

9.2 Experimental 163

9.3 Results and Discussion 165

9.4 Conclusions 172

References 173

Overall Conclusions 175

Appendix 179

Derivation of Fick's Laws 179

Derivation of the Nernst Equation 182

Derivation of the Butler-Volmer Equation 184

Glossary

Table 1 - List of symbols commonly used throughout this thesis.

Symbol	Definition
α	cathodic electron transfer coefficient
β	anodic electron transfer coefficient
δ	diffusion layer thickness
ΔE_{pp}	peak-to-peak separation
ΔG	Gibb's energy
ΔG°	standard Gibb's energy
δt	time interval
δx^2	mean square distance
ϕ	electric field function
Γ	surface coverage
γ_j	activity coefficient of species j
η	solvent viscosity
η_∞	hypothetical viscosity at infinite temperature
Λ	Matsuda and Ayabe parameter
∇^2	Laplacian operator
τ	dimensionless time
υ	scan rate
[A]	concentration of species A
[B]	concentration of species B
A	electrode area
A	reactant species
a_j	activity of species j
B	product species

c	concentration
C	homogeneous reaction product
C_{d}	double layer capacitance
D	diffusion coefficient
D_{∞}	hypothetical diffusion coefficient at infinite temperature
E	potential
e^{-}	electron
E°	standard electrode potential
E°_{RDS}	formal potential of RDS
E_1	starting potential
$E_{1/2}$	half-wave potential
E_2	final or switching potential
$E_{a,D}$	activation energy of diffusion
E_{eq}	equilibrium potential
E_f°	formal potential
E_{η}	activation energy for viscous flow
E_{p}	peak potential
F	Faraday constant (96485 C mol^{-1})
$f(\ )$	function of
i	current
i_0	exchange current
i_{C}	charging/capacitative current
i_{d}	diffusion limited current
i_{p}	peak current
i_{ss}	steady-state current
j	flux
j_{c}	convective flux
j_{d}	diffusive flux
j_{m}	migratory flux
k°	standard electrochemical rate constant

k°_{RDS}	standard electrochemical rate constant of RDS
k_{b}	backward rate constant
k_{B}	Boltzmann constant
k_f	forward rate constant
m	number of moles of substance
m_{T}	mass transport coefficient
n	number of electrons or a real integer > 0
N	number of moles
n'	number of electrons transferred prior to RDS
n''	number of electrons transferred after RDS
p	constant
P	pressure
q	charge passed
Q	total charge or reaction quotient
R	universal gas constant
r	electrode radius or radial coordinate
r_h	hydrodynamic radius
R_{s}	solution resistance
T	absolute temperature
t	time
T_0	ideal gas temperature of zero conductivity
u	mobility
$v(x)$	velocity in the x direction
W	electrical work
x	distance or direction
X	halide species
$x(t)$	time dependent position in x
x_0	initial position in x
z	ionic charge or length coordinate

Table 2 - List of units commonly used throughout this thesis.

Unit	Definition
°C	degrees centigrade
µL	microlitre
µm	micrometre
Å	angstrom
C	Coulomb
cm	centimetre
cP	centipoise
g	gram
K	Kelvin
m	metre
M	molar
mbar	millibar
min	minutes
mL	millilitre
mM	millimolar
mm	millimetre
mol	mole
mV	millivolts
MΩ	megaohms
s	second
V	volts
Ω	ohms

Table 3 - List of abbreviations commonly used throughout this thesis.

Abbreviation	Definition
AQ	9,10-anthraquinone
AQ_L	2-anthraquinonyl group
BDD	boron-doped diamond
CE	counter electrode
CPET	concerted proton and electron transfer
CV	cyclic voltammogram
DMF	*N,N*-dimethylformamide
DMSO	dimethylsulfoxide
DOS	density of electronic states
EtOH	ethanol
Fc	ferrocene
FFT	fast fourier transform
GC	glassy carbon
GCS	Gouy-Chapman-Stern double layer model
GPES	general purpose electrochemical suite
HOPG	highly-ordered pyrolytic graphite
IHP	inner Helmholtz plane
MeCN	acetonitrile
OHP	outer Helmholtz plane
PID	proportional-integral-derivative
PTFE	polytetrafluoroethylene
PZC	point of zero charge
RDS	rate determining step
RE	reference electrode
RTIL	room temperature ionic liquid
WE	working electrode

1. Introduction to Electrochemistry

This chapter introduces the basic fundamental concepts of electrochemistry and the electrochemical techniques used throughout this thesis. The description provided herein is by no means exhaustive and thus the reader is directed towards several excellent textbooks for a more thorough introduction[1-7].

Electrochemistry, in a broad sense, is the study of the interrelation of electrical and chemical effects. The field primarily deals with the study of chemical changes in a system resultant from the passage of an electrical current, or the production of an electrical current *via* a chemical reaction. The former may involve examining the properties of an analyte by probing its response to an electrical current, or inducing chemical reactions as a result of passing an electrical current. Measuring the current response as a function of the potential applied across a solution, between electrodes, allows for the extraction of a wealth of information on both the kinetics and thermodynamics of the species under study, as shown below.

1.1 Equilibrium Electrochemistry

Equilibrium electrochemistry considers the formation of a chemical equilibrium between an electrode (usually, but not necessarily, a metal) and an electrolyte, without the passage of a sustained current, when a potential difference is established. Thus, for the electrode reaction;

$$\mathrm{A} + n\mathrm{e}^- \rightleftharpoons \mathrm{B} \tag{1.1}$$

involving species A and B in solution as well as n electrons in the electrode, an equilibrium will be established at the electrode surface. Once this dynamic equilibrium has been established, the number of electrons passing from the electrode to species A is, by definition, exactly equal to that passing from species B to the electrode. As this equilibrium involves both the electrode and the two species in the solution phase, there will be a net separation of charge between the two phases, which then gives rise to a potential difference across the phases. It should be noted at this point that the kinetics of (1.1) must be fast enough to develop an equilibrium within the timescale of the experiment, which is crucial in identifying redox couples which are suitable for use in reference electrodes[8]. The equilibrium potential established in (1.1) is dependent on the concentrations of A and B and is predicted by the Nernst equation;

$$E_{\text{eq}} = E^{\circ} + \frac{RT}{nF}\ln\left(\frac{a_{\text{A}}}{a_{\text{B}}}\right) \tag{1.2}$$

where E_{eq} is the equilibrium potential, E° the standard electrode potential, R the universal gas constant, T the temperature, n the number of electrons transferred, F is the Faraday constant and a_{A} and a_{B} are the activities of the species involved in the charge transfer reaction. However, under electrolytic conditions, (1.2) is better expressed in terms of the surface concentrations [A] and [B] in conjunction with the formal potential, E_f°, such that;

$$E_{\text{eq}} = E_f^{\circ} + \frac{RT}{nF}\ln\left(\frac{[\text{A}]}{[\text{B}]}\right) \tag{1.3}$$

The driving force behind the establishment of the equilibrium in (1.1) is based on the difference in energy levels between the electrode and the solution phase species. The energy levels of the ions in solution are discrete, while the electronic structure of a metal electrode consists of a continuum of energy levels, in conduction bands, up to a maximum at the Fermi level. It is thus energetically favourable for electrons to pass from which ever species has the highest energy level, be it from a discrete solution phase species or the electrode, to one with a lower energy level. This is the driving force behind the establishment of the equilibrium and when reached, the highest occupied band in the electrode has an energy intermediate to those of the two solution phase species. Thus, the rate of electron transfer *from* the electrode to one solution phase species is exactly matched by the rate of electron transfer *to* the electrode from the other and the equilibrium is maintained.

1.2 Dynamic Electrochemistry

Dynamic electrochemistry regards the study of electron transfer reactions, at the electrode-electrolyte interface, resulting from an *applied* potential difference which causes an electrical current to flow. The mechanisms which cause an electrical current to flow in response to an applied potential can be grouped into two distinct categories; Faradaic processes and non-Faradaic processes.

1.2.1 Faradaic Processes

'Faradaic' or charge-transfer processes involve the transfer of electrons across the electrode-electrolyte interface; resulting in either the oxidation, if the energy of electrons in the solution phase species is higher than that in the electrode, or the reduction of the electroactive solution-phase species, for the converse situation. The amount of the electroactive species which is oxidised or reduced is described by Faraday's law, which states that the charge passed per mole of electrons transferred is equal to 96485 C mol^{-1} and is expressed as;

$$q = nFN \tag{1.4}$$

where q is the charge passed, n the number of electrons transferred per molecule, F is the Faraday constant (96485 C mol^{-1}) and N is the number of moles of the species being oxidised or reduced. However, Faraday's law assumes that all of the current which flows in response to an applied potential is of a 'Faradaic' nature, whereas in reality there are also non-Faradaic contributions to the current, which are described in the following section.

The extent to which a Faradaic current flows is dependent on both the kinetics of the electron transfer across the electrode-solution interface as well as the rates of mass transport to and from the electrode surface. Additionally, homogeneous reactions occurring either before or after a heterogeneous electron transfer step, or indeed between two such steps, will also impact on the magnitude of the Faradaic current. These aspects are explained in greater depth in their relevant sections.

1.2.2 Non-Faradaic Processes

A 'non-Faradaic' process is any process resulting in a flow of current which cannot be described by Faraday's law (1.4). These processes include adsorption and desorption at the electrode surface and changes to the electrode-solution interface that are potential dependant. In a non-Faradaic process, electronic charge does not actually cross the electrode to solution interface, although external currents can flow as a result of a changing potential, electrode area or solution composition.

The current resultant from a change in solution composition at the electrode to solution interface is commonly referred to as the 'charging' or 'capacitative' current, i_C, which arises from the reorganisation of ions in solution around the electrode in a region called the 'electrical double layer', which is described in the following section. The magnitude of the capacitative current as a function of time, for a potential step of magnitude E, is given by;

$$i_C = \frac{AE}{R_s} e^{-t/R_s C_d} \tag{1.5}$$

where A is the electrode area, R_s is the solution resistance, t is the time and C_d is the double-layer capacitance. The equivalent of (1.5) for a linear potential sweep experiment is given by;

$$i_C = Av C_d (1 - e^{-t/R_s C_d}) \tag{1.6}$$

which reaches a steady-state value of $Av C_{\mathrm{d}}$ at long times from which the double layer capacitance can be determined.

Generally, Faradaic currents are of primary interest in electrochemistry and hence modern potentiostats, covered in section 1.6, are designed to reduce non-Faradaic contributions to the overall current; however, they cannot be fully compensated for and must be kept in mind.

1.2.3 The Electrical Double Layer

As mentioned in the previous section, the electrical double layer is the region of ions in solution in a volume adjacent to the electrode surface. This region is necessary in order to balance the charge on the electrode which, if the electrode is sufficiently conducting, must reside on the surface as a result of Gauss's law[9]. The electrical double layer, as the name suggests, actually consists of two distinct layers; the 'compact' double layer and the 'diffuse' double layer.

The compact double layer refers to ions and molecules, both from the solvent and the species therein, which are specifically adsorbed on the electrode surface. The midpoint of these specifically adsorbed ions is described by a distance from the electrode surface referred to as the 'inner Helmholtz plane' (IHP). The distance of closest approach, again with respect to the midpoints, to the electrode for further solvated ions which are not specifically adsorbed is then termed the 'outer Helmholtz plane' (OHP). These two planes are named after Hermann von Helmholtz, who initially proposed a simple double layer model consisting only of the charge on the electrode and a counter-charge of ions at the electrode

surface[10, 11]. In the Helmholtz model, the potential is assumed to vary linearly across the adsorbed ions, from the value at the electrode to that of the bulk solution.

This model was later revised by Gouy[12, 13] and Chapman[14], who envisaged the ions as point charges and proposed the idea of a diffuse double layer. The diffuse double layer is a region of charged ions extending out into the bulk solution, where the density of charge decreases as a function of distance from the electrode, as the attractive electrostatic forces decrease in magnitude and thermal fluctuations become increasingly dominant. As a result, the potential drops approximately exponentially from the electrode surface into the solution, until the value for the bulk solution is reached.

Stern later improved upon this model further[15], by considering the ions not as point charges, but of finite dimension. Additionally, he amalgamated the Helmholtz model for the compact double layer with the Gouy-Chapman diffuse layer to create the model which is still most frequently used to this day. Additional refinements, relating largely to specific adsorption, have been proposed by Grahame[16] and Bockris *et al.*[17], however, the Gouy-Chapman-Stern (GCS) model is generally accepted to adequately describe the electrical double layer. In the GCS model, the potential varies linearly between the electrode and the OHP, after which it drops off approximately exponentially until the value of the bulk solution is reached.

1.2.4 Adsorption and Desorption Processes

As stated in the previous section, species in solution may be adsorbed at the electrode surface either 'specifically' or 'non-specifically'. The distinction between the two depends on the dominant force driving the attraction. Non-specifically adsorbed species are the result of long-range electrostatic forces altering the ionic composition near the surface, while specifically adsorbed species are resultant of a strong interaction between the adsorbed species or 'adsorbate' and the electrode surface. Both specifically and non-specifically adsorbed species can affect the electrochemical response of a system.

Non-specific adsorption of electroactive species changes the concentration of that species near the electrode, as well as influencing the potential profile in the area adjacent to the electrode. Specific adsorption of electroactive species on the electrode surface also alters the response due to concentration and potential distribution concerns, as well as potentially altering the energetics of the Faradaic process.

Specific adsorption of electroinactive species also alters the electrochemical response, as these species may form a blocking layer on the electrode, hence altering the accessible area, and/or alter the reactivity of electroactive species at the surface, *i.e.* in electrocatalytic systems. Specifically adsorbed species can also undergo 'desorption' at certain potentials and as a result it is quite common to employ one or more desorption potential steps before an electrochemical measurement in order to 'activate' or 're-activate' the electrode surface.

1.3 Mass Transport

In order for an electrode process to occur, the solution-phase species must first be transported from the bulk solution to the electrode surface. The means with which these species may reach the electrode can be divided into three distinct categories; diffusion, convection and migration, which are described below. However, it should first be mentioned that the overall flux, j, to the electrode surface is given by the summation of the diffusive flux, j_{d}, the convective flux, j_{c}, and the migratory flux, j_{m}.

1.3.1 Diffusion

Diffusion can be defined as the movement of a chemical species in response to a concentration gradient, which is effectively a gradient of chemical potential. It is this mode of mass transport which is most frequently encountered in electrochemical experiments, as whenever an electroactive species is depleted at the electrode a concentration gradient is formed. In fact, with the only exception being 'forced convection' (described in the following section), other modes of mass transport are actively discouraged in order to simplify the analysis of results. Diffusion is defined mathematically by Fick's laws, which are derived in the appendix. The diffusive flux, j_{d}, of material moving through a fixed volume in a direction, x, in response to an arbitrary concentration gradient at time, t. is given by Fick's first law;

$$j_{\mathrm{d}} = -D\frac{\partial c}{\partial x} \tag{1.7}$$

where c is the concentration as a function of x and D is the diffusion coefficient of the species, which is defined as;

$$D = \frac{\delta x^2}{2\delta t} \tag{1.8}$$

where δt represents the time interval in which the species moves a mean square distance (δx^2) and D describes the ease with which a given species can move though solution.

Fick's first law describes the flux as a function of distance, which in the case of electrochemistry is usually the distance from the electrode surface. However, Fick's first law does not describe the temporal variation of the flux, which is defined by Fick's second law;

$$\frac{\partial c}{\partial t} = D\frac{\partial^2 c}{\partial x^2} \tag{1.9}$$

which is described for a concentration gradient purely in the x direction. A more widely applicable version of (1.9), extended to three dimensions, is given by;

$$\frac{\partial c}{\partial t} = D \cdot \nabla^2 c \tag{1.10}$$

where ∇^2 is the Laplacian operator for the second differential and depends on the coordinate system used, being $(\partial^2/\partial x^2 + \partial^2/\partial y^2 + \partial^2/\partial z^2)$ for a Cartesian geometry. This equation, in conjunction with a vector operator appropriate for the given

coordinate system, can then be used to predict concentration changes around the electrode during an electrochemical experiment.

Furthermore, (1.9) can be used, in conjunction with the relevant boundary conditions, to derive the so-called 'Cottrell equation' for the diffusion limited current response, i_d, of an electroactive species as a function of time[18];

$$i_d = nFAc\sqrt{\frac{D}{\pi t}} \tag{1.11}$$

where c referrers to the concentration of the species in the bulk solution. This equation shows that, for a planar macroelectrode under planar diffusion, the current response to a potential step will eventually decay to zero proportional to the inverse square root of time.

1.3.2 Convection

Convection may be defined as the movement of a chemical species as a result of the hydrodynamic transport of the solution itself. Convection may be further broken down in to two separate cases; *natural* convection, such as that caused by density and thermal gradients, and *forced* convection, such as that imposed *via* the stirring or pumping of the solution or by gasses bubbling through solution. Natural convection is both undesirable, as the convective flux is difficult to separate from the diffusive flux, and difficult to predict. However, at short time-scales on the order of ten to twenty seconds, the effects are negligible[1].

Convection during an electrochemical experiment can otherwise be minimised by avoiding any stirring or pumping of solution and making efforts to prevent any

vibrations in the experimental setup. The convective flux, j_c, for a solution moving with a velocity $v(x)$ in the x direction is given by;

$$j_c = c \cdot v(x) \tag{1.12}$$

1.3.3 Migration

Migration can be defined as the movement of charged species in response to an electric field, which is a gradient of electric potential. In the bulk solution, during an electrochemical experiment, concentration gradients are small and thus the majority of the current is carried *via* migration[5]. Once a potential is applied to the electrode, a potential field is set up through the solution, inducing the migration of *all* charged species in the solution. The migratory flux, j_m, is thus defined (in the x direction) as[5];

$$j_m = -uc\frac{\partial \phi}{\partial x} \tag{1.13}$$

where c is the concentration, ϕ is the function for the electric field and u is the 'mobility' of the charged species, which is defined as the limiting velocity of the ion in an electric field of unit strength and is related to the diffusion coefficient *via* the Einstein-Smoluchowski equation[2];

$$u = \frac{|z|FD}{RT} \tag{1.14}$$

where z is the charge on the ion, F is the Faraday constant, R is the universal gas constant and T is the temperature.

As mentioned above, the effects of migration can be difficult to separate from those of diffusion and thus it is usually desirable to minimise migratory contributions to the flux. These contributions can be mitigated *via* the addition of an inert 'supporting electrolyte', present in much higher concentration than the species under study, such that the supporting electrolyte carries the vast majority of the migratory current. This supporting electrolyte may also have the added benefits of reducing the solution resistance, establishing the pH, ionic strength and ligand concentration of the solution, and ensuring that the double layer remains thin[2]. However, the addition of supporting electrolytes also involves several drawbacks such as increased ion-pairing, increased impurities (which may be electroactive), possible adsorption onto the electrode and the possibility of altering both kinetic and thermodynamic parameters[2].

1.4 Heterogeneous Electron Transfer

Having discussed the three principle modes of mass transfer in the previous section, this section now addresses the concept of heterogeneous electron transfer. The potential of an electrode strongly governs the reactions occurring at its surface and thus it is important to develop an understanding of the relationship of the electrode potential and the resulting Faradaic currents in terms of electron transfer kinetics.

1.4.1 The Butler-Volmer Model

The Butler-Volmer model of electron transfer kinetics is generally considered to be the most widely used interpretation of heterogeneous electron transfer kinetics. The model, proposed independently by Butler[19] and Volmer[20], is a predictive model based purely on classical, not microscopic, concepts. The theory thus has some limitations in that it cannot be used in a predictive manner, however, still provides valuable insight into reaction mechanisms.

In order to describe the Butler-Volmer equation (which is derived more fully in the Appendix), we first consider the following heterogeneous electron transfer reaction;

$$\mathrm{A} + \mathrm{e}^- \underset{k_b}{\overset{k_f}{\rightleftharpoons}} \mathrm{B} \tag{1.15}$$

where k_f and k_b represent the rate constants for the reduction and oxidation, respectively. It is intuitive from (1.15) that the net rate of reaction will be a summation of the rates of the forward and reverse reactions reaction and will be dependent on the surface concentrations [A] and [B]. As the net rate of reaction can also be described in terms of the electrons transferred we can state that;

$$\frac{i}{FA} = k_f[\mathrm{A}] - k_b[\mathrm{B}] \tag{1.16}$$

where i is the current, F is the Faraday constant and A is the electrode area. As shown in the appendix, the rate constants for the oxidation and reduction can be expressed as;

$$k_f = k^\circ \exp\left(-\frac{\alpha F}{RT}(E - E_f^\circ)\right) \tag{1.17}$$

$$k_b = k^\circ \exp\left(\frac{(1-\alpha)F}{RT}(E - E_f^\circ)\right) \tag{1.18}$$

where k° is the standard electrochemical rate constant, E is the potential and E_f° the formal potential (such that $(E - E^\circ)$ is the 'overpotential') and α is the transfer coefficient, which is a measure of the symmetry of the energy barrier for electron transfer[5]. The function for the current response in (1.16) is thus given by;

$$i = FAk^\circ\left([\mathrm{A}]\exp\left(-\frac{\alpha F}{RT}(E - E_f^\circ)\right) - [\mathrm{B}]\exp\left(\frac{(1-\alpha)F}{RT}(E - E_f^\circ)\right)\right) \tag{1.19}$$

which is the Butler-Volmer equation. This equation can then be combined with the equations for mass transport in order to model the current response of an electrochemical system, to extract the thermodynamic and kinetic parameters of an experimental measurement[1].

1.4.2 Electrochemical Reversibility

This section discusses the relationship of the relative rates of heterogeneous electron transfer and mass transport to the overall rate of reaction. In order to compare the rate constant for electron transport, k°, to that of mass transport, it is informative to first define the rate of mass transport, $m_\mathrm{T}c$ (mol m^{-2} s^{-1}), where m_T is given by[1];

$$m_T = \frac{D}{\delta} \tag{1.20}$$

and δ is the diffusion layer thickness, which describes the thickness of the region of depletion near the electrode through which electroactive material must diffuse to reach the electrode. The diffusion layer is depleted as a result of a charge transfer reaction and as such, the diffusion layer thickness is a function of the time, t, of electrolysis and can be estimated as the root-mean-squared displacement[2], such that;

$$\delta \approx \sqrt{\left\langle (x(t) - x_0)^2 \right\rangle} = \sqrt{2Dt} \tag{1.21}$$

As time progresses, the diffusion layer becomes thicker and thus the electroactive species must diffuse over a longer distance; hence the rate of mass transport to the electrode decreases at longer times. This is an important statement, as we later find that the relative reversibility of a couple is often dependant on the timescale of the experiment.

The term 'electrochemically reversible' refers to a situation where the rate constant, k°, is sufficiently high that the charge transfer interface is always at equilibrium on the timescale of the experiment[2]. An electrochemical couple of the form described by (1.15) is said to be reversible if the electron transfer rate constant, k°, is sufficiently 'fast' compared to the mass transport coefficient, m_{T}, i.e. $k^\circ >> m_T$. In such situations, the Butler-Volmer equation can be effectively normalised by dividing by the so-called 'exchange current' (the current in the absence of an overpotential), to yield the Nernst equation[2]

$$E = E_f^\circ + \frac{RT}{F}\ln\left(\frac{[\mathrm{A}]}{[\mathrm{B}]}\right) \tag{1.22}$$

which can be used to predict electrolyte composition as a function of potential.

Conversely, an electron transfer reaction is said to be electrochemically 'irreversible' if the rate of mass transport is sufficiently faster than the rate of electron transfer, i.e. $m_T >> k^\circ$. In the case of irreversible electrode kinetics, equilibrium is not reached at potentials near E_f° on the timescale of the experiment and a significant overpotential is required to 'drive' the reaction.

In practise, however, most electrochemical couples are found to exhibit kinetics intermediate to these two limiting cases and these systems are said to be 'quasi-reversible.

1.4.3 The Tafel Law

As shown in Section 1.4.1, the Butler-Volmer equation (1.19) describes the current response as a function of applied potential. Given that the exponents for both the anodic and cathodic components of (1.19) contain the term $E - E_f^\circ$ it is apparent that, given a sufficient overpotential in either direction, either the anodic or the cathodic term will tend towards zero. For the case of a reduction, when the anodic term tends to zero, (and assuming that the concentrations of A and B are approximately equal to their bulk values) the Butler-Volmer equation (1.19) can be rearranged such that;

$$i = i_0 \exp\left(-\frac{\alpha F}{RT}(E - E_f^\circ)\right) \tag{1.23}$$

where i_0 is the so-called 'exchange current' (the current in the absence of an overpotential). Equation (1.23) can then be rearranged to yield;

$$E - E_f^\circ = -\frac{RT}{\alpha F}\ln(i) + \frac{RT}{\alpha F}\ln(i_0) \tag{1.24}$$

where the second term on the right hand side is necessarily a constant. Thus, it is possible to construct a plot of E *vs.* $\ln\ i$, from which one can easily calculate the cathodic transfer coefficient α . These arguments can also be applied to the anodic case in an analogous manner. There are, however, limits on the extent to which such Tafel analysis can be applied. Firstly, the requirement that the surface concentrations are not substantially changed from their bulk values implies that the diffusion layer must be sufficiently small, such that the rate of the electron transfer reaction is not mass transport limited, and the reaction is under kinetic control. Secondly, the requirement of a large overpotential (while not reaching a steady-state) implies that this method is only suitable for sufficiently irreversible electrode kinetics. The combination of these two limitations implies that even for a sufficiently irreversible couple, the potential range over which Tafel analysis is applicable is limited. However, it is possible to overcome these limitations to some extent by using a 'mass transport corrected Tafel' equation, although this analysis is limited to systems in which limiting currents can be measured[1].

1.4.4 Multi-Step Electron Transfer

So far we have dealt only with systems involving a single electron transfer, however, in practice, electrochemical mechanisms often contain multiple electron

transfer reactions (and also homogeneous steps, which are covered in the next section). In such mechanisms, the current response is accordingly dictated by the step with the slowest kinetics and this step is thus referred to as the 'rate-determining step' (RDS). For example, consider the following electrode process;

$$\mathrm{A} + n'\mathrm{e}^- \rightleftharpoons \mathrm{A}' \tag{1.25}$$

$$\mathrm{A}' + \mathrm{e}^- \underset{k_b}{\overset{k_f}{\rightleftharpoons}} \mathrm{B}' \tag{1.26}$$

$$\mathrm{B}' + n''\mathrm{e}^- \rightleftharpoons \mathrm{B} \tag{1.27}$$

where (1.25) represents the *total* result of all steps preceding the RDS (1.26) and (1.27) represents the net result of all steps following the RDS. n' thus represents the total number of electrons transferred prior to the RDS and similarly n'' the total number transferred after the RDS. For the multi-step mechanism shown above, the Butler-Volmer expression for the current-potential behaviour becomes;

$$i = nFAk^\circ_{\mathrm{RDS}}\left([\mathrm{A}']\exp\left(-\frac{\alpha F}{RT}(E - E^\circ_{\mathrm{RDS}})\right) - [\mathrm{B}']\exp\left(\frac{(1-\alpha)F}{RT}(E - E^\circ_{\mathrm{RDS}})\right)\right) \tag{1.28}$$

where k°_{RDS}, α and E°_{RDS} all apply to the RDS. The concentration terms in (1.28) are now controlled, not only by mass transport and kinetics, but also by the properties of the preceding reactions[2]. Importantly, Tafel analysis can be performed on (1.28) (in a method analogous to that for the case of a one electron transfer, described in the previous section), such that for a reduction;

$$i = i_0 \exp\left(-\frac{(n' + \alpha)F}{RT}(E - E^{\circ}_{\mathrm{RDS}})\right) \tag{1.29}$$

where n' again refers to the total number of electrons transferred before the RDS. As a result, given that the conditions outlined in the previous section hold for the RDS and Tafel analysis is possible, it is possible to determine the RDS through Tafel analysis alone.

1.5 Homogeneous Processes

As mentioned in the previous section, a homogeneous electron transfer mechanism may also involve homogeneous chemical steps, which my occur either before, after or intermediate to electron transfer steps. The notation used to describe electrochemical mechanisms must therefore differentiate between the two. The mostly commonly used notation is that proposed by Testa and Reinmuth, who suggested that heterogeneous electron transfer steps be represented by an 'E' and homogeneous steps by the letter 'C'[21]. The following are some of the most frequently encountered examples of such mechanisms.

1.5.1 EC Mechanism

The EC mechanism represents cases where the product of a heterogeneous electron transfer undergoes a follow-up chemical reaction, such that;

$$\mathrm{A} + \mathrm{e}^- \rightleftarrows \mathrm{B} \tag{1.30}$$

$$\mathrm{B} \rightarrow \mathrm{C} \tag{1.31}$$

In the EC case, the overall product of the reaction mechanism, C, is not electroactive at potentials where the precursor, A, is reduced. This mechanism is quite common, as the product of a charge transfer reaction is quite often a reactive species[2].

A special case of the EC mechanism is that of the so-called EC' mechanism, which refers to a heterogeneous electron transfer step followed by a homogeneous reaction involving the catalytic regeneration of the electroactive species. Another special case of this mechanism is termed the EC_2 mechanism and involves a homogeneous step in which the product of the heterogeneous step dimerises in a second order reaction.

1.5.2 ECE Mechanism

In the case of the ECE mechanism, shown below, the product of the chemical step *is* electroactive at potentials near those at which the first electron transfer occurs.

$$A + e^- \rightleftarrows B \tag{1.32}$$

$$B \rightarrow C \tag{1.33}$$

$$C + e^- \rightleftarrows D \tag{1.34}$$

It should be mentioned that the ECE mechanism, where the second electron transfer occurs at the electrode surface, is often very difficult to differentiate from situations in which the second electron transfer occurs in solution. Mechanisms of this form are termed DISP mechanisms.

1.5.3 DISP Mechanism

As mentioned above, the DISP mechanism is similar to the ECE case, except that the second electron transfer occurs in the homogeneous phase;

$$A + e^- \rightleftarrows B \tag{1.35}$$

$$B \rightarrow C \tag{1.36}$$

$$B + C \rightarrow A + D \tag{1.37}$$

where one of the products of the homogeneous electron transfer is the precursor species, A, which is then available to undergo reduction at the electrode surface once more. The DISP mechanism can be further classified as a DISP1 or DISP2 mechanism, depending on which homogeneous step is rate determining. If (1.36) is rate determining then the mechanism is said to be DISP1, while if (1.37) is rate determining it is classed as DISP2[1]. DISP2 mechanisms are easily differentiated from the ECE and DISP1 cases, as the forward peak potential in a linear sweep voltammogram shows a dependence on the concentration of A as well as a scan rate dependence of 20 mV/decade (compared to the 30 mV/decade of the ECE and DISP1 schemes)[1]. However it is difficult to differentiate between ECE and DISP1 mechanisms as both have the same rate determining step and scan rate dependence of the forward peak potential, which also does not vary with scan rate.

It is possible under some circumstances to differentiate between the ECE and DISP1 cases, when the formal potentials of the two electron transfers are sufficiently separated, *via* double-step chronoamperometry[22]. However, in cases

where this is not possible, a distinction between the two mechanisms may be possible by employing electrochemical simulation techniques, such as those described in Section 1.8.3.

1.6 Electrochemical Cells

The preceding sections have described the fundamental principles upon which electrochemical techniques are based. This section now focuses on some of the more practical aspects of electrochemistry.

In order to apply a potential difference across a solution (and hence for a current to flow) at least two electrodes are required. The electrode representing the interface of interest and under study is termed the 'working electrode' (WE), while the second electrode (in the case of a two-electrode system) is termed the 'reference electrode' (RE). The primary function of the reference electrode is to maintain a constant reference potential against which the potential of the working electrode can be measured. This can, however, prevent a challenge in a two-electrode system if the electrode interfaces are of comparable dimensions; as for a reference electrode to maintain a constant potential, the chemical environment at the electrode surface must also be constant (by virtue of the Nernst equation). This clearly will not be the case if the current passed is large and thus, in such cases, it is necessary to employ a third electrode, termed the 'counter electrode' (CE), which serves the function of passing the current which would otherwise need to be delivered by the reference electrode. All three of the electrodes are

then controlled by a 'potentiostat', which imposes a potential difference, E, between the working and reference electrodes. The potentiostat then records the current response as a function of the applied potential and 'drives' the potential of the counter electrode to a value which causes the same current as that at the WE to flow.

As (even with the addition of supporting electrolyte) the solution under study is not a perfect conductor, failing to employ a counter electrode in electrochemical measurements will usually result in the distortion of results. This is because such a situation would introduce an extra potential difference related to the electrical resistance of the solution, R_s, of the form iR_s (where i is the current) in addition to the potential difference between the WE and the RE.

One exception where it is acceptable to use only two electrodes is when the dimensions of the working electrode are much smaller than those of the reference electrode. In such cases only a very small current is required to flow through the reference electrode and thus the chemical environment at the surface of the RE will remain relatively unchanged and the iR_s potential difference will be negligible. Working electrodes which have such small dimensions, with radii typically on the order of several microns or less, are called 'microelectrodes' and are discussed in the following section.

1.6.1 Microelectrodes

An expression for the one-dimensional diffusion of a species to a planar macroelectrode was developed in Section 1.3.1. This expression can reasonably

approximate the diffusion limited current to the electrode when the dimensions of the electrode are large enough that the flux to the electrode is effectively constant over the entire surface (a uniformly accessible electrode). This is achieved when the radius of the electrode, r, is significantly larger than that of the diffusion layer;

$$r \gg \sqrt{2Dt} \tag{1.38}$$

If, however, the dimensions of the electrode are of the order of a few micrometers, as is the case for microelectrodes, then (1.38) will usually no longer hold true. For such situations where the electrode is not uniformly accessible, it is necessary to solve to solve Fick's second law (1.10) in cylindrical coordinates[1];

$$\frac{\partial c}{\partial t} = D\left(\frac{\partial^2 c}{\partial r^2} + \frac{1}{r}\frac{\partial c}{\partial r} + \frac{\partial^2 c}{\partial z^2}\right) \tag{1.39}$$

where r is a radial coordinate in the plane of the electrode surface and z is the perpendicular distance from the surface. Solving (1.39) analytically, in conjunction with the relevant boundary conditions, requires assumptions to made such that the flux at the edges is not infinite[23]. However, the current response to a potential step at a microdisk electrode has been shown[24] to, at sufficiently long times, yield a 'steady-state' current, i_{ss}, such that;

$$i_{ss} = 4nFcDr \tag{1.40}$$

where, c refers to the concentration of the electroactive species in the bulk solution. The full current-time transient has also been determined, by Aoki and Osteryoung[24], as a function of the dimensionless time, τ, such that;

$$i = 4nFcDr \cdot f(\tau) \tag{1.41}$$

where $\tau = 4Dt / r^2$ and $f(\tau)$ is known numerically. As mentioned above, at long times (1.41) becomes the equation for the steady-state current (1.40) as diffusion to the edge sites (convergent diffusion) dominates. At very short times though, when the thickness of the diffusion layer obeys (1.38), diffusion to the electrode surface is effectively planar and thus the current response is dictated by the Cottrell equation (1.11). The fact that a single potential step yields a current transient that is, at different times, dependant on both D and $\sqrt{D}$ is highly convenient and will be returned to in Section 1.8.1. There are also several additional benefits to using microelectrodes in electrochemical experiments.

Microelectrodes display significantly lower double layer capacitances than macroelectrodes, as the capacitance of the electrode-solution interface scales proportionally to the electrode size. As a result, the signal to noise ratio is much higher at a microelectrode and it is thus possible to employ much faster scan rates than at a macroelectrode. This in turn allows for kinetic measurements, both heterogeneous and homogeneous, which would not be possible at macroelectrodes.

As mentioned in Section 1.6, the small currents, usually of the order of nA or less, measured at microelectrodes lead to negligible iR_s distortion of the current response, even in solvents which are not excessively conducting[25]. As a result, this also allows for the use of two electrode systems employing so-called quasi-reference electrodes, which are described in the following section.

1.6.2 Reference Electrodes

The reference electrode should provide a stable and reproducible potential against which the potential applied to the working electrode can measured. In order for a system to make a good reference electrode, it must be designed in such a manner that it meets several criteria. The kinetics of the couple must be sufficiently fast that the potential is governed purely by the Nernst equation (1.3). Furthermore, the potential of the reference electrode should be stable over time and stable over as wide a temperature range as possible.

The composition of a reference electrode classifies it as one of four main kinds. Reference electrodes of the 'first kind' are based on a potential determining equilibrium between atoms or molecules and their corresponding ions in solution. Such electrodes are most often prepared simply by immersing a metal electrode in a solution of its own ion, such as $Ag|Ag^+$.

Reference electrodes of the 'second kind' consist of three phases and are usually prepared by coating a metal with a layer of a sparingly soluble salt and immersing in a saturated solution of the salt. An example of such an electrode is the $Ag|AgCl_{(s)}|Cl^-$ reference electrode.

Electrodes of the 'third kind', which are also referred to as 'redox electrodes', consist of an electrically conducting electrode immersed in a solution containing both species of a redox couple.

It is also common, especially in systems where contamination from the reference electrode to the sample solution is highly undesirable, to employ a so-called 'quasi-reference' electrode[2]. This simply involves immersing a metal wire, usually platinum or silver, into the sample solution. The use of such an electrode is usually accompanied by an 'internal reference' couple in the sample solution, such as the ferrocene|ferrocenium couple, the formal potential of which is known.

1.6.3 Counter Electrodes

The counter electrode must simply pass a current equal in magnitude to that of the working electrode. As such, the counter electrode should be constructed from an inert material and have an accessible surface area which is much larger than that of the working electrode.

1.7 Electrochemical Techniques

There exist a multitude of electrochemical techniques available to the electrochemist. The techniques employed in this thesis are 'potential step chronoamperometry', 'cyclic voltammetry' and various simulation techniques, which are outlined below.

1.7.1 Potential Step Chronoamperometry

Potential step chronoamperometry is arguably one of the simplest electrochemical techniques, yet can still provide a wealth of information. In such an experiment, the potential is initially held at a value, E_1, at which no Faradaic processes occur. The potential is then stepped to a value, E_2, at which the process of interest proceeds at a diffusion limited rate, in a manner dictated by the Cottrell equation (1.11) for macroelectrodes and a combination of (1.11) and (1.40) for microelectrodes. For macroelectrodes, where planar diffusion governs the current response, (1.11) implies that (provided three parameters are known) one can obtain either A, D, c or n from the gradient of a plot of i *vs.* $1/\sqrt{t}$.

For a microelectrode, where convergent diffusion dominates the current response, the current can be defined over the full timescale of the experiment with an error of less than 0.6% by the so-call 'Shoup-Szabo approximation'[26];

$$i = 4nFcDr \cdot f(\tau) \tag{1.42}$$

$$f(\tau) = 0.7854 + 0.8863\tau^{-\frac{1}{2}} + 0.2146\exp\ -0.7823\tau^{-\frac{1}{2}} \tag{1.43}$$

where $\tau = 4Dt / r^2$ and the expression was determined empirically. As mentioned in Section 1.6.1, the fact that at small values of τ the current response is proportional to $\sqrt{D}$, while at large values it scales with D is highly beneficial. This is because the fitting of experimental current transients with the Shoup-Szabo approximation allows for the *simultaneous* determination of D and the product nc.

1.7.2 Cyclic Voltammetry

Cyclic voltammetry is a potentiodynamic technique which involves applying a triangular potential waveform, which varies with time, across the working electrode. In such an experiment, the potential is 'scanned' from an initial value, E_1, at a set 'scan rate', υ, to a switching potential, E_2, at which point the scan direction is reversed and the sweep is generally continued until $E = E_1$ again. The result of this experiment is a plot of i *vs.* E and is called a 'cyclic voltammogram' (CV). Cyclic voltammetry is a very versatile technique which is able to provide both kinetic and thermodynamic parameters and is often the first electrochemical experiment performed as it often gives immediate information as to the formal potentials of the species under study.

In order to understand the current response to such a potential regime, we first consider the current response obtained from reducing species A by one electron, at a macrodisk electrode, to form species B. As the potential is scanned from E_1 to E_2, initially no current flows; then, as the potential approaches the formal potential, the electroactive species starts to undergo electrolysis as the heterogeneous rate constant becomes sufficiently large to allow for the depletion of the species within the diffusion layer. The current increases in an exponential manner, as indicated by the Butler-Volmer equation (1.19), until a peak is formed, at which point the concentration of A has become sufficiently depleted within the diffusion layer. At this point the current becomes mass transport limited and starts to decay with the concentration gradient, as the diffusion layer

is now thicker and thus A must diffuse a larger distance. Upon reversal of the scan direction at E_2, there is a sufficient build up of the product, B, in the diffusion layer, such that the same processes as described for the reduction also lead to an oxidation peak on the reverse sweep. As the scan rate, υ, is increased, the duration of the cyclic voltammetric experiment is decreased and as a result, the relative rate of mass transport to the electrode is increased. This then leads to larger peak currents at increased scan rates, which can be predicted by the Randles-Ševčík equation[27, 28] such that, at 298 K, the peak current, i_P, is given by;

$$i_P = (2.69 \times 10^5) A D^{\frac{1}{2}} \upsilon^{\frac{1}{2}} c \tag{1.44}$$

for the reversible limit and;

$$i_P = (2.99 \times 10^5) \alpha^{\frac{1}{2}} A D^{\frac{1}{2}} \upsilon^{\frac{1}{2}} c \tag{1.45}$$

for the irreversible limit; where α is the transfer coefficient, A is the electrode area, D is the diffusion coefficient, υ is the scan rate and c is the concentration of the electroactive species in bulk solution. Equations (1.44) and (1.45) show that, for a diffusional system, the peak currents will be linearly proportional to the square root of the scan rate. Importantly, for an adsorbed electroactive species the peak current is not dependent on the square root of scan rate, but rather is directly proportional to υ, such that[2];

$$i_P = \frac{F^2 \upsilon A \Gamma}{4RT} \tag{1.46}$$

where Γ represents the surface coverage (in mol/m^2) of the adsorbate.

As mentioned in Section 1.4.2, the electron transfer kinetics of a redox couple can be classed as reversible, quasi-reversible and irreversible. In the reversible case, the CV waveform is described as 'Nernstian', as the heterogeneous electron transfer rate constant is large enough (relative to the rate of mass transport) to ensure an equilibrium between the reduced and oxidised species at the electrode surface, defined by the Nernst equation (1.3). In the reversible limit, for the process $\mathrm{A} + n\mathrm{e}^- \rightleftharpoons \mathrm{B}$, the peak position, E_P, of both the cathodic and anodic peaks can be related to the formal potential, E_f°, such that;

$$E_P \pm E_f^\circ = 1.109\frac{RT}{nF} = \frac{28.5}{n}\ \text{mV (at 298 K)} \tag{1.47}$$

Note that (1.47) implies that, for a fully reversible system, the formal potential lies midway between the anodic and cathodic peaks, the peak potentials are independent of scan rate and the peak-to-peak potential separation, ΔE_PP is equal to $57/n$ mV at 298 K.

In the irreversible limit, when the rate of electron transfer is much slower than the rate of mass transport, much broader waveforms are encountered and the peak positions (for a one electron system) can be expressed as[2];

$$E_P \pm E_f^\circ = \frac{RT}{\alpha F}\left(0.78 + \ln\left(\frac{D^{\frac{1}{2}}}{k^\circ}\right) + \ln\left(\frac{\alpha F\upsilon}{RT}\right)^{\frac{1}{2}}\right) \tag{1.48}$$

where $\Delta E_{PP} = 47.7 / \alpha$ mV at 298 K. Importantly, (1.48) also shows that, for an irreversible system, the peak positions occur further from the formal potential by an activation overpotential related to k° and are also dependent on the scan rate.

For a quasi-reversible system, the kinetics are intermediate to the two limiting cases and it becomes more complicated to define the current-potential characteristics. However, this case has been treated by Matsuda and Ayabe[29], who showed that the various peak parameters were functions of α and the parameter Λ, which is defined as;

$$\Lambda = \frac{k^\circ}{\sqrt{D_A^{1-\alpha} D_B^{\alpha} \frac{F\upsilon}{RT}}} \tag{1.49}$$

where D_A and D_B are the diffusion coefficients of species A and B, respectively. Matsuda and Ayabe then further suggested that the various kinetic cases could be defined such that;

$$\begin{array}{ll} \text{Reversible:} & \Lambda > 15,\ k^\circ > 0.3\sqrt{\upsilon} \\ \text{Quasi-Reversible:} & 15 \geq \Lambda \geq 10^{-2(1+\alpha)},\ 0.3\sqrt{\upsilon} \geq k^\circ \geq (2\times10^{-5})\sqrt{\upsilon} \\ \text{Irreversible:} & \Lambda < 10^{-2(1+\alpha)},\ k^\circ < (2\times10^{-5})\sqrt{\upsilon} \end{array} \tag{1.50}$$

The definitions of the limits in (1.50) show that, as mentioned in Section 1.4.2, a system may show behaviour which switches between the different cases depending on the timescale (scan rate) of the experiment.

As microelectrodes are also used extensively throughout this thesis, it is of interest to compare their voltammetric response with that of macroelectrodes. As

mentioned in Section 1.6.1, at short timescales (fast scan rates), when the diffusion layer is very thin, diffusion to a microelectrode is predominantly planar. This results in peak shaped voltammetry similar to that at macroelectrodes. If, however, the scan rate is sufficiently slow, convergent diffusion will dominate and the current response will be of a steady-state nature. This type of behaviour occurs because the rate of mass transfer to the electrode is sufficiently fast that the concentrations of electroactive species at the electrode surface is constantly replenished over the entire potential range and as such the concentration profile at a given potential is independent of time.

Steady-state voltammetry is typically characterised by both the limiting current, i_{SS}, and the so-called 'half-wave potential', $E_{1/2}$, which is the potential at which the current is exactly half of i_{SS}. This half-wave potential approaches the formal potential when the kinetics are sufficiently fast, though deviates significantly as the kinetics approach the irreversible limit. If the kinetics of the electron transfer are quasi-reversible, it is also possible to extract k°, E_f° and α from a steady-state voltammogram[30] *via* the parameters ($E_{1/4}$ – $E_{1/2}$) and ($E_{1/2}$ – $E_{3/4}$). Finally, the appearance of either steady-state or transient behaviour in a microelectrode voltammogram can be predicted by the parameter p, such that[1];

$$p = \sqrt{\frac{Fr^2\upsilon}{RTD}} \tag{1.51}$$

where if $p \ll 1$, the voltammetry will be steady-state in nature, while if $p \gg 1$, transient behaviour will be observed.

1.7.3 Modelling Electrochemical Processes

Although voltammetric measurements can provide a wealth of information on both heterogeneous and homogeneous processes directly, mechanistically complex systems are often difficult to characterise directly. In such cases it is common to employ numerical data simulation methods, of which there are several types.

Probably the most common of these is the 'implicit finite difference' method, which is based on the combination of an exponentially expanding space model with an implicit simulation algorithm[31]. These methods are based on solving the partial differential equations associated with mass transport after imposing a space-time grid on the system. As such, positions and times are discretised, with a choice of dimensions appropriate to the electrode geometry, and the concentrations at each point calculated for each timestep. The model also accounts for both heterogeneous and homogeneous kinetics and after solving all of the relevant equations, outputs a current value as a function of time/potential. The computation time for complex mechanisms with kinetic steps increases proportionally to $m^3(n + 1)$, where m is the number of species involved and n represents the number of grid boxes required, i.e. the resolution[31].

This concludes the brief introduction to the fundamental principles and techniques of electrochemistry which are used throughout this thesis. The next chapter gives an introduction on the nature of the room-temperature ionic liquids used in this work and discusses some practical aspects of working with them.

References

1. R. G. Compton and C. E. Banks, *Understanding voltammetry*, World Scientific, Singapore; London, 2nd edn., 2011.
2. A. J. Bard and L. R. Faulkner, *Electrochemical Methods: Fundamentals and Applications*, Wiley, New York, 2nd edn., 2000.
3. J. O. M. Bockris and A. K. N. Reddy, *Modern electrochemistry*, Plenum Press, New York, 1998.
4. R. G. Compton and G. H. W. Sanders, *Electrode Potentials*, Oxford University Press, Oxford, 1996.
5. A. C. Fisher, *Electrode Dynamics*, Oxford University Press, Oxford, 1996.
6. C. M. A. Brett and A. M. O. Brett, *Electrochemistry: Principles, Methods, and Applications*, Oxford University Press, Oxford, 1993.
7. F. Scholz, *Electroanalytical Methods: Guide to Experiments and Applications*, Springer, 2nd edn., 2010.
8. L. E. Barrosse-Antle, A. M. Bond, R. G. Compton, A. M. O'Mahony, E. I. Rogers and D. S. Silvester, *Chemistry – An Asian Journal*, 2010, 5, 202-230.
9. R. A. Serway and J. W. Jewett, *Physics for Scientists and Engineers*, Brooks/Cole, California, 9th edn., 2013.
10. H. L. F. von Helmholtz, *Ann. Physik*, 1853, 165, 211-233.
11. H. L. F. Von Helmholtz, *Ann. Physik*, 1879, 243, 337-382.
12. G. Gouy, *J. physique*, 1910, 9, 457-467.
13. G. Gouy, *Compt. rend.*, 1910, 149, 654-657.
14. D. L. Chapman, *Phil. Mag.*, 1913, 25, 475.
15. O. Stern, *Z. Elektrochem. Angew. Phys. Chem.*, 1924, 30, 508-516.
16. D. C. Grahame, *Chem. Rev. (Washington, DC, U. S.)*, 1947, 41, 441-501.
17. J. O. M. Bockris, M. A. V. Devanathan and K. Mueller, *Proc. Phys. Soc. (London) Ser. A*, 1963, 274, 55-79.
18. F. G. Cottrell, *Z. Phys. Chem., Stoechiom. Verwandtschaftsl.*, 1903, 42, 385-431.
19. J. A. V. Butler, *Trans. Faraday Soc.*, 1924, 19, 729-733.
20. T. Erdey-Gruz and M. Volmer, *Z. physik. Chem.*, 1930, 150, 203-213.

21. A. C. Testa and W. H. Reinmuth, *Anal. Chem.*, 1961, 33, 1320-1324.
22. C. Amatore and J. M. Savéant, *Journal of Electroanalytical Chemistry and Interfacial Electrochemistry*, 1980, 107, 353-364.
23. K. Aoki, *Electroanalysis*, 1993, 5, 627-639.
24. K. Aoki and J. Osteryoung, *Journal of Electroanalytical Chemistry*, 1981, 122, 19-35.
25. J. Heinze, *Angewandte Chemie International Edition in English*, 1991, 30, 170-171.
26. D. Shoup and A. Szabo, *Journal of Electroanalytical Chemistry and Interfacial Electrochemistry*, 1982, 140, 237-245.
27. J. E. B. Randles, *Trans. Faraday Soc.*, 1948, 44, 327-338.
28. A. Ševčík, *Collect. Czech. Chem. Commun.*, 1948, 13, 349-377.
29. H. Matsuda and Y. Ayabe, *Z. Elektrochem. Angew. Phys. Chem.*, 1955, 59, 494-503.
30. M. V. Mirkin and A. J. Bard, *Anal. Chem.*, 1992, 64, 2293-2302.
31. M. Rudolph, *J. Electroanal. Chem. Interfacial Electrochem.*, 1991, 314, 13-22.

2. Introduction to Room Temperature Ionic Liquids

Room temperature ionic liquids (RTILs) are a class of molten salts, composed entirely of ions, which are liquid at and around room temperature. These ionic liquids are used extensively throughout the work reported in this thesis and, as such, a brief introduction to RTILs and their properties is pertinent.

2.1 Introduction

The attraction of using RTILs as solvents, especially for electrochemical experiments, is due to several advantageous properties. Room temperature ionic liquids have wide electrochemical windows, low volatility, high thermal stability, and possess a high *intrinsic* conductivity[1-6]. Importantly, RTILs have also been shown, in certain cases, to stabilise intermediates and products which would not be stable in conventional molecular solvents[7] as well as strongly influence the reactivity of radical ions[8-10]. Ionic liquids are also relatively environmentally friendly compared to conventional volatile organic solvents and thus there has been considerable research performed using RTILs in the field of 'green chemistry'[11-14].

The history of ionic liquids has been covered extensively in several books and review articles, the most notable of which is that by Wilkes[4] who gives a firsthand account as one of the 'three grandfathers of ionic liquids' (the others being Osteryoung and Hussey). However, it is informative to give a brief history here, as

doing so provides a method of grouping RTILs into categories based on their 'generation'.

The first generation of ionic liquids are those based on haloaluminate anions such as $[AlCl_4]^-$ and $[Al_2Cl_4]^-$, the first of which was a 1-butylpyridinium chloride-aluminium chloride mixture[15]. These ionic liquids, however, have a major drawback in that they are highly sensitive to moisture and must thus be handled under anhydrous conditions[16].

The second generation of ionic liquids are based on such anions as tetrafluoroborate ($[BF_4]^-$), hexafluorophosphate ($[PF_6]^-$), nitrate ($[NO_3]^-$), Sulphate ($[SO_4]^-$) and acetate ($[CH_3COO]^-$) and were first prepared *via* the metathesis reactions of a dialkylimidazolium halide with an appropriate silver salt[17]. However, while these second generation ionic liquids are *less* reactive to water, they are still quite hygroscopic and as a result have very different physical and chemical properties depending on the moisture content. The $[BF_4]^-$ and $[PF_6]^-$ anions have also been shown to hydrolyse to form hydrogen fluoride[1].

More recent ionic liquids, which lie between the second and third generation, are based on anions such as bis(trifluoromethylsulfonyl)imide ($[NTf_2]^-$) and perfluoroalkylphosphate ($[FAP]^-$), which are significantly more hydrophobic. The third generation of RTILs then comprises the so-called 'task specific' ionic liquids, in which functional groups are incorporated into the cation or anion[18-20]. There also exist ionic liquids based on anions which are difficult to categorise into any of the above generations, such as dicyanamide ($[N(CN)_2]^-$) and thiocyanate

($[SCN]^-$). Some of these are halide-free or possess physical properties such as lower viscosity and increased conductivity[3].

The most commonly encountered cations are based on alkylmethylimidazolium ($[C_nmim]^+$), alkylmethylpyrrolidinium ($[C_nmPyrr]^+$), tetraalkylammonium ($[N_{a,b,c,d}]^+$) and tetraalkylphosphonium ($[P_{a,b,c,d}]^+$) moieties. The structures of the ionic liquids used in this thesis are presented in Chapter 3. However, broadly, they consist of a bulky, asymmetric, organic cation and a weekly coordinating inorganic anion.

2.2 Synthesis of RTILs

Most of the commonly encountered ionic liquids described in the previous section are usually synthesised in a two step procedure. The first step of this procedure involves the alkylation of the parent precursor (i.e. methylpyrrolidine for alkylmethylpyrrolidinium RTILs) using an alkyl halide[21]. After the desired cation halide has been formed the anion is introduced as either an alkali metal or silver salt, thus forming the desired RTIL in a metathesis reaction, with the silver halide or alkali metal halide as a byproduct. This two step procedure has been used for the synthesis of imidazolium, pyrrolidinium, tetraalkylammonium and tetraalkylphosphonium ionic liquids, with various anions[21-24]. In all cases that a procedure of this sort is implemented, it is necessary to purify the resultant ionic liquids, as impurities can have significant effects on the physical properties of the RTILs, as will be discussed in Section 2.4.

2.3 Properties of RTILs

In order to determine if room temperature ionic liquids are suitable as solvents for electrochemical applications, it is first desirable to have an understanding of their physical and chemical properties, which are described below.

2.3.1 Viscosity

The viscosity of a solvent can have important implications for electrochemical experiments as high viscosities lead to decreased mass transport in solution[6, 25]. Room temperature ionic liquids tend to exhibit viscosities comparable to those of oils, generally around 30 to 450 cP or approximately 10 to 100 times higher than conventional molecular solvents[6, 26]. The viscosity of an ionic liquid depends on both the cation and anion and the differences in viscosity between RTILs is predominantly related to differences in hydrogen bonding and Van der Waals interactions[25, 27-30]. The addition of small amounts of organic cosolvents[31] or water[32] typically leads to a lower viscosity, but also causes the RTIL to lose some of its more favourable properties, such as low volatility and high thermal stability (covered below), as well as introducing extra possible reactants to the system. The viscosities of ionic liquids are also highly temperature dependent, with a 20 percent change over 5 K around room temperature not uncommon[33]. The viscosities of most ionic liquids, especially those consisting of asymmetrical cations without added functional groups, tend to exhibit an Arrhenius relationship to the temperature[34], such that;

$$\ln \eta = \ln \eta_{\infty} + \frac{E_{\eta}}{RT} \tag{2.1}$$

where the viscosity, η, is dependent on the hypothetical viscosity at infinite temperature, η_{∞} and the temperature, T, and E_{η} is the activation energy for viscous flow and R is the universal gas constant.

2.3.2 Density

Room temperature ionic liquids are typically denser than water and most organic solvents, with densities of the order of 1 to 1.6 g cm^{-3} being common[35]. Ionic liquids with longer alkyl chains or larger cations are generally less dense than those with shorter alkyl chains or less bulky cations[1]. Furthermore, the density of an RTIL will tend to decrease in the approximate order; $[FAP]^- > [NTf_2]^- > [PF_6]^- > [BF_4]^-$. In contrast to viscosity, the densities of ionic liquids do not tend to vary considerably with temperature[1].

2.3.3 Conductivity

Ionic liquids, by definition, exhibit an intrinsic ionic conductivity as the ions act as charge carriers. In an electrochemical experiment, the conductivity of the solution is of vital importance (as discussed in Chapter 1), which is partly why supporting electrolytes are added to conventional molecular solvents in such experiments. Generally, most RTILs exhibit conductivities which are comparable to those of organic solvents containing added supporting electrolyte, but less than that of aqueous electrolytic solutions[5]. The reason that ionic liquid conductivities are generally lower than for water with added electrolyte, even though the RTIL

is composed entirely of ions, is because the conductivity, κ, is a function of both the concentration of charge carriers and their mobility in solution[36], such that;

$$\kappa = F\sum_{i}\left|z_i\right|u_i c_i \tag{2.2}$$

where F is the Faraday constant and z_i, u_i and c_i the charge, mobility and concentration, respectively, of species, i. The mobility is an index of the migration velocity of an ion and is defined as the limiting velocity of the ion in an electric field of unit strength. Thus, while ionic liquids contain a large number of charge carriers, the high viscosity of RTILs and large size of the constituent ions result in low mobilities and thus only average conductivities. The conductivity of an ionic liquid is often approximately inversely proportional to its viscosity and the conductivity increases with increasing temperature due to the increased mobilities as the viscosity decreases[5, 37]. The variation of conductivity with temperature in RTILs is described by the Vogel-Tammann-Fulcher relationship[38-40];

$$\kappa = A\sqrt{T}\exp\left[-B(T - T_0)\right] \tag{2.3}$$

where T_0 is the ideal gas temperature at which the conductivity drops to zero and the constants A and B are derived empirically for each ionic liquid[33, 37].

2.3.4 Electrochemical Window

The electrochemical window of a solvent is defined as the difference between the anodic and cathodic breakdown potentials of the solvent and/or supporting electrolyte (whichever occurs first). Aqueous solutions exhibit narrow potential

windows (*ca.* 1.5 to 2 V) at most electrodes, due to the oxidation and reduction of water[36]. The electrochemical windows of non-aqueous solvents on the other hand are considerably larger (*ca.* 3 to 5 V)[36]. Ionic liquids, however, typically possess electrochemical windows which are even larger than those of molecular aprotic solvents (*ca.* 4 to 6 V)[41] due to the electrochemical stability of their constituent ions. The electrochemical window is thus clearly dependent on the ions from which the RTIL is composed. The cation has been suggested to play a more significant role in determining the electrochemical window[5]. In terms of the cation, it is generally the case that the electrochemical window increases in the order[42] $[C_n mim]^+ < [N_{a,b,c,d}]^+ < [C_n mPyrr]^+ < [P_{a,b,c,d}]^+$. The nature of the anion also has an impact, albeit a smaller one, on the width of the potential window and the electrochemical window is found to generally increase in the order[5] $[X] < [BF_4]^- \approx [PF_6]^- < [NTf_2]^- < [FAP]^-$, where X is a halide. While the potential window of ionic liquids may vary as a function of ionic composition, RTILs in general still exhibit larger potential windows than molecular solvents, which may then allow for the study of species which are electroactive but would normally lie outside of the accessible potential range.

2.3.5 Melting Points, Thermal Stability and Volatility

Room temperature ionic "liquids" are broadly defined as salts which have a melting point below 100°C[1] (a temperature chosen somewhat arbitrarily). In order to use these salts as electrochemical solvents, they must remain in the liquid state over the entire temperature range under study. Typical inorganic salts have

melting points on the order of 1000°C, which reflect their high lattice energies and are a result of a high degree of coordination and strong electrostatic forces between the ions[43]. As the ions comprising an RTIL are both bulky and organic, van der Waals, hydrogen bonding and π-π stacking interactions also contribute, alongside electrostatic forces, to the lattice energies. The melting points of ionic liquids tend to decrease as the size of the anion or cation, the delocalisation of charge and also as the degree of asymmetry in the ions increases[1]. The melting points decrease as the radii of one or more of the ions increase because the surface charge density decreases and the ionic separations increase. In effect, all of the points described above indicate that as the ions pack less efficiently, the melting point decreases, defining the lower limit of the liquidus range.

The upper limit of the liquidus range for a conventional molecular solvent is generally defined by its boiling point. However, in the case of ionic liquids it is more frequently defined by the decomposition temperature, as this is usually lower than the boiling point due to RTILs exhibiting negligible vapour pressure.

The majority of ionic liquids are reported to have onset decomposition temperatures in the range of *ca.* 573 to 673 K, with some remaining thermally stable at temperatures up to 773 K[44]. The mechanisms of thermal degradation are very much dependent on the specific ionic liquid and even then are not straightforward as multiple parameters must be taken into account, as demonstrated in a review by Maton[44].

As mentioned above, room temperature ionic liquids usually exhibit negligible vapour pressures, under atmospheric pressure, at temperatures up to their thermal decomposition as a result of the strong coulombic interactions between the ions[1]. However, Rebello *et. al.* used experimental surface tension and density data to predict that it should be possible to distil $[C_n mim][NTf_2]$ ionic liquids, when n was large, at temperatures between their estimated boiling and decomposition temperatures[45]. Subsequently, they showed that it was possible to distil $[C_{10}mim][NTf_2]$ and $[C_{12}mim][NTf_2]$ at 450 K under a reduced pressure of 0.01 mbar[45]. It was later shown that several additional room temperature ionic liquids were also distillable, at temperatures between 473 and 573 K and pressures of 0.001 to 0.1 mbar[46]. However, as many ionic liquids show little or no evidence of distillation below their thermal decomposition temperatures[1], for most practical electrochemical purposes RTILs can be treated as having negligible volatility.

2.4 The Effects of Impurities

Despite many ionic liquids being labelled as 'hydrophobic', it is well established in the literature that all ionic liquids absorb water to some extent, which then leads to a decrease in the potential window as well as altered mass transport due to viscosity changes[25, 27, 35]. However, several other common impurities have also been shown to influence the physical properties of RTILs, the most notable of which are dissolved gasses, halides and other unreacted starting materials

remaining after their synthesis. All of these common contaminants and their effects on the electrochemical and physical properties of RTILs will be briefly covered below.

2.4.1 Water

Dissolved water is highly undesirable when conducting electrochemical studies in room temperature ionic liquids, as the amount of the impurity is often unknown and dissolved water (depending on the concentration) can drastically alter the properties of the RTIL. Water impurities in ionic liquids have been shown to significantly reduce the electrochemical window[47], decrease the density[48], increase the conductivity[49] and decrease the viscosity[50], thereby altering rates of mass transport in the RTIL. As a result of the numerous detrimental effects which dissolved water can impose on an RTIL electrochemical experiment, and taking into account the negligible vapour of RTILs, vacuum techniques have been strongly advocated for the removal of water[25].

2.4.2 Halides and Other Unreacted Starting Materials

Halide impurities can be present in an ionic liquid due to an incomplete metathesis reaction in their synthesis (see Section 2.2). The effects of halide impurities have been reviewed by Seddon *et al.* for imidazolium ionic liquids, who reported a notable increase in viscosity with increasing chloride concentration[51]. Halide impurities can also reduce the electrochemical window of an RTIL, as halides are generally oxidised at more negative potentials than most RTIL anions[52] (see Section 2.3.4). Furthermore, halide impurities may act as stabilising

ligands, nucleophiles or reactants, depending on the nature of the reaction[53], and thus react with electrochemically formed intermediates[54], potentially altering both kinetic and thermodynamic parameters. Similarly, other unreacted starting materials, such as imidazole in the case of imidazolium ionic liquids or pyrrolidine in pyrrolidinium based RTILs, may also alter these parameters.

2.4.3 Dissolved Gases

Several dissolved gases can also present complications when undertaking electrochemical experiments in room temperature ionic liquids. Initially, it was thought that only electroactive gasses such as oxygen would interfere in ionic liquid based experiments, however, it has since been shown that several other dissolved gasses may interfere by altering mass transport.

The presence of dissolved oxygen, from the atmosphere or otherwise, presents a considerable obstacle for electrochemical studies as it is relatively easy to reduce at most electrodes and may therefore contribute to the background current or even swamp the current of interest entirely[5]. Depending on the specific RTIL, reduction currents corresponding to the reduction of oxygen to superoxide and the reduction of superoxide to peroxide may be observed[55].

Furthermore, several gases which were previously thought to be electrochemically benign, such as argon, nitrogen and carbon dioxide, have since been shown to alter the mass transport properties of ionic liquids, either by only partially removing dissolved water, or by dissolving to such a large extent that the viscosity of the RTIL is altered[56-58].

2.5 Fundamental Electrochemistry in RTILs

The previous section described some of the more fundamental properties of ionic liquids. This section now devotes greater detail to the behaviour of RTILs as electrochemical solvents and briefly compares their electrochemical behaviour to that observed in conventional molecular solvents.

2.5.1 Mass Transport

As mentioned in Section 2.3, ionic liquids can be two to three orders of magnitude more viscous than conventional molecular solvents. As such, the diffusion coefficients of electroactive species are often roughly two to three orders of magnitude lower in RTILs than in conventional aprotic solvents. This can be rationalised as diffusion coefficients are generally found to be inversely proportional to viscosity, as dictated by the Stokes-Einstein equation;

$$D = \frac{k_B T}{p\pi r_h \eta} \tag{2.4}$$

where k_B is the Boltzmann constant, T is the temperature, p is a constant, r_h is the hydrodynamic radius of the diffusing species and η is the solvent viscosity. The fact that the diffusion coefficients of larger molecules, such as ferrocene[59], cobaltocene[59] and N,N,N'N'-tetramethylphenylenediamine[60] in RTILs follow the Stokes-Einstein equation gives an indication that ionic liquids behave like conventional solvents[6]. However, for smaller molecules such as O_2[55] and H_2[61], the equation was found to break down. In general, the likelihood of a given system to adhere to (2.4), increases if the solute and solvent are of comparable size[5]. As the

viscosity of an ionic liquid is highly sensitive to temperature (see Section 2.3.1), so too is the diffusion coefficient and as such, the diffusion coefficient often follows an Arrhenius type relationship to temperature;

$$D = D_{\infty} \exp\left(\frac{-E_{a,D}}{RT}\right) \tag{2.5}$$

where D_{∞} represents the hypothetical diffusion coefficient at infinite temperature and $E_{a,D}$ is the activation energy of diffusion,

The slow diffusion coefficients often encountered when employing ionic liquids in electrochemical studies have some important practical implications. The steady-state limiting current at a microdisk electrode is often used to determine diffusion coefficients or to determine electrode radii (see Chapter 1). However, if a true steady-state is not reached, these measurements may not be accurate. In order to reach a true steady state in a voltammetric experiment, it is required that;

$$\upsilon \ll \frac{RTD}{nFr^2} \tag{2.6}$$

where υ is the scan rate, R the universal gas constant, T the temperature, D the diffusion coefficient, n the number of electrons transferred, F is the Faraday constant and r is the radius of the electrode. This approximation shows that in ionic liquid media, where diffusion coefficients are often of the order of 1×10^{-11} m^2 s^{-1}, in order to obtain true steady-state behaviour scan rates of 10 mV s^{-1} or

below, in conjunction with electrode radii of 5 μm, are required. Interestingly, this relation also shows that for $D = 1\times10^{-11}$ m^2 s^{-1} and $r = 5$ μm, both steady-state and transient behaviour can be observed in a single system by varying the scan rate. Additionally, (2.6) shows that for an electrode with $r = 5$ μm and a scan rate of 10 mV s^{-1}, differing diffusion coefficients will lead to either steady-state or transient behaviour. It is important that this is highlighted, as in ionic liquid media the ionic nature of the solvent can lead to differences in the diffusion coefficients of neutral and charged species of over an order of magnitude. For example, the diffusion coefficients of oxygen (O_2) and superoxide ($O_2^{\bullet-}$) in the $[N_{6,2,2,2}][NTf_2]$ ionic liquid were found to be 1.5×10^{-10} and 4.7×10^{-12} m^2 s^{-1}, respectively[62]. Such large differences in the diffusion coefficients of a redox couple thus manifests as a single voltammogram displaying both steady-state and transient behaviour. As a result of this behaviour, microelectrodes are frequently employed in electrochemical studies in ionic liquids, where all of the benefits outlined in Chapter 1 also hold true.

2.5.2 Electron Transfer Kinetics

The transfer of kinetics from conventional solvents to ionic liquids is not as straightforward as for mass transport. There is of course evidence of kinetic studies in ionic liquids reported in the literature[63-69], however, to a much lesser extent than for molecular aprotic solvents.

It has been claimed, *via* simulation techniques, that solvent reorganization energies associated with an electron transfer are similar in RTILs and acetonitrile,

and the charge-transfer process is Marcus-like[69]. However, the mechanisms by which an ionic liquid responds to an applied electric field are quite different from a conventional aprotic solvent. In conventional solvents the solvent molecules re-orientate, whereas in an RTIL the molecules must move relative to each other. These differences must impact upon the overall observed rate of electron transfer and thus inner-sphere electron transfer rates might be expected to be similar in RTILs compared to aprotic solvents, while outer-sphere electron transfers will be very different due to the electrostatic screening mechanisms[70].

There has also been experimental confirmation of these suggestions, as Lagrost *et al.* have studied the heterogeneous electron transfer kinetics of several aliphatic and aromatic nitro compounds[71] and several electrogenerated radical cations[72]. For the nitro compounds, they found that k° values decreased by two orders of magnitude when the inner sphere contribution to the activation energy of the electron transfer was low, when moving from acetonitrile to the ionic liquid. However, when the inner sphere contributions were more important, such as for the reduction of 2-methyl-2-nitropropane, they found little variation in the k° values. The study of the electrogenerated radical cations, in which the cation radicals undergo first and second-order chemical reactions, showed that switching from acetonitrile to the ionic liquid did not affect the *nature* of the mechanisms. However, k° values were found to be approximately an order of magnitude slower in the ionic liquid, indicating a larger degree of solvent reorganisation during charge transfer in the RTIL.

However, the two studies undertaken by Lagrost *et al.*[71, 72] did not fully account for the ohmic drop and capacitative charging (see Chapter 1), which may have lead to the misinterpretation of results as k° values were calculated on the basis of peak to peak separations at macroelectrodes. More recent work by Fietkau *et* al. investigated several ferrocene derivatives in an ionic liquid using a high-speed channel microband electrode setup to minimise these factors[73]. The values of k° measured in this study were found to be approximately one order of magnitude lower than in acetonitrile and no correlation was observed between k° and the hydrodynamic radius in the RTIL. Subsequent studies by Belding *et al.*[74], on arenes and substituted ferrocenes, and by Long et al.[75], on phenylenediamines, in ionic liquids also found no correlation between k° and the hydrodynamic radius. These results illustrate the theoretical predictions that Marcus theory for outer-sphere electron transfer in dipolar solvents does not apply in ionic liquids[69, 76].

2.5.3 The Electrochemical Double Layer

The structure of the double layer of a solvent at the electrode-solution interface is another important property of ionic liquids, as the variation of the double layer with potential can affect electrode processes. This effect cannot be neglected (as mentioned in Chapter 1) as the charging current may swamp the Faradaic current if the concentration of electroactive species is low. The capacitance-potential curves for molten salts are asymmetric parabolic curves with a capacitance minimum at a potential equal to the point of zero charge (PZC). These types of capacitance-potential curves in dilute aqueous electrolytes are interpreted using a

diffuse double-layer model (as described in Chapter 1). However, this explanation cannot be valid for solvent-free ionic liquids because of their high ionic strength[77]. As such, a double layer model for ionic liquids was proposed in which there are multiple layers of cations and anions parallel to the electrode surface in which the excess surface charge is distributed, in agreement with that observed for high temperature molten salts[78]. The double layer was investigated in more detail in a review article[79] by Kornyshev who shortly thereafter also published a phenomenological model to describe the capacitance curves[80]. Kornyshev found that the capacitance curve has an asymmetric "bell-shape" character and that the maximum capacitance coincides with the PZC if the cation and anion are of the same size. However, he also stressed that capacitance curves for real ionic liquids will be deviate from the theory due to the non-spherical shape of RTIL ions[80]. Further evidence for this model was provided, by Kornyshev[81], *via* the use of Monte Carlo methods. This study showed that even at relatively high volume densities of ions, the neutral tails play the role of *latent voids* that can be replaced by charged groups with reorientations of the ions. Such rearrangements lead to compaction of the counter charge at moderate potentials, which provides the rising branch of capacitance. This becomes impossible at higher potentials due to steric effects as the double layer 'swells' and the capacitance starts to decrease. Even if only one of the ions has neutral moieties the two effects will occur at both cathodic and anodic polarizations of the electrode, at different potentials, resulting in the "double-hump camel shape"[81]. Experiments have since been

performed which then use Kornyshev's theory to fit the capacitance-potential curves, for example for the capacitance response of several electrode materials in the $[C_4mim][NTf_2]$ ionic liquid[82].

This chapter has provided a brief introduction on the physiochemical and electrochemical properties of ionic liquids, as well as describing some of the more practical aspects in using RTILs in electrochemical studies. The following chapter now describes the specific experimental details pertaining to the investigations presented in this thesis.

References

1. M. Freemantle, *An Introduction to Ionic Liquids*, The Royal Society of Chemistry, Cambridge, 1st edn., 2010.
2. A. P. Abbott and K. J. McKenzie, *Physical Chemistry Chemical Physics*, 2006, 8, 4265-4279.
3. D. S. Silvester and R. G. Compton, *Zeitschrift für Physikalische Chemie*, 2006, 220, 1247-1274.
4. J. S. Wilkes, *Green Chemistry*, 2002, 4, 73-80.
5. L. E. Barrosse-Antle, A. M. Bond, R. G. Compton, A. M. O'Mahony, E. I. Rogers and D. S. Silvester, *Chemistry – An Asian Journal*, 2010, 5, 202-230.
6. P. Hapiot and C. Lagrost, *Chemical Reviews*, 2008, 108, 2238-2264.
7. D. S. Silvester, L. Aldous, M. C. Lagunas, C. Hardacre and R. G. Compton, *Journal of Physical Chemistry B*, 2006, 110, 22035-22042.
8. F. Andre, P. Hapiot and C. Lagrost, *Physical Chemistry Chemical Physics*, 2010, 12, 7506-7512.
9. S. Ernst, K. R. Ward, S. E. Norman, C. Hardacre and R. G. Compton, *Physical Chemistry Chemical Physics*, 2013, 15, 6382-6389.
10. C. Lagrost, S. Gmouh, M. Vaultier and P. Hapiot, *The Journal of Physical Chemistry A*, 2004, 108, 6175-6182.
11. A. P. Doherty, L. Diaconu, E. Marley, P. L. Spedding, R. Barhdadi and M. Troupel, *Asia-Pacific Journal of Chemical Engineering*, 2012, 7, 14-23.
12. B. Murphy, P. Goodrich, C. Hardacre and M. Oelgemöller, *Green Chemistry*, 2009, 11, 1867.
13. M. J. Earle and K. R. Seddon, *Pure and Applied Chemistry*, 2000, 72, 1391-1398.
14. X. Sun, H. Luo and S. Dai, *Chem Rev*, 2012, 112, 2100-2128.
15. R. J. Gale, B. Gilbert and R. A. Osteryoung, *Inorg. Chem.*, 1978, 17, 2728-2729.
16. J. S. Wilkes, J. A. Levisky, R. A. Wilson and C. L. Hussey, *Inorg. Chem.*, 1982, 21, 1263-1264.

17. J. S. Wilkes and M. J. Zaworotko, *J. Chem. Soc., Chem. Commun.*, 1992, DOI: 10.1039/c39920000965, 965-967.
18. A. E. Visser, R. P. Swatloski, W. M. Reichert, J. H. Davis, Jr., R. D. Rogers, R. Mayton, S. Sheff and A. Wierzbicki, *Chem. Commun. (Cambridge)*, 2001, DOI: 10.1039/b008041l, 135-136.
19. J. H. Davis, Jr., *Chem. Lett.*, 2004, 33, 1072-1077.
20. J. H. Davis, Jr., eds. P. Wasserscheid and T. Welton, Wiley-VCH Verlag GmbH & Co. KGaA, 2003, pp. 33-40.
21. D. R. MacFarlane, P. Meakin, J. Sun, N. Amini and M. Forsyth, *The Journal of Physical Chemistry B*, 1999, 103, 4164-4170.
22. J. Sun, M. Forsyth and D. R. MacFarlane, *The Journal of Physical Chemistry B*, 1998, 102, 8858-8864.
23. D. R. MacFarlane, S. A. Forsyth, J. Golding and G. B. Deacon, *Green Chem.*, 2002, 4, 444-448.
24. R. E. Del Sesto, C. Corley, A. Robertson and J. S. Wilkes, *J. Organomet. Chem.*, 2005, 690, 2536-2542.
25. A. M. O'Mahony, D. S. Silvester, L. Aldous, C. Hardacre and R. G. Compton, *Journal of Chemical and Engineering Data*, 2008, 53, 2884-2891.
26. H. Ohno, in *Electrodeposition from Ionic Liquids*, eds. F. Endres, D. R. MacFarlane and A. P. Abbott, Wiley-VCH Verlag GmbH & Co. KGaA, 2008, DOI: 10.1002/9783527622917.ch3, pp. 47-82.
27. B. D. Fitchett, T. N. Knepp and J. C. Conboy, *J. Electrochem. Soc.*, 2004, 151, E219-E225.
28. W. Xu, L.-M. Wang, R. A. Nieman and C. A. Angell, *J. Phys. Chem. B*, 2003, 107, 11749-11756.
29. F. Endres and E. A. S. Zein, *Phys. Chem. Chem. Phys.*, 2006, 8, 2101-2116.
30. P. Wasserscheid and W. Keim, *Angew. Chem., Int. Ed.*, 2000, 39, 3772-3789.
31. J. Wang, Y. Tian, Y. Zhao and K. Zhuo, *Green Chem.*, 2003, 5, 618-622.
32. K. Machanova, A. Boisset, Z. Sedlakova, M. Anouti, M. Bendova and J. Jacquemin, *J. Chem. Eng. Data*, 2012, 57, 2227-2235.

33. A. B. McEwen, E. L. Ngo, K. LeCompte and J. L. Goldman, *J. Electrochem. Soc.*, 1999, 146, 1687-1695.
34. O. O. Okoturo and T. J. VanderNoot, *J. Electroanal. Chem.*, 2004, 568, 167-181.
35. J. Jacquemin, P. Husson, A. A. H. Padua and V. Majer, *Green Chem.*, 2006, 8, 172-180.
36. A. J. Bard and L. R. Faulkner, *Electrochemical Methods: Fundamentals and Applications*, Wiley, New York, 2nd edn., 2000.
37. D. R. McFarlane, J. Sun, J. Golding, P. Meakin and M. Forsyth, *Electrochimica Acta*, 2000, 45, 1271-1278.
38. H. Vogel, *Phys. Z.*, 1921, 22, 645-646.
39. G. Tammann and G. Veszi, *Z. Anorg. Allg. Chem.*, 1926, 150, 355-380.
40. G. S. Fulcher, *J. Am. Ceram. Soc.*, 1925, 8, 339-355.
41. M. C. Buzzeo, R. G. Evans and R. G. Compton, *ChemPhysChem*, 2004, 5, 1106-1120.
42. Y.-H. Tian, G. S. Goff, W. H. Runde and E. R. Batista, *The Journal of Physical Chemistry B*, 2012, 116, 11943-11952.
43. D. S. Silvester, E. I. Rogers, R. G. Compton, K. J. McKenzie, K. S. Ryder, F. Endres, D. MacFarlane and A. P. Abbott, in *Electrodeposition from Ionic Liquids*, eds. F. Endres, D. R. MacFarlane and A. P. Abbott, Wiley-VCH Verlag GmbH & Co. KGaA, 2008, DOI: 10.1002/9783527622917.ch11, pp. 287-351.
44. C. Maton, N. De Vos and C. V. Stevens, *Chemical Society Reviews*, 2013, 42, 5963-5977.
45. L. P. N. Rebelo, J. N. Canongia Lopes, J. M. S. S. Esperança and E. Filipe, *The Journal of Physical Chemistry B*, 2005, 109, 6040-6043.
46. M. J. Earle, J. M. S. S. Esperança, M. A. Gilea, J. N. C. Lopes, L. P. N. Rebelo, J. W. Magee, K. R. Seddon and J. A. Widegren, *Nature*, 2006, 439, 831-834.
47. U. Schröder, J. D. Wadhawan, R. G. Compton, F. Marken, P. A. Z. Suarez, C. S. Consorti, S. R. F. de and J. Dupont, *New J. Chem.*, 2000, 24, 1009-1015.

48. J. G. Huddleston, A. E. Visser, W. M. Reichert, H. D. Willauer, G. A. Broker and R. D. Rogers, *Green Chem.*, 2001, 3, 156-164.

49. J. A. Widegren, E. M. Saurer, K. N. Marsh and J. W. Magee, *J. Chem. Thermodyn.*, 2005, 37, 569-575.

50. J. A. Widegren, A. Laesecke and J. W. Magee, *Chem. Commun. (Cambridge, U. K.)*, 2005, DOI: 10.1039/b417348a, 1610-1612.

51. K. R. Seddon, A. Stark and M.-J. Torres, *Pure Appl. Chem.*, 2000, 72, 2275-2287.

52. M. C. Buzzeo, R. G. Evans and R. G. Compton, *Chemphyschem*, 2004, 5, 1106-1120.

53. P. Wasserscheid and T. Welton, *Ionic Liquids in Synthesis*, Wiley-VCH Verlag GmbH & Co. KGaA, 2003.

54. M. V. Merritt and D. T. Sawyer, *The Journal of Organic Chemistry*, 1970, 35, 2157-2159.

55. R. G. Evans, O. V. Klymenko, S. A. Saddoughi, C. Hardacre and R. G. Compton, *Journal of Physical Chemistry B*, 2004, 108, 7878-7886.

56. C. Zhao, A. M. Bond, R. G. Compton, A. M. O'Mahony and E. I. Rogers, *Analytical Chemistry*, 2010, 82, 3856-3861.

57. L. E. Barrosse-Antle, L. Aldous, C. Hardacre, A. M. Bond and R. G. Compton, *The Journal of Physical Chemistry C*, 2009, 113, 7750-7754.

58. L. E. Barrosse-Antle, C. Hardacre and R. G. Compton, *The Journal of Physical Chemistry B*, 2009, 113, 2805-2809.

59. E. I. Rogers, D. S. Silvester, D. L. Poole, L. Aldous, C. Hardacre and R. G. Compton, *J Phys Chem C*, 2008, 112, 2729-2735.

60. R. G. Evans, O. V. Klymenko, P. D. Price, S. G. Davies, C. Hardacre and R. G. Compton, *ChemPhysChem*, 2005, 6, 526-533.

61. D. S. Silvester, L. Aldous, C. Hardacre and R. G. Compton, *Journal of Physical Chemistry B*, 2007, 111, 5000-5007.

62. M. C. Buzzeo, O. V. Klymenko, J. D. Wadhawan, C. Hardacre, K. R. Seddon and R. G. Compton, *Journal of Physical Chemistry A*, 2003, 107, 8872-8878.

63. A. S. Barnes, E. I. Rogers, I. Streeter, L. Aldous, C. Hardacre and R. G. Compton, *The Journal of Physical Chemistry B*, 2008, 112, 7560-7565.

64. T. J. Stockmann, J. Zhang, J. C. Wren and Z. Ding, *Electrochim. Acta*, 2012, 62, 8-18.
65. K. R. J. Lovelock, A. Ejigu, S. F. Loh, S. Men, P. Licence and D. A. Walsh, *Phys. Chem. Chem. Phys.*, 2011, 13, 10155-10164.
66. R. Wibowo, L. Aldous, E. I. Rogers, S. E. Ward Jones and R. G. Compton, *The Journal of Physical Chemistry C*, 2010, 114, 3618-3626.
67. E. O. Barnes, A. M. O'Mahony, S. R. Belding and R. G. Compton, *J. Chem. Eng. Data*, 2010, 55, 2219-2224.
68. A. W. Taylor, F. Qiu, J. Hu, P. Licence and D. A. Walsh, *J. Phys. Chem. B*, 2008, 112, 13292-13299.
69. R. M. Lynden-Bell, *Electrochemistry Communications*, 2007, 9, 1857-1861.
70. H. Liu, Y. Liu and J. Li, *Physical Chemistry Chemical Physics*, 2010, 12, 1685-1697.
71. C. Lagrost, L. Preda, E. Volanschi and P. Hapiot, *J. Electroanal. Chem.*, 2005, 585, 1-7.
72. C. Lagrost, D. Carrie, M. Vaultier and P. Hapiot, *J. Phys. Chem. A*, 2003, 107, 745-752.
73. N. Fietkau, A. D. Clegg, R. G. Evans, C. Villagran, C. Hardacre and R. G. Compton, *ChemPhysChem*, 2006, 7, 1041-1045.
74. S. R. Belding, N. V. Rees, L. Aldous, C. Hardacre and R. G. Compton, *J. Phys. Chem. C*, 2008, 112, 1650-1657.
75. J. S. Long, D. S. Silvester, A. S. Barnes, N. V. Rees, L. Aldous, C. Hardacre and R. G. Compton, *J. Phys. Chem. C*, 2008, 112, 6993-7000.
76. R. M. Lynden-Bell, *The Journal of Physical Chemistry B*, 2007, 111, 10800-10806.
77. C. Nanjundiah, S. F. McDevitt and V. R. Koch, *J. Electrochem. Soc.*, 1997, 144, 3392-3397.
78. A. D. Graves and D. Inman, *J. Electroanal. Chem. Interfacial Electrochem.*, 1970, 25, 357-372.
79. A. A. Kornyshev, *J. Phys. Chem. B*, 2007, 111, 5545-5557.
80. M. V. Fedorov and A. A. Kornyshev, *J. Phys. Chem. B*, 2008, 112, 11868-11872.

81. M. V. Fedorov, N. Georgi and A. A. Kornyshev, *Electrochemistry Communications*, 2010, 12, 296-299.

82. C. Cannes, H. Cachet, C. Debiemme-Chouvy, C. Deslouis, S. J. de, N. C. Le and V. A. Zinovyeva, *J. Phys. Chem. C*, 2013, 117, 22915-22925.

3. Experimental Methods

This chapter presents details on the chemical reagents and room temperature ionic liquids used throughout this thesis, as well as details of general experimental methodology and apparatus. Descriptions of experimental procedures and apparatus specific to individual investigations will be given in the relevant results chapters.

3.1 Chemical Reagents

The structures of the room temperature ionic liquids used throughout the following experiments are shown below in Figure 1. These and other compounds used in this thesis are also listed below in Table 4.

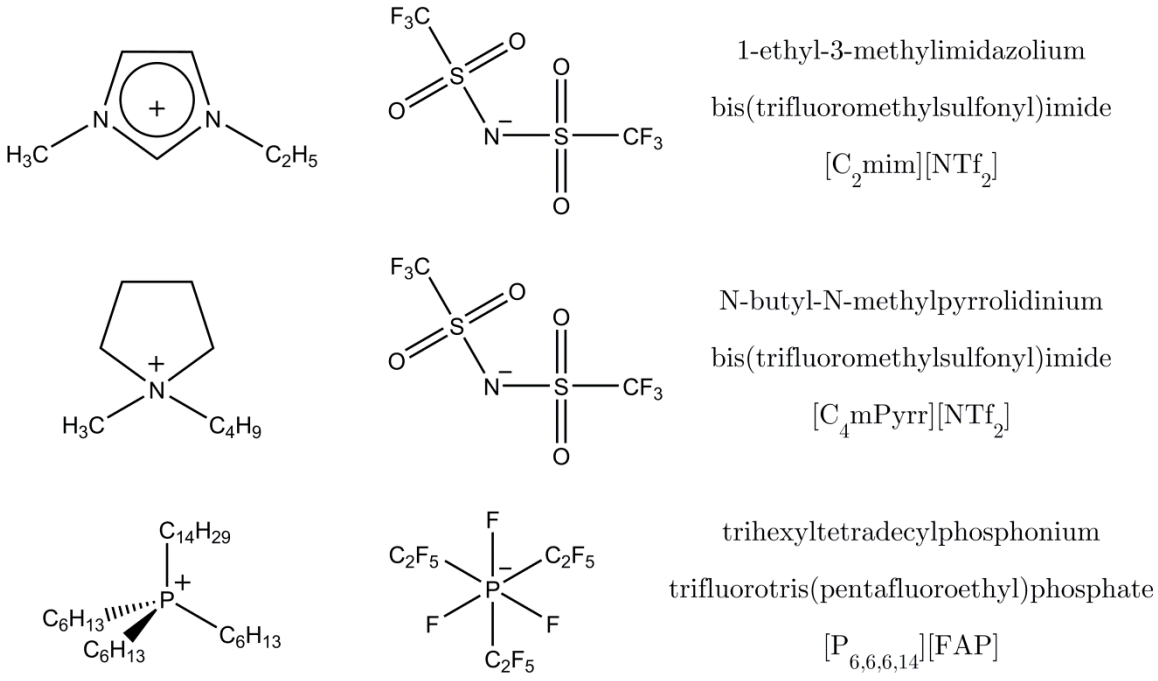
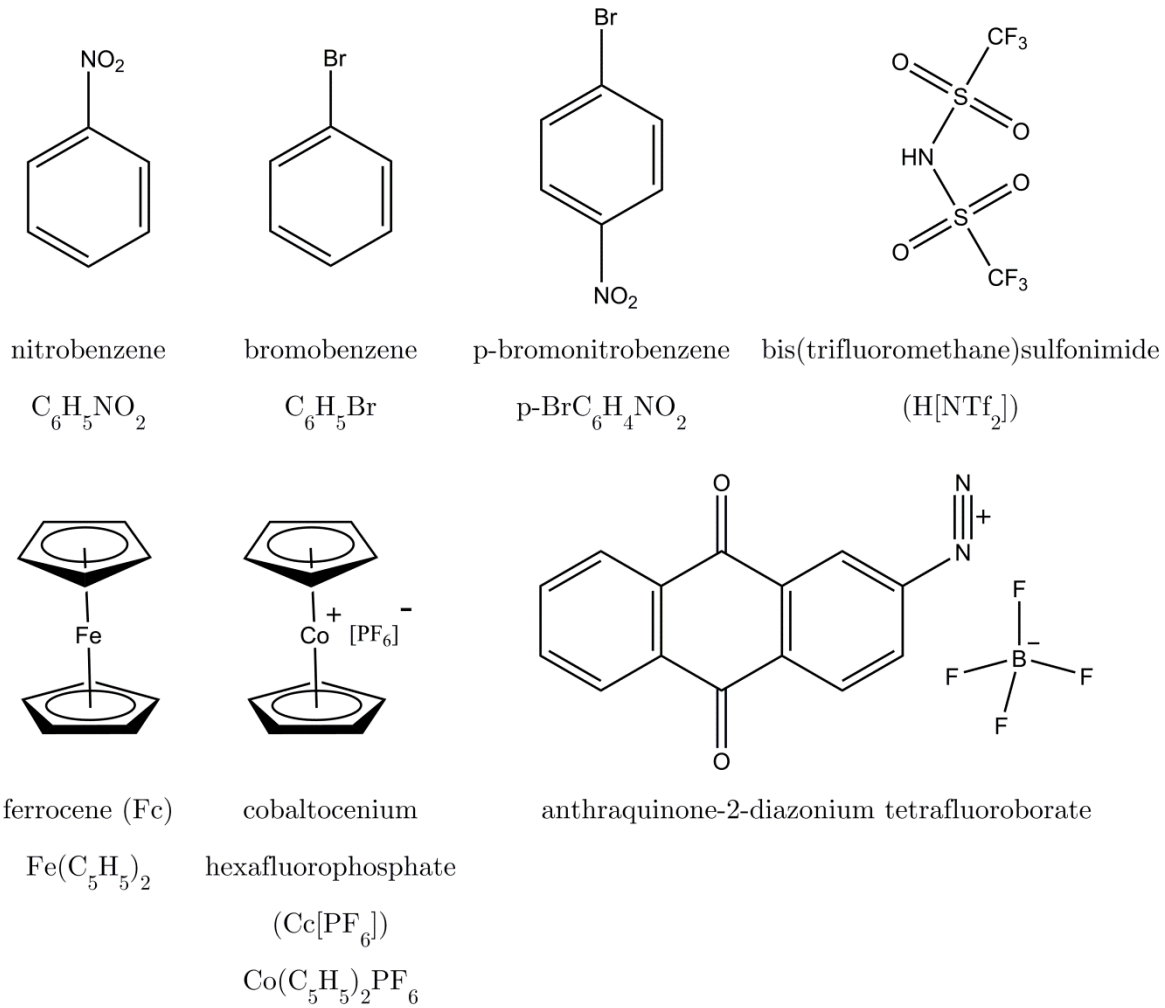


Figure 1 – Chemical structures of the room temperature ionic liquids in Table 4.

The structures of some of the chemical reagents used in the investigations in this thesis are presented below in Figure 2, while a table of all the chemicals and room temperature ionic liquids used, accompanied by manufacturer and purity information is given below in Table 4.



nitrobenzene $C_6H_5NO_2$

bromobenzene C_6H_5Br

p-bromonitrobenzene $p\text{-}BrC_6H_4NO_2$

bis(trifluoromethane)sulfonimide $(H[NTf_2])$

ferrocene (Fc) $Fe(C_5H_5)_2$

cobaltocenium hexafluorophosphate $(Cc[PF_6])$ $Co(C_5H_5)_2PF_6$

anthraquinone-2-diazonium tetrafluoroborate

Figure 2 - Chemical structures of a selection of reagents in Table 4.

Table 4 – List of chemicals used throughout this thesis, including their purities and suppliers.

Chemical Name	Formula / Abbreviation	Purity	Supplier
1-bromo-4-nitrobenzene	p-$BrC_6H_4NO_2$	99 %	Aldrich
1-ethyl-3-methylimidazolium bis(trifluoromethylsulfonyl)imide	$[C_2mim][NTf_2]$	98 %	Merck KGaA
2-aminoanthraquinone	AQ-NH_2	85 - 90 %	Sigma-Aldrich
acetonitrile	MeCN	≥ 99.9 %	Sigma-Aldrich
anthraquinone-2-diazonium tetrafluoroborate	AQ-$N_2^+BF_4^-$	-	synthesised
benzoic acid	C_6H_5COOH	> 99.5 %	Fluka
bis(trifluoromethane)sulfonimide	$H[NTf_2]$	> 95 %	Fluka
bromobenzene	C_6H_5Br	99 %	Aldrich
carbon dioxide	CO_2	99.995 %	BOC
cobaltocenium hexafluorophosphate	$Co(C_5H_5)_2PF_6$/$Cc[PF_6]$	98 %	Strem
deionised water	H_2O	18.2 MΩ·cm	Millipore
dichloromethane	DCM	99.9 %	Fisher Sci.
ethanol	EtOH	≥ 99.8 %	Sigma-Aldrich
ferrocene	$Fe(C_5H_5)_2$ / Fc	98 %	Aldrich
N,*N*-dimethylformamide	DMF	≥ 95 %	Fisher Sci.
N-butyl-*N*-methylpyrrolidinium bis(trifluoromethylsulfonyl)imide	$[C_4mPyrr][NTf_2]$	-	synthesised
nitrobenzene	$C_6H_5NO_2$	> 99 %	Aldrich
nitrogen (oxygen-free)	N_2	> 99.998 %	BOC
nitrosonium tetrafluoroborate	$NOBF_4$	95 %	Sigma-Aldrich
oxygen	O_2	> 99.5 %	BOC
potassium hydroxide	KOH	85 %	Sigma-Aldrich
silver trifluoromethanesulfonate	Ag[Otf]	> 99.95 %	Aldrich
tetra-*n*-butylammonium perchlorate	TBAP	≥ 99 %	Sigma-Aldrich
trihexyltetradecylphosphonium trifluorotris(pentafluoroethyl)phosphate	$[P_{6,6,6,14}][FAP]$	-	synthesised
zinc oxide	ZnO	99 %	Sigma-Aldrich
zinc(II) bis(trifluoromethylsulfonyl)imide	$Zn[NTf_2]_2$	-	synthesised

3. Experimental Methods

Anthraquinone-2-diazonium tetrafluoroborate was synthesised according to the method of Milner[1]; 2-aminoanthraquinone (0.5 g) was added to nitrosonium tetrafluoroborate (0.4 g, *ca.* 50% molar excess) in dichloromethane (50 mL). The resulting slurry was kept in an ice-water bath and stirred for one hour before the dichloromethane was removed under vacuum. The resulting anthraquinone-2-diazonium tetrafluoroborate product was stored at -5 °C.

$Zn[NTf_2]_2$ was synthesised *via* a neutralization reaction by adding a 50% molar excess of ZnO to an aqueous solution of $H[NTf_2]$ and stirring overnight until pH-neutral[2, 3]. The resulting slurry was then filtered through a sintered glass frit and the (clear and colourless) filtrate was dried under rotary evaporation and then high vacuum ($P = 0.018 \pm 0.002$ mbar) overnight to yield large white flakes.

All aqueous solutions were prepared using deionised water with resistivity equal to 18.2 MΩ·cm at 25 °C (Millipore water systems). Ionic liquid solutions containing ferrocene were prepared by adding 50 μL of ~10 mM ferrocene in MeCN to 50 μL of the ionic liquid, followed by the removal of MeCN under vacuum. Unless otherwise specified, all other ionic liquid solutions were prepared via the direct dissolution of compounds into the ionic liquid. Any gasses introduced to the RTIL solutions were first passed through a column of molecular sieves (mixture of 3 & 4 Å, Acros Organics) immediately before use in order to remove any residual water.

The $[C_2mim][NTf_2]$ ionic liquid was purchased from Merck, however, the remaining RTILs were synthesised by Dr. Sarah Norman, under the supervision of

Prof. Christopher Hardacre at the Queen's University Ionic Liquids Laboratory. The most common method of synthesising room temperature ionic liquids is *via* metathesis of a halide salt of the cation with either silver, group I metal or ammonium salt of the anion[4]. Accordingly, both $[C_4mPyrr][NTf_2]$[5] & $[P_{6,6,6,14}][FAP]$[6] were synthesised *via* the standard literature procedures for their metatheses.

3.2. Instrumentation and Electrodes

All electrochemical measurements were performed in a thermostated Faraday cage (25 ± 1 °C) using a μAutolab Type II computer-controlled potentiostat (EcoChemie) in conjunction with standard two or three electrode configurations. All of the voltammetry presented was obtained using normal staircase cyclic voltammetry using a potential step of *ca.* 1 to 2 mV and α value of 0.3.

Various working electrodes, both macrodisk and microdisk, were employed throughout the experiments reported in this thesis. The macroelectrodes used were boron-doped diamond (r = 1.5 mm, ~10^{20} cm^{-3} boron, Windsor Scientific, D-191-SA) and glassy carbon (r = 1.5 mm, BASi). The microelectrodes used were glassy carbon, (r ≈ 7.5 μm, Princeton Applied Research), Platinum (r ≈ 5 μm, BASi) and zinc (r ≈ 12.5 μm, see Chapter 7). Microelectrode radii were generally calibrated by measuring the chronoamperometric transients of solutions with a known concentration of Fc (*ca.* 2 mM, with 0.1 M TBAP) in MeCN and then fitting the transients using the Shoup-Szabo expression[7], as described below in

section 3.4, with the known values for the concentration and diffusion coefficient of Fc[8] (2.3×10^{-9} m^2 s^{-1}) fixed, to fit the radius.

Experiments employing a quasi-reference electrode were conducted using a silver wire (0.5 mm diameter, 99.99%, Goodfellow). Experiments using a three-electrode configuration employed either a platinum wire (0.75 mm diameter, 99.9%, Goodfellow), coiled platinum wire (0.75 mm diameter, 99.9%, Goodfellow) or platinum mesh (99.9%, Goodfellow) counter electrode, as appropriate for the radius of the working electrode. In all of these cases the reference electrode was a Ag/Ag^+ reference electrode, prepared *via* a modified version of the method of Meng et al.[9], by attaching a 5Å, 1.6mm diameter molecular sieve (Aldrich) to the end of a cut-down glass Pasteur pipette (VWR International Ltd) using PTFE heatshrink (TE Connectivity), see Figure 3. The Ag/Ag^+ reference electrode was then filled with a 20 mM solution of Ag[OTf] in $[C_4mPyrr][NTf_2]$ and a silver wire was immersed in the solution. These reference electrodes then yielded reproducible formal potentials (Pt working electrode in $[C_4mPyrr][NTf_2]$) of -363 ± 4 mV for the ferrocene|ferrocenium couple and -1691 ± 5 mV for the cobaltocenium|cobaltocene couple.

Prior to use, working electrodes were polished using 1, 0.3 and 0.05 μm alumina lapping compounds (Buehler) on soft lapping pads (Buehler) and then placed in deionised water (or EtOH in the case of zinc electrodes) in an ultrasonic bath for *ca.* 2 minutes to remove any adsorbed alumina particles. The electrodes were then rinsed with MeCN and dried using compressed nitrogen. Before use, the

platinum wires and meshes were cleaned in a hot Bunsen flame and then rinsed with MeCN and dried under nitrogen. Silver wires were lightly polished using P1000 silicon carbide paper (Flexovit) and then rinsed with MeCN und dried under nitrogen.

3.3 Apparatus

Experiments were typically prepared by placing 50 μL of the desired sample solution into a sample chamber on top of the electrode, constructed by attaching a section of disposable micropipette tip (VWR International Ltd) over the electrode tip.

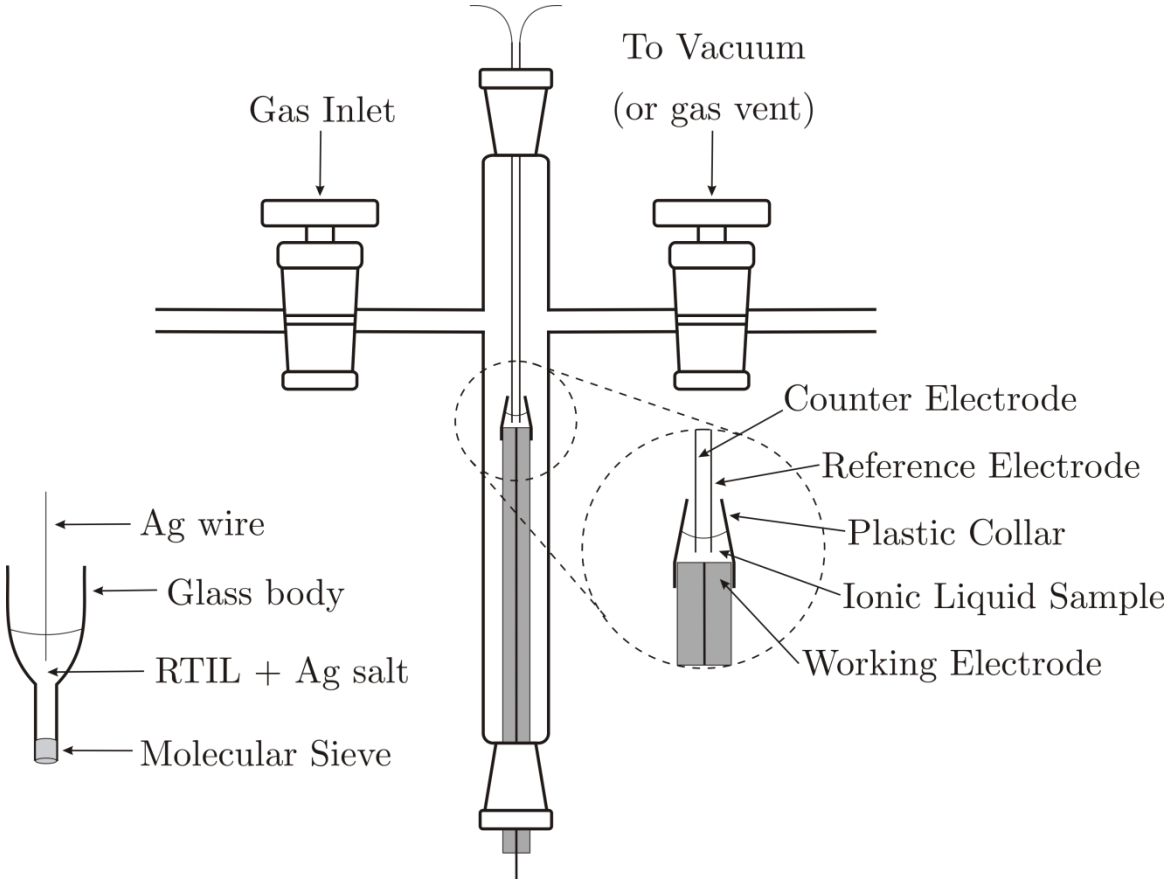


Figure 3 - Typical experimental setup for studying RTIL solutions.

The working electrode and sample were then placed into a glass T-shaped cell, described previously[10] and shown above in Figure 3, and the counter and reference electrodes fed into the sample from above. One arm of the T-shaped cell was then connected to a rotary vacuum pump (Edwards) and the sample was placed under vacuum ($P = 0.018 \pm 0.002$ mbar) for at least 2 hours before measurement and remained *in-vacuo* for the duration of the experiment. System are studied *in-vacuo* to reduce the water[11] and oxygen[12] concentrations in the RTIL to acceptably low levels. Moreover, several gasses which were previously thought to be electrochemically benign, such as argon, nitrogen and carbon dioxide, have since been shown to alter the mass transport properties of RTILs[12-14].

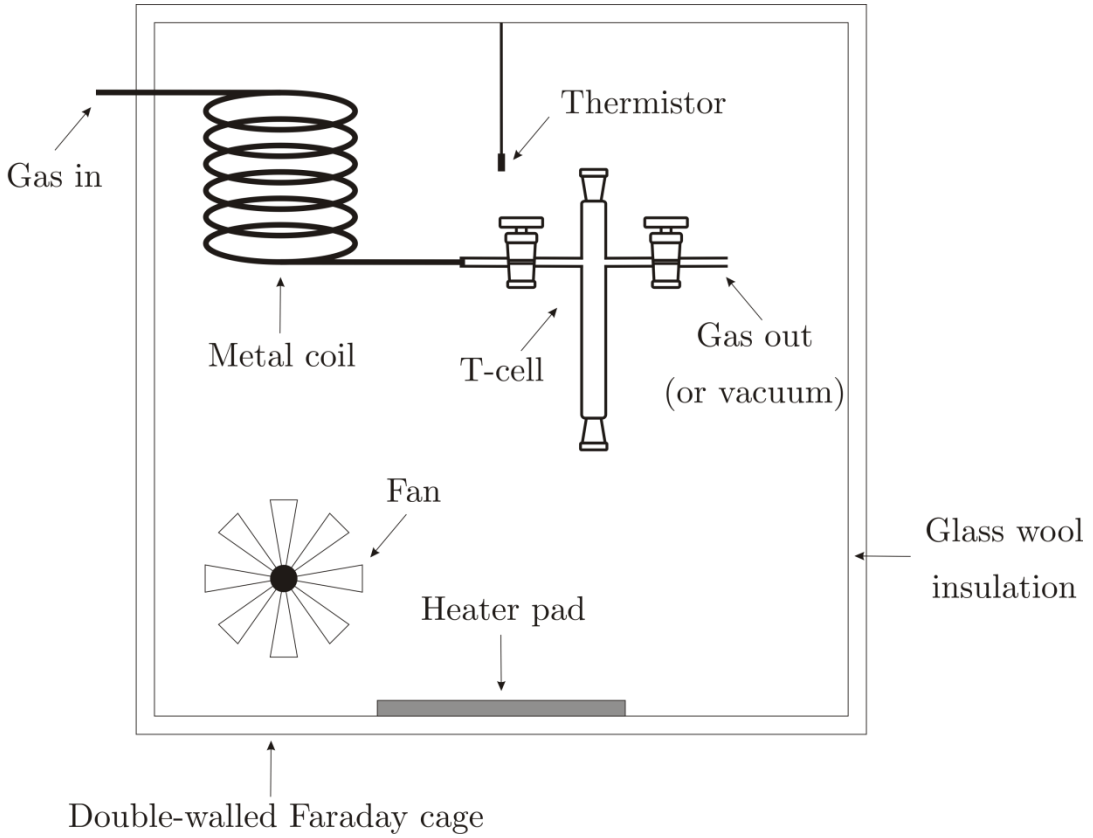


Figure 4 - The thermostated Faraday cage.

Figure 4 shows the construction of the thermostated Faraday cage. The temperature is measured through the thermistor and a temperature controller (CAL3300, CAL Controls Ltd) modulates the power applied to the heater pad *via* a PID loop. The setup shown in Figure 4, employing the T-cell shown in Figure 3 was used in all of the experiments described in this thesis where the volume of solution under study was small. For experiments requiring larger volumes, the T-cell was replaced with the cell shown in Figure 5, where the electrodes and Pasteur pipettes are held in place using Parafilm and gas flow to the bubbler is stopped before measurement by closing a valve.

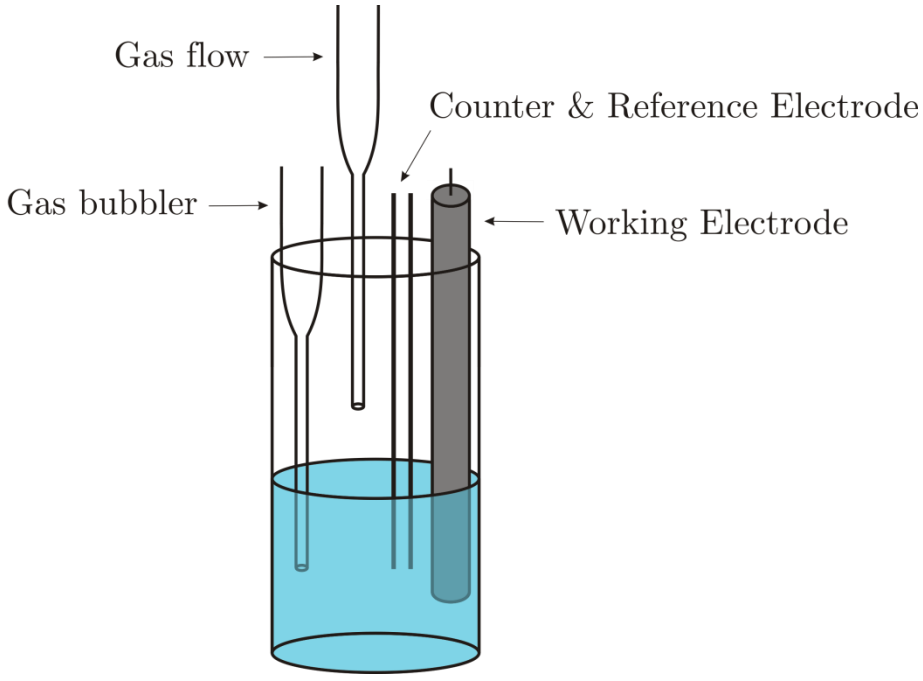


Figure 5 - Large volume cell.

3.4 Chronoamperometric Experiments

Chronoamperometric transients, unless stated otherwise, were measured using a measurement time of 5 s and a sample time of 0.01 s. For these experiments, the potential was held at a point at which no Faradaic current is passed for 5 s, after which the potential was stepped to a point sufficiently 'past' the voltammetric peak in order to ensure that the process is diffusion-limited. Chronoamperometric transients were then analysed *via* the automated iterative fitting of the empirically determined Shoup and Szabo expression[7], described below, using the OriginPro 8 software package.

$$i = 4nFcDr \cdot f(\tau) \tag{3.1}$$

$$f(\tau) = 0.7854 + 0.8863\tau^{-1/2} + 0.2146\exp(-0.7823\tau^{-1/2}) \tag{3.2}$$

$$\tau = \frac{4Dt}{r^2} \tag{3.3}$$

where the current, i, is a function of n; the number of electrons transferred, F; the Faraday constant, c; the initial concentration, D; the diffusion coefficient, r; the electrode radius and τ; the dimensionless time. The Shoup and Szabo expression has been shown to correctly and simultaneously predict D and (nc) with a maximum error of less than 0.6%[7], provided that optimal transient times are used[15]. In fitting experimental transients, the value of r (previously calibrated) was fixed and the software performed up to a maximum of 400 iterations, although generally only 10 or so were required, to fit D and c to the experimental transients, until the fit converged to the optimal parameters.

References

1. D. J. Milner, *Synth. Commun.*, 1992, 22, 73-82.
2. H. Kobayashi, J. Nie and T. Sonoda, *Chemistry Letters*, 1995, 24, 307-308.
3. J. Nie, H. Kobayashi and T. Sonoda, *Catalysis Today*, 1997, 36, 81-84.
4. T. Welton, *Chemical Reviews*, 1999, 99, 2071-2084.
5. D. R. MacFarlane, P. Meakin, J. Sun, N. Amini and M. Forsyth, *The Journal of Physical Chemistry B*, 1999, 103, 4164-4170.
6. R. E. Del Sesto, C. Corley, A. Robertson and J. S. Wilkes, *Journal of Organometallic Chemistry*, 2005, 690, 2536-2542.
7. D. Shoup and A. Szabo, *Journal of Electroanalytical Chemistry and Interfacial Electrochemistry*, 1982, 140, 237-245.
8. M. Sharp, *Electrochimica Acta*, 1983, 28, 301-308.
9. Y. Meng, L. Aldous, S. R. Belding and R. G. Compton, *Physical Chemistry Chemical Physics*, 2012, 14, 5222-5228.
10. R. G. Evans, O. V. Klymenko, P. D. Price, S. G. Davies, C. Hardacre and R. G. Compton, *ChemPhysChem*, 2005, 6, 526-533.
11. A. M. O'Mahony, D. S. Silvester, L. Aldous, C. Hardacre and R. G. Compton, *Journal of Chemical and Engineering Data*, 2008, 53, 2884-2891.
12. C. Zhao, A. M. Bond, R. G. Compton, A. M. O'Mahony and E. I. Rogers, *Analytical Chemistry*, 2010, 82, 3856-3861.
13. L. E. Barrosse-Antle, C. Hardacre and R. G. Compton, *The Journal of Physical Chemistry B*, 2009, 113, 2805-2809.
14. L. E. Barrosse-Antle, L. Aldous, C. Hardacre, A. M. Bond and R. G. Compton, *The Journal of Physical Chemistry C*, 2009, 113, 7750-7754.
15. L. Xiong, L. Aldous, M. C. Henstridge and R. G. Compton, *Analytical Methods*, 2012, 4, 371.

4. Influence of Cation Size on Voltammetry in RTILs

Voltammetry in conventional molecular solvents, both aqueous and aprotic, generally employs charge carriers, in the form of supporting electrolyte, which are relatively small and have appropriately high diffusion coefficients, as well as being electrochemically inert in the potential window of the solvent. However, given that room temperature ionic liquids are generally considerably bulkier than the charge carriers employed in conventional aqueous and aprotic systems, the effect of charge carrier size (RTIL cations and anions) may have significant effects on the voltammetric response observed in these solvents, especially for surface-bound species.

This chapter thus examines the effects of varying the RTIL cation size on the reduction of model surface-bound 2-anthraquinonyl groups (AQ_L) attached to glassy carbon microelectrodes. The electroactivity of the anthraquinonyl films was found to vary with the size of the RTIL cation, in that the extent of the $AQ_L^{\bullet -}|AQ_L^{2-}$ reduction was found to decrease with increasing cation size. Two distinct one-electron redox waves were observed in RTILs composed of smaller cations, while only a single one-electron wave was observed in RTILs composed of larger cations. It was thus proposed that complete reduction of the film cannot be achieved using larger RTIL cations, as steric hindrance within the film inhibits charge compensation. The work presented in this chapter has been published in *Chemical Physics Letters*[1]

4.1 Introduction

As mentioned above, the effect of charge carrier size may have significant effects on the voltammetric response observed for surface-bound species in room temperature ionic liquids. In addition, modified electrodes are of interest for a range of sensing and electrocatalytic applications. This is largely due to the ease with which desired functionality may be introduced, with both electrochemical[2-5] and chemical[6, 7] routes available. The aim of these techniques is usually to deposit a uniform layer of material on the electrode surface. It should be noted that this process often results in the deposition of multilayers[8], which are voltammetrically active due to their porosity[9-11]. Surface-bound films have been prepared electrochemically using room-temperature ionic liquids (RTILs) as the electrolyte[12, 13]. However, the electroactivity of such films has not been investigated in RTIL media, nor has a comparative study been performed as a function of RTIL size or structure.

Quinones, such as 9,10-anthraquinone (AQ), have been used previously to derivatise carbon powder electrodes for use as reagentless pH sensors[14, 15] and in synthesis using room temperature ionic liquids (RTILs) as solvents[16]. Quinones are also useful model redox probes, as they are known to exhibit well understood electrochemistry in conventional protic and aprotic solvents[17]. Various quinones have also been investigated, to a lesser extent, in ionic liquids[18-20]. 9,10-anthraquinone is reduced in ionic liquids via two one-electron reduction

steps, forming first the radical anion and then the dianion, as shown in equations (4.1) and (4.2).

$$AQ + e^- \rightleftarrows AQ^{\bullet -} \tag{4.1}$$

$$AQ^{\bullet -} + e^- \rightleftarrows AQ^{2-} \tag{4.2}$$

Carter and Osteryoung investigated the behaviour of AQ in $AlCl_3$/1-ethyl-3-methylimidazolium chloride ($[C_2mim]Cl$) mixtures at an elevated temperature[21]. Wang *et al.* studied the electrochemistry of the hydroquinone | benzoquinone system in 1-ethyl-3-methylimidazolium bis(trifluoromethylsulfonyl)imide ($[C_2mim][NTf_2]$)[18, 19], while Barnes *et al.* considered the electrochemical oxidation of catechol and dopamine in $[C_2mim][NTf_2]$[20].

More recently, Nikitina *et al.* investigated the electrochemistry of tetrachloro-1,2-benzoquinone, 2-methyl-1,2-benzoquinone and 9,10-anthraquinone in 1-butyl-3-methylimidazolium tetrafluoroborate ($[C_4mim][BF_4]$) and 1-butyl-3-methylimidazolium hexafluorophosphate ($[C_4mim][PF_6]$)[22].

Previous work involving quinones in RTILs has focused on solution-phase electrochemistry, which has on occasion been hindered by the poor solubility of quinones in certain RTILs[22]. In one case, this has been overcome by incorporating the quinone into the RTIL itself[23]. The solubility limitation can also be overcome by investigating surface-bound species, with surface-bound 9,10-anthraquinone having been investigated previously in aqueous systems[24]. Quinones may be attached to electrodes by a variety of methods. The most useful with respect to

carbon electrodes is the use of diazonium salt chemistry[25] which has been used previously to attach 9,10-anthraquinone to edge plane pyrolytic graphite electrodes[24]. The electrochemical reduction of diazonium salts has proven to be extremely well suited to cases involving macroelectrodes[8, 26-28], more recently in RTILs[12, 13], and has been used to modify metallic microelectrodes[29]. However, this method may not be appropriate for the modification of carbon microelectrodes as diffusion to the periphery of a microelectrode is much greater than to sites in the bulk surface[30] and certain carbon sites have been shown to modify preferentially via diazonium electroreduction[9, 31].

In the present work, a glassy carbon microelectrode was chemically modified with a layer of 2-anthraquinonyl groups. The resulting modified electrode was characterised in several RTILs, covering a relatively wide range of cation sizes. The resulting voltammetry was strongly influenced by the nature of the RTIL employed.

4.2 Experimental

The glassy carbon working electrode was modified using anthraquinone-2-diazonium tetrafluoroborate *via* the standard thermal decomposition method[24]. The electrode was immersed in a stirred solution of *ca.* 0.002 g of the diazonium salt in 100 mL of de-ionised water for 30 minutes. This solution, initially prepared in an ice-water bath, was placed into a temperature-controlled Faraday cage set at 25 °C, immediately prior to the immersion of the electrode. After 30 minutes,

the modified electrode was removed from solution and immediately rinsed with acetonitrile, DMF, and deionised water to remove any unreacted starting material and limit further modification. Anthraquinone-2-diazonium tetrafluoroborate solutions of higher concentration (*ca.* 6 mM) and modifications from 1 to 60 minutes were also performed, but yielded less optimal results and are therefore not included.

Voltammetric scans were performed using both conventional staircase cyclic voltammetry and current integrative voltammetry and no significant changes were observed. The voltammetry presented was obtained using normal staircase cyclic voltammetry using a potential step of 2 mV and α value of 0.3.

Ionic liquid samples were prepared with a ferrocene redox marker by adding 50 μL of ionic liquid and 50 μL of ~10 mM Fc in MeCN. The 0.8 M $[C_2mim][NTf_2]$ sample in $[C_4mPyrr][NTf_2]$ was prepared, as above, using 12.9 μL $[C_2mim][NTf_2]$, 50 μL $[C_4mPyrr][NTf_2]$ and 50 μL Fc in MeCN. Samples were left under vacuum for at least eight hours prior to any measurements.

4.3 Results and Discussion

A glassy carbon microelectrode was modified via the literature method for the thermal decomposition of anthraquinone-2-diazonium tetrafluoroborate[32], shown in equation (4.3), and this reaction was optimised, by varying reagent concentration and reaction time, in order to reproducibly form an anthraquinonyl (AQ_L) layer with good signal-to-noise response.

$$R_1N \equiv N^+ + R_2COO^- \rightarrow R_2COOR_1 + N_2 \qquad (4.3)$$

where in the present case, R_1 is the anthraquinone moiety which attaches to carboxylic groups on the carbon, R_2, surface, evolving nitrogen in the process.

Surface coverages were determined by integrating the 1st peak ($AQ_L|AQ_L^{\bullet -}$) reduction scan to determine the total reductive charge, Q, and then substituting this value into equation (4.4),

$$\frac{m}{A} = \frac{Q}{n \cdot F} \cdot \frac{1}{A} \qquad (4.4)$$

where m refers to the number of moles of AQ, n the number of electrons transferred in the reduction, F is the Faraday constant and A the area of the microelectrode.

This method yields the minimum surface coverages, which were found to vary over the experiments conducted from approximately 1.4×10^{-9} to 2.1×10^{-9} mol cm^{-2} as calculated for scans at 250 mV s^{-1}. These coverages are higher than those reported by Seinberg et al.[33], however this is likely due to the differing electrode sizes and solution concentrations employed, as well as the fact that the present study employed 2-anthraquinonyl groups while Seinberg *et al.* used anthraquinonyl groups bound via the C_1 carbon.

The theoretical coverage of a densely-packed monolayer (with maximum possible packing) was calculated from x-ray bond lengths[34] and non-bonded van der Waals radii[35]. The calculation involved the assumption that the

anthraquinonyl groups were in a planar conformation, with the molecular plane perpendicular to the electrode surface and anchored at an angle of 30° *via* the C_2 carbon atom. These calculations show that a densely-packed monolayer, with maximum possible packing, would yield a surface coverage of 3.45×10^{-10} mol cm^{-2} if uniformly spread. If surface modification was to occur in localised patches, as seen during electrochemical deposition on highly ordered pyrolytic graphite[31], the same coverage would lead to patches consisting of multiple layers. Thus, in the experiments performed, the surface-averaged coverage was determined to vary between 4 and 6 molecular layers. However, since packing is likely to be less dense than that encountered in the crystalline phase, the surface layer was probably composed of more than 4 to 6 molecular layers.

Figure 6 displays a CV of an unmodified (blank) glassy carbon microelectrode (r = 7.5 μm) in the $[C_4mPyrr][NTf_2]$ ionic liquid at a scan rate of 250 mV s^{-1}. In addition, Figure 6 displays a CV of the same electrode in the $[C_4mPyrr][NTf_2]$ ionic liquid after being modified with a surface-immobilized layer of anthraquinonyl groups, with average surface coverage *ca.* 1.4×10^{-9} mol cm^{-2}. The figure shows that, in $[C_4mPyrr][NTf_2]$, the two one-electron $AQ_L|AQ_L^{\bullet-}$ and $AQ_L^{\bullet-}|AQ_L^{2-}$ waves have peak separations of *ca.* 100 and 120 mV respectively. The 1st reduction peak, showing the reduction of AQ_L to $AQ_L^{\bullet-}$, was found to have a full-width half-maximum of *ca.* 320 mV. This is larger than the value of $90.6/n$ mV (25°C) expected for an ideal surface-bound system[36], although experimental full-width half-maxima have been shown to be larger than this value for a number

of reasons[37]. The results of a 'background subtraction', subtracting the blank scan from the modified-electrode scan, are also shown in Figure 6. The background-subtracted scans show improved resolution of the AQ_L features, though it is evident that modification of the glassy carbon surface with AQ_L groups results in an additional total double-layer capacitance of approximately 85%, as measured at 0.3V *vs.* Fc | Fc^+.

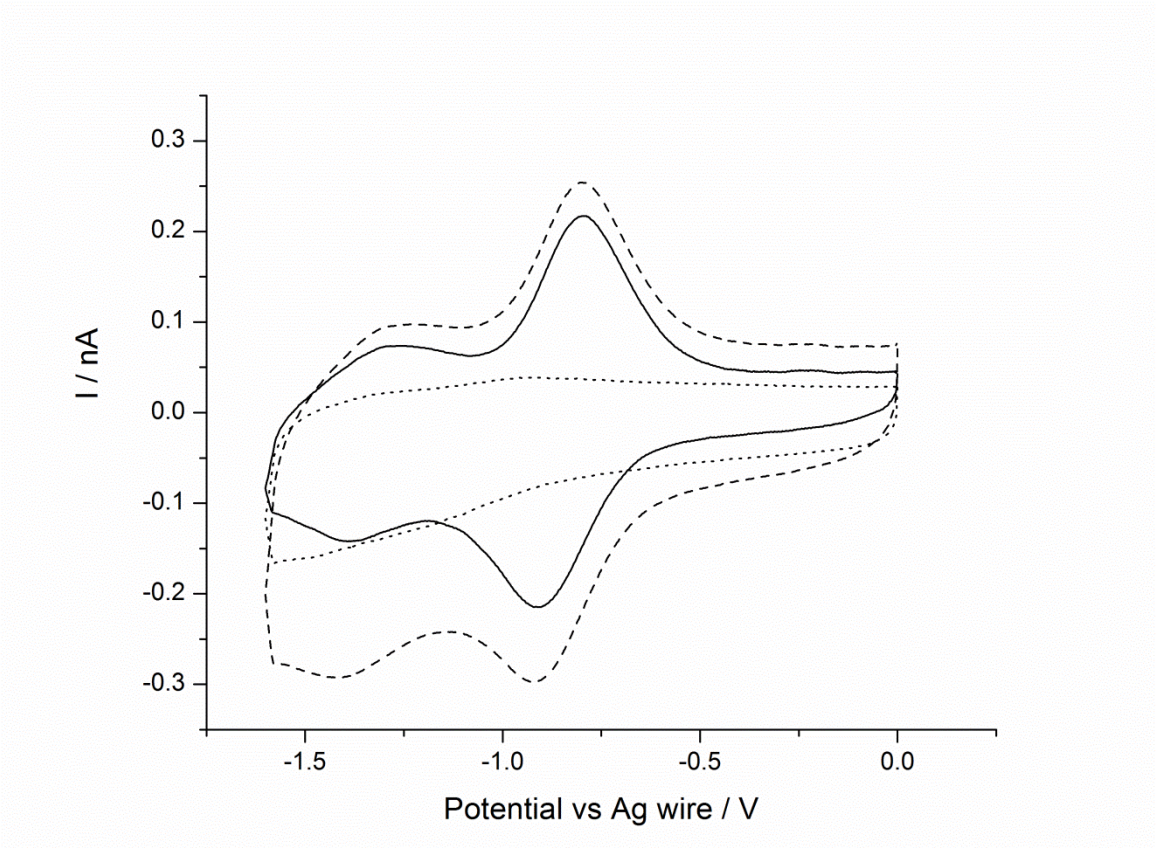


Figure 6 - CVs recorded at 250 mV s^{-1} in $[C_4mPyrr][NTf_2]$ for (···) a blank glassy carbon microelectrode (r = 7.5μm), (---) the same glassy carbon microelectrode after being modified with a surface-bound layer of AQ_L groups, and (—) the AQ_L signal after background subtraction.

All CVs, other than Figure 6, were referenced to the half-wave potential of the ferrocene | ferrocenium couple, after making the necessary corrections for the non-

equivalent diffusion coefficients of ferrocene and ferrocenium[38, 39], through the addition of 10 mM ferrocene (Fc) as an internal reference. All subsequent CVs were also background-subtracted.

Figure 7 displays the effect of varying scan rate on the voltammetry of an AQ_L-modified electrode in $[C_4mPyrr][NTf_2]$. Figure 7 shows two distinct one-electron reductions at each scan rate studied.

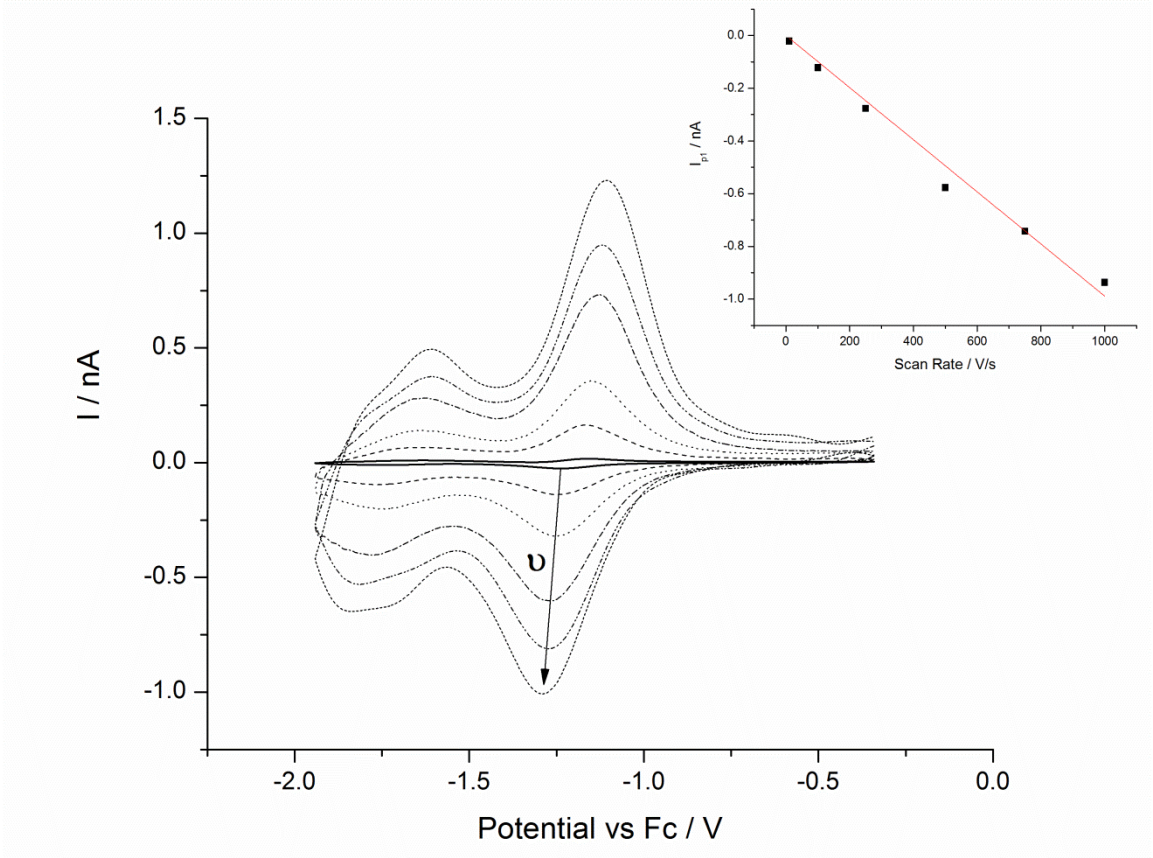


Figure 7 - CVs of surface-bound AQ_L groups on a glassy carbon microelectrode (r = 7.5μm) in $[C_4mPyrr][NTf_2]$ containing a ~10mM ferrocene redox marker (not shown), illustrating the linear dependence of peak height on scan rate for the reduction of AQ_L to $AQ_L^{\bullet-}$. The scan rates investigated were 10, 100, 250, 500, 750 and 1000 mV s^{-1}.

The two-step reduction, at 250 mV s^{-1}, of $AQ_L|AQ_L^{\bullet-}$ and $AQ_L^{\bullet-}|AQ_L^{2-}$ occurs at -1.25 and -1.75 V *vs.* $Fc|Fc^+$ respectively, while the oxidations of $AQ_L^{2-}|AQ_L^{\bullet-}$ and

$AQ_L^{\bullet-}|AQ_L$ occur at -1.63 and -1.15 V *vs.* $Fc|Fc^+$. The inset in Figure 7 displays the relationship between the peak current of the first reduction peak, I_{p1}, *vs.* scan rate, v. The linear dependence ($R^2 > 0.99$) of I_{p1} with respect to v, along with the non-linear nature of the I_{p1} *vs.* $\sqrt{v}$ data (not shown) indicates that the AQ_L groups are surface bound[30]. Peak to peak separations for the $AQ_L|AQ_L^{\bullet-}$ and $AQ_L^{\bullet-}|AQ_L^{2-}$ couples at 250 mV s^{-1} were of the order of 100 and 120 mV, respectively. This is related partly to the relatively high iR drop[40] common to ionic liquids, partly due to quasi-reversible electrode kinetics[30] and partly from operating in the region between convergent and planar diffusion limits[41].

Scan rate investigations yielding similar dependencies were also performed on AQ_L-modified electrodes in the ionic liquids $[C_2mim][NTf_2]$ and $[P_{6,6,6,14}][FAP]$. Example CVs recorded in $[C_2mim][NTf_2]$ and $[P_{6,6,6,14}][FAP]$ at 250 mV s^{-1} are shown in Figure 8 and Figure 9, respectively.

Figure 8 demonstrates the two-step reduction of AQ_L to AQ_L^{2-} in $[C_2mim][NTf_2]$ at 250 mV s^{-1}, along with the subsequent two-step oxidation of AQ_L^{2-} to AQ_L. The peaks corresponding to the $AQ_L|AQ_L^{\bullet-}$ and $AQ_L^{\bullet-}|AQ_L^{2-}$ reductions were found to occur at -1.23 and -1.51 V *vs.* $Fc|Fc^+$ respectively, while the subsequent $AQ_L^{2-}|AQ_L^{\bullet-}$ and $AQ_L^{\bullet-}|AQ_L$ oxidations were found to occur at *ca.* -1.37 and -1.10 V *vs.* $Fc|Fc^+$, respectively.

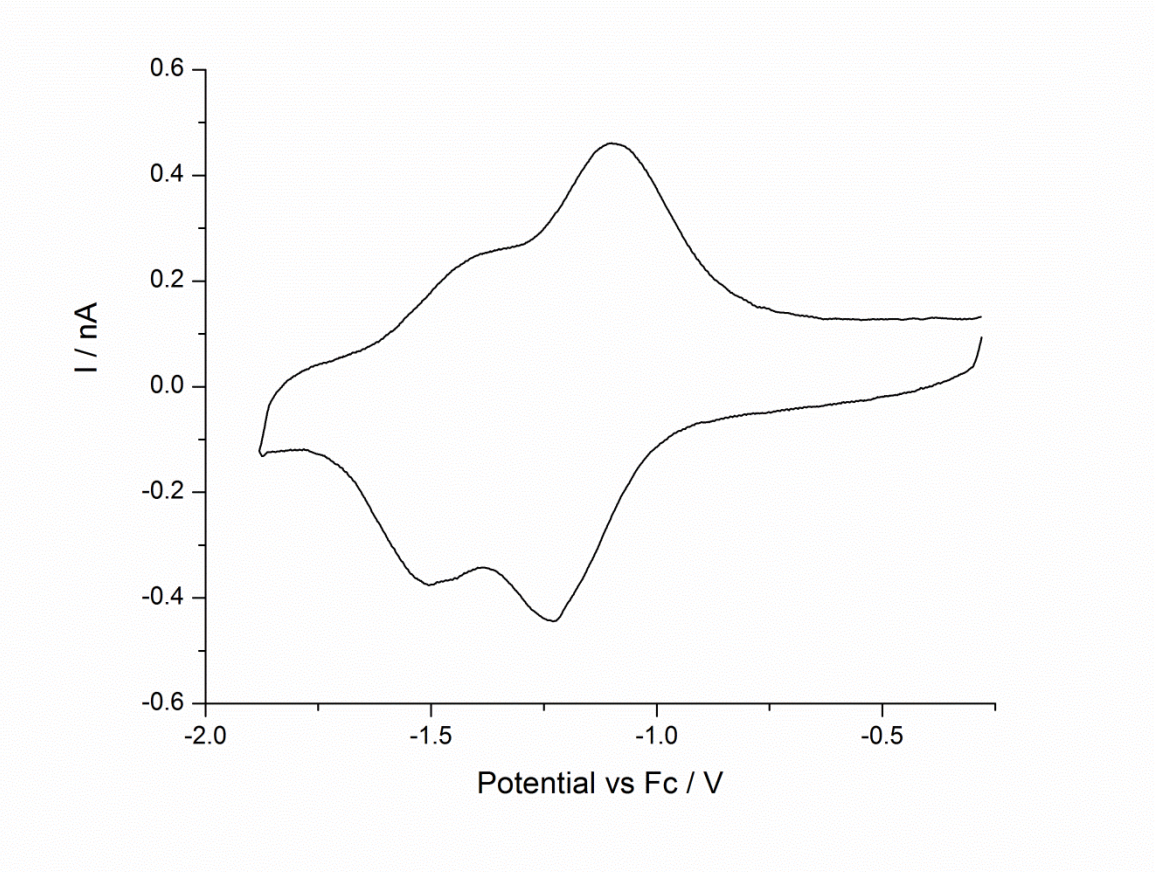


Figure 8 – The reduction of surface-bound AQ_L groups on a glassy carbon microelectrode (r = 7.5μm) in $[C_2mim][NTf_2]$ at 250 mV s^{-1}.

Also apparent from Figure 8 is the ease with which the anion radical is further reduced to the dianion in $[C_2mim][NTf_2]$ when compared to the same reduction in $[C_4mPyrr][NTf_2]$, as evidenced by the closer spacing of the reduction peaks. This is well established in the literature, with the difference in the formal potential of redox couple (4.1) or (4.2) in different RTILs being governed chiefly by the degree of hydrogen-bonding interactions between the quinone and RTIL, particularly for couple (4.2)[17].

Furthermore, a much larger percentage of the anion radicals are reduced in the $[C_2mim][NTf_2]$, as evidenced by the larger I_{p2}/I_{p1} peak ratio, where I_{p1} and I_{p2}

correspond to the peak currents of the $AQ_L|AQ_L^{\bullet-}$ and $AQ_L^{\bullet-}|AQ_L^{2-}$ reductions respectively. For $[C_2mim][NTf_2]$, I_{p2}/I_{p1} was found to be 0.89, while for $[C_4mPyrr][NTf_2]$ I_{p2}/I_{p1} was found to be only 0.54. The explanation for this behaviour is discussed below.

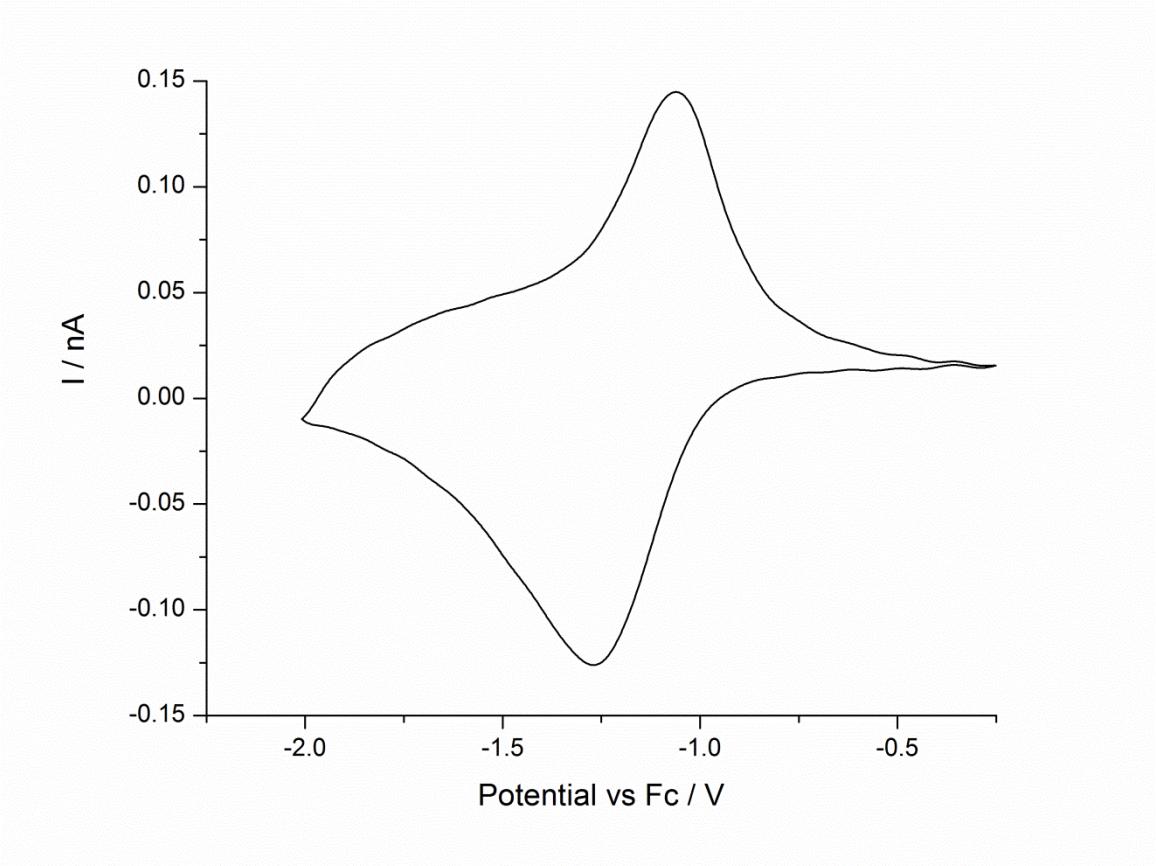


Figure 9 – The reduction of surface-bound AQ_L groups on a glassy carbon microelectrode (r = 7.5μm) in $[P_{6,6,6,14}][FAP]$ at 250 mV s^{-1}.

Figure 9 shows a 250 mV s^{-1} CV of surface-bound AQ_L groups in $[P_{6,6,6,14}][FAP]$, with single reduction and oxidation peaks at -1.27 and -1.06 V *vs.* $Fc|Fc^+$, respectively. This redox wave is assigned purely to the $AQ_L|AQ_L^{\bullet-}$ couple. The possibility that this corresponds to the two-electron reduction of AQ_L to AQ_L^{2-} is ruled out as the reference potential *vs.* $Fc|Fc^+$ matches the AQ_L to $AQ_L^{\bullet-}$

process, and there is no obvious manner in which $[P_{6,6,6,14}][FAP]$ could significantly stabilise the immobilised AQ_L^{2-} species relative to $[C_2mim][NTf_2]$ and $[C_4mPyrr][NTf_2]$. Impurities resulting in proton transfer and a two-electron reduction feature (c.f. behaviour observed in aqueous media[42]) are also ruled out, as quinone/hydroquinone couples are known to exhibit irreversible voltammetry in RTILs[18, 19] and occur at significantly different potentials to those observed for quinones in the absence of protons[17]. Furthermore, the charge under the reduction peak was similar to that observed in $[C_2mim][NTf_2]$ and $[C_4mPyrr][NTf_2]$, rather than a factor of two larger as would be expected for a two electron process occurring in $[P_{6,6,6,14}][FAP]$.

Figure 10 highlights the difference in the ease and extent of the reduction of $AQ_L^{\bullet-}$ to AQ_L^{2-} in each RTIL and also shows a minor difference in the potentials of the AQ_L to $AQ_L^{\bullet-}$ reduction. As all CVs were recorded with a ferrocene internal reference, all potentials were shifted with respect to the $Fc \mid Fc^+$ couple and the currents were normalised for comparison.

Molal volumes of the RTIL cations were calculated via the method of Le Bas, which uses atomic volume contributions (with modifiers) to estimate the volume of complex molecules, from values summarised by Wilke and Chang[43]. The molal volumes for the $[C_2mim]^+$, $[C_4mPyrr]^+$ and $[P_{6,6,6,14}]^+$ cations were calculated to be 149, 211 and 741 $cm^3\ g^{-1}\ mol^{-1}$, respectively.

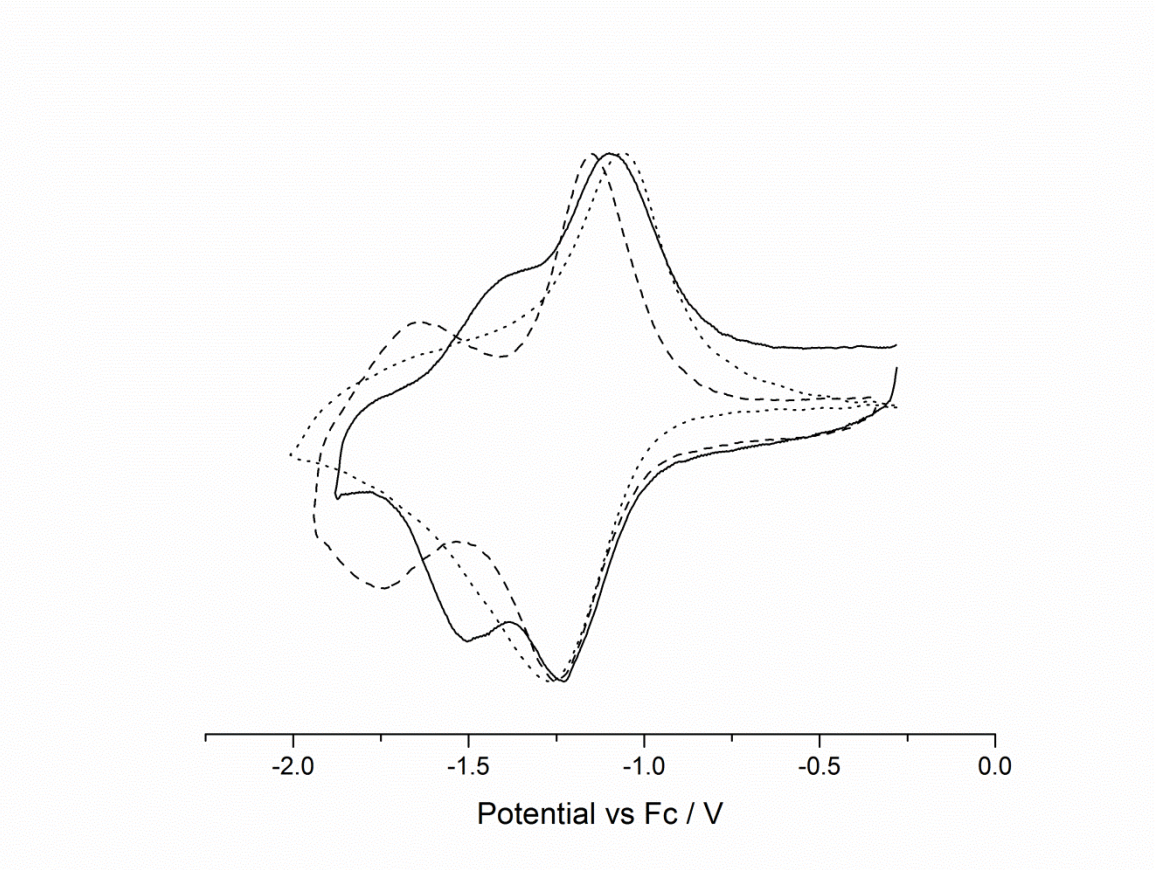


Figure 10 - Overlaid, normalised scans recorded at 250 mV s^{-1} for surface-bound AQ_L groups on a glassy carbon microelectrode (r = 7.5μm) in (—) [C_2mim][NTf_2], (---) [C_4mPyrr][NTf_2] and (···) [$P_{6,6,6,14}$][FAP].

The extent of the $AQ_L^{\bullet-}$ to AQ_L^{2-} reduction in the three RTILs studied, as evidenced by the I_{p2}/I_{p1} peak ratios (see Figure 10), was found to relate to the molal volumes of the RTIL cations. The I_{p2}/I_{p1} ratio was found to decrease from 0.89 in the smaller [C_2mim][NTf_2] to 0.54 in [C_4mPyrr][NTf_2] to 0 in [$P_{6,6,6,14}$][FAP], the largest cation. This behaviour was found to be independent of scan rate and thus cannot be explained by differences in RTIL diffusion. Instead, this behaviour is believed to be the result of steric hindrance at or within the $AQ_L^{\bullet-}$ layer as the RTIL ions maintain electroneutrality in the layer. Cations, compensating for the resulting interfacial charge within the $AQ_L^{\bullet-}$ layer hinder the further reduction to

AQ_L^{2-} because additional cations cannot fit into the immobilised layer. This is particularly relevant when dealing with multilayer films, although a similar process could be envisaged to occur even at monolayer coverages if the AQ_L:cation size disparity is large enough.

Electrodes modified with surface layers of phenyl[27] or anthraquinonyl[28] groups have been observed to alter the electrochemical behaviour of some solution-based redox probes through electrostatic and hydrophilic/hydrophobic interactions[27], which can block the probe's approach to the electrode surface. As a result, electron transfer was found to occur at a greater distance from the electrode surface, with a corresponding decrease in the observed kinetics for most of the probes[27, 28]. Only the behaviour of methyl viologen diiodide was unaltered by the presence of surface-bound phenyl groups, likely due to π-π interactions[27]. Brooksby *et al.* have highlighted that in aqueous systems increasingly compact films of nitrobenzene inhibited proton diffusion, resulting in increasingly cathodic, asymmetric nitrobenzene reduction peaks[10].

In the case of RTILs containing large cations, steric hindrance in the porous layer significantly inhibits the ability of the RTIL to compensate for the build-up of interfacial charge. Thus, bulkier cations such as $[P_{6,6,6,14}]^+$, with an estimated molal volume of 741 cm^3 g^{-1} mol^{-1}, are not able to compensate for the charge of the second reduction to the same extent as a smaller cation, such as $[C_2mim]^+$ with an estimated molal volume of 149 cm^3 g^{-1} mol^{-1}.

4. Influence of Cation Size on Voltammetry in RTILs

If the cation size dependant steric hindrance of charge compensation was the cause of the differing peak ratios, one might expect that a mixture of two RTILs would assume behaviour intermediate to that of the two constituent liquids. Indeed, Figure 11 highlights the large change in voltammetry that even a relatively low (*ca.* 0.8 M, 20.5% V/V) volume of $[C_2mim][NTf_2]$ (smaller cation) added to $[C_4mPyrr][NTf_2]$ (larger cation) can have on both the potential and the extent of the $AQ_L^{\bullet-}$ to AQ_L^{2-} reduction.

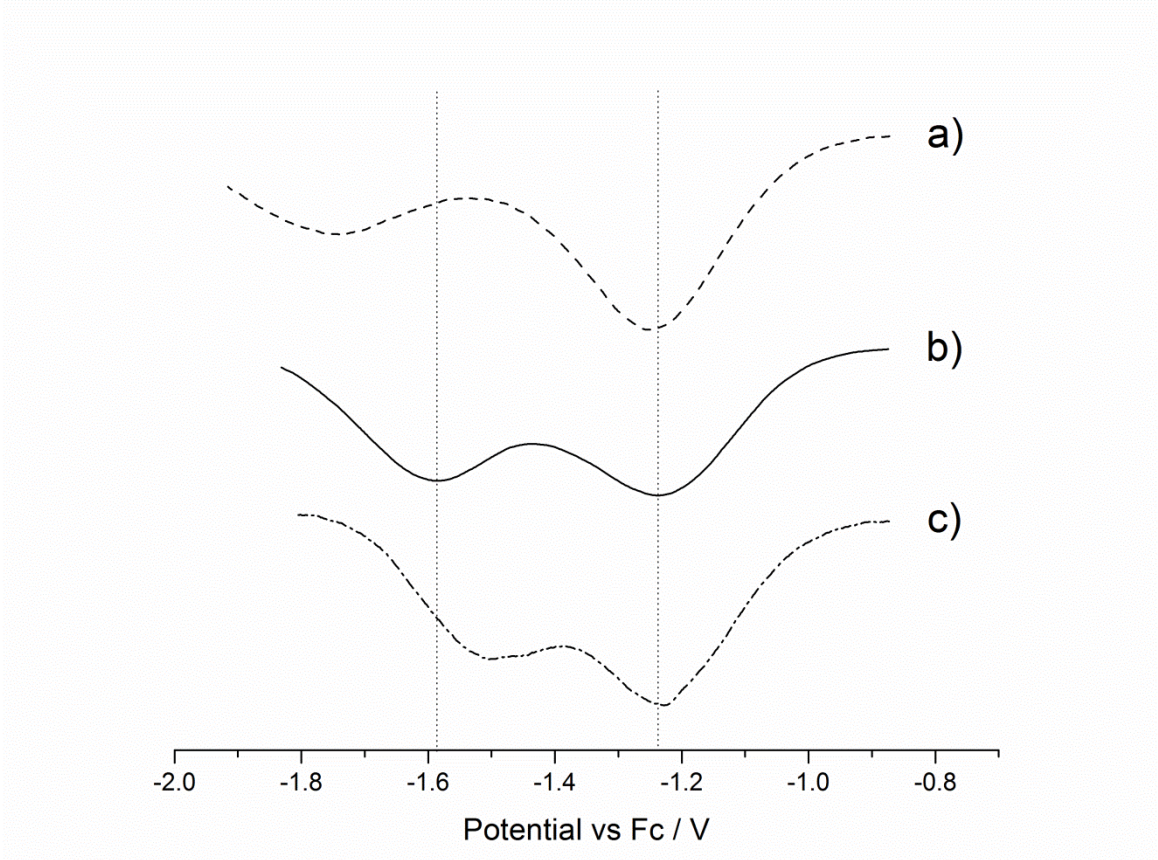


Figure 11 - 250 mV s^{-1} cyclic voltammograms recorded for surface-bound AQ_L groups on a glassy carbon microelectrode (r = 7.5μm) in (a) $[C_4mPyrr][NTf_2]$, (b) $[C_4mPyrr][NTf_2]$ containing 0.8 M $[C_2mim][NTf_2]$ and (c) $[C_2mim][NTf_2]$.

Figure 11 also shows a minor change in the potential of the AQ_L to $AQ_L^{\bullet-}$ reduction. The change in reduction potentials was explained above in terms of the degree of hydrogen-bonding interactions between the AQ_L groups and the RTIL, where couple (4.2) is affected to a much larger degree than couple (4.1)[17].

4.4 Conclusions

It has thus been demonstrated in this chapter that the electroactivity of anthraquinonyl films in RTILs is strongly correlated with the size of the RTIL cation, such that the $AQ_L^{\bullet-}|AQ_L^{2-}$ redox process becomes increasingly suppressed with increasing cation size. Steric hindrance of additional cations prevents charge compensation and hence inhibits the electroactivity of the film. The choice of RTIL is therefore critical to the response of immobilised electroactive layers, such as those which have been used in electroanalytical sensing[44] or electrocatalysis[45, 46]. This may also have implications for the electroactivity of species inside porous films when RTILs are used as the electrolyte. The selection of RTIL for a given electrochemical application thus depends on a combination of factors, including the size of the ionic components, potential window, conductivity, chemical stability, cost as well as mass transport (viscosity) considerations. After careful consideration of all of these factors, the following chapter presents an investigation of oxygen reduction at glassy carbon and boron-doped diamond electrodes, utilising the $[C_2mim][NTf_2]$ ionic liquid.

References

1. S. Ernst, L. Aldous and R. G. Compton, *Chemical Physics Letters*, 2011, 511, 461-465.
2. M. Delamar, R. Hitmi, J. Pinson and J. M. Savéant, *Journal of the American Chemical Society*, 1992, 114, 5883-5884.
3. P. Allongue, M. Delamar, B. Desbat, O. Fagebaume, R. Hitmi, J. Pinson and J. M. Savéant, *Journal of the American Chemical Society*, 1997, 119, 201-207.
4. L. Santos, J. Ghilane, P. Martin, P. C. Lacaze, H. Randriamahazaka and J. C. Lacroix, *Journal of the American Chemical Society*, 2010, 132, 1690-1698.
5. A. J. Downard, *Electroanalysis*, 2000, 12, 1085-1096.
6. M. Pandurangappa, N. S. Lawrence and R. G. Compton, *Analyst*, 2002, 127, 1568-1571.
7. K. G. Ray Iii and R. L. McCreery, *Journal of Electroanalytical Chemistry*, 1999, 469, 150-158.
8. F. Anariba, S. H. DuVall and R. L. McCreery, *Analytical Chemistry*, 2003, 75, 3837-3844.
9. J. K. Kariuki and M. T. McDermott, *Langmuir*, 2001, 17, 5947-5951.
10. P. A. Brooksby and A. J. Downard, *Journal of Physical Chemistry B*, 2005, 109, 8791-8798.
11. M. Kullapere, F. Mirkhalaf and K. Tammeveski, *Electrochimica Acta*, 2010, 56, 166-173.
12. J. Ghilane, P. Martin, O. Fontaine, J.-C. Lacroix and H. Randriamahazaka, *Electrochemistry Communications*, 2008, 10, 1060-1063.
13. O. Fontaine, J. Ghilane, P. Martin, J. C. Lacroix and H. Randriamahazaka, *Langmuir*, 2010, 26, 18542-18549.
14. G. G. Wildgoose, M. Pandurangappa, N. S. Lawrence, L. Jiang, T. G. J. Jones and R. G. Compton, *Talanta*, 2003, 60, 887-893.
15. H. C. Leventis, I. Streeter, G. G. Wildgoose, N. S. Lawrence, L. Jiang, T. G. J. Jones and R. G. Compton, *Talanta*, 2004, 63, 1039-1051.

16. B. Murphy, P. Goodrich, C. Hardacre and M. Oelgemöller, *Green Chemistry*, 2009, 11, 1867-1870.
17. C. Costentin, *Chemical Reviews*, 2008, 108, 2145-2179.
18. Y. Wang, S. R. Belding, E. I. Rogers and R. G. Compton, *Journal of Electroanalytical Chemistry*, 2011, 650, 196-204.
19. Y. Wang, E. I. Rogers, S. R. Belding and R. G. Compton, *Journal of Electroanalytical Chemistry*, 2010, 648, 134-142.
20. E. O. Barnes, A. M. O'Mahony, L. Aldous, C. Hardacre and R. G. Compton, *Journal of Electroanalytical Chemistry*, 2010, 646, 11-17.
21. M. T. Carter and R. A. Osteryoung, *Journal of the Electrochemical Society*, 1992, 139, 1795-1802.
22. V. A. Nikitina, R. R. Nazmutdinov and G. A. Tsirlina, *Journal of Physical Chemistry B*, 2011, 115, 668-677.
23. WO 2006003395 (A2), Jan 12, 2006.
24. C. Batchelor-McAuley, B. R. Kozub, D. Menshykau and R. G. Compton, *The Journal of Physical Chemistry C*, 2010, 115, 714-718.
25. J. Pinson and F. Podvorica, *Chemical Society Reviews*, 2005, 34, 429-439.
26. S. H. DuVall and R. L. McCreery, *Journal of the American Chemical Society*, 2000, 122, 6759-6764.
27. A. J. Downard and M. J. Prince, *Langmuir*, 2001, 17, 5581-5586.
28. R. Reilson, M. Kullapere and K. Tammeveski, *Electroanalysis*, 2010, 22, 513-518.
29. M. Janin, J. Ghilane, H. Randriamahazaka and J.-C. Lacroix, *Electrochemistry Communications*, 2009, 11, 647-650.
30. R. G. Compton and C. E. Banks, *Understanding voltammetry, 2nd ed.*, World Scientific, Singapore ; London, 2011.
31. J. K. Kariuki and M. T. McDermott, *Langmuir*, 1999, 15, 6534-6540.
32. M. S. Strano, C. A. Dyke, M. L. Usrey, P. W. Barone, M. J. Allen, H. Shan, C. Kittrell, R. H. Hauge, J. M. Tour and R. E. Smalley, *Science*, 2003, 301, 1519-1522.
33. J.-M. Seinberg, M. Kullapere, U. Mäeorg, F. C. Maschion, G. Maia, D. J. Schiffrin and K. Tammeveski, *Journal of Electroanalytical Chemistry*, 2008, 624, 151-160.

34. A. Prakash, *Acta Crystallographica*, 1967, 22, 439-440.
35. A. Bondi, *J. Phys. Chem.*, 1964, 68, 441-451.
36. E. Laviron, *Electroanal. Chem.*, 1982, 12, 53-157.
37. M. J. Honeychurch and G. A. Rechnitz, *Electroanalysis*, 1998, 10, 285-293.
38. E. I. Rogers, D. S. Silvester, D. L. Poole, L. Aldous, C. Hardacre and R. G. Compton, *J Phys Chem C*, 2008, 112, 2729-2735.
39. R. Wibowo, L. Aldous, E. I. Rogers, S. E. W. Jones and R. G. Compton, *J Phys Chem C*, 2010, 114, 3618-3626.
40. M. I. Montenegro, *Res. Chem. Kinet.*, 1994, 2, 1-80.
41. A. S. Barnes, E. I. Rogers, I. Streeter, L. Aldous, C. Hardacre and R. G. Compton, *The Journal of Physical Chemistry B*, 2008, 112, 7560-7565.
42. C. Batchelor-McAuley, Q. Li, S. M. Dapin and R. G. Compton, *The Journal of Physical Chemistry B*, 2010, 114, 4094-4100.
43. C. R. Wilke and P. Chang, *AIChE Journal*, 1955, 1, 264-270.
44. T. Ramakrishnappa, M. Pandurangappa and D. H. Nagaraju, *Sensors and Actuators, B: Chemical*, 2011, DOI: 10.1016/j.snb.2011.1001.1020.
45. Q. Li, C. Batchelor-McAuley, N. S. Lawrence, R. S. Hartshorne and R. G. Compton, *ChemPhysChem*, 2011, 12, 1255-1257.
46. A. Sarapuu, K. Helstein, K. Vaik, D. J. Schiffrin and K. Tammeveski, *Electrochimica Acta*, 2010, 55, 6376-6382.

5. Oxygen Reduction in RTILs at Different Electrodes

This chapter describes the reduction of oxygen (O_2) on boron-doped diamond (BDD) and glassy carbon (GC) electrodes in the 1-ethyl-3-methylimidazolium bis(trifluoromethylsulfonyl)imide, $[C_2mim][NTf_2]$, ionic liquid. O_2 reduction at both electrodes is found to involve the one electron reduction of oxygen to superoxide ($O_2^{\bullet -}$). The formation of superoxide is verified by repeating the oxygen reduction on BDD in the presence of benzoic acid, resulting in a shift from the one electron reduction observed in the absence of benzoic acid to a two electron reduction yielding the hydroperoxyl anion. The reduction of O_2 is found to be electrochemically quasi-reversible on GC and irreversible on BDD. The significantly slower kinetics observed on the BDD electrode are likely due to the lower electronic density of states in BDD. The work presented in this chapter has been published in the *Journal of Electroanalytical Chemistry*[1].

5.1 Introduction

The electrochemical reduction of oxygen has been variously studied in aqueous[2-4], non-aqueous[5, 6] and room-temperature ionic liquid (RTIL)[7-13] media. The interest in the oxygen reduction reaction stems primarily from the research into fuel cells, metal-air batteries, electrocatalysis and the electrosynthesis of reactive oxygen species such as superoxide ($O_2^{\bullet -}$)[14-16]. In addition, the oxygen reduction reaction in RTIL media is of interest with regards to gas sensing[8-12].

5. Oxygen reduction in RTILs at Different Electrodes

The superoxide anion has previously been shown to exhibit chemically reversible voltammetry in a range of dry aprotic solvents[5, 6] and RTILs[8, 12, 13]. RTILs are of particular interest as a solvent for the oxygen reduction reaction because of their low volatility, large electrochemical windows and ability to withstand high temperatures and pressures. RTILs are also able to stabilise reaction compounds and intermediates that cannot be easily investigated using molecular solvents[17], as well as exhibit considerable influence on the reactivity of anion radicals[18].

In aprotic media, the reduction of oxygen to the superoxide anion has been shown to proceed *via* a single, reversible 1e$^-$ step according to (7.1)[5];

$$O_2 + e^- \rightleftharpoons O_2^{\bullet -} \tag{7.1}$$

Upon addition of weak proton donors such as water or other weak acids to aprotic solvents, the superoxide formed in (7.1) can become protonated *via* (7.2);

$$O_2^{\bullet -} + HA \rightleftharpoons HO_2^{\bullet} + A^- \tag{7.2}$$

This protonated species can then undergo disproportionation to form the peroxide species. While the exact mechanism of this step has been disputed[19, 20], the overall observed reaction stoichiometry (at long timescales or for rapid disproportionation) is given by (7.3);

$$O_2 + 2e^- + H^+ \longrightarrow HO_2^- \tag{7.3}$$

The HO_2^- species may then undergo further protonation, depending on the concentration and acidity of the proton donor, *via* (7.4);

$$HO_2^- + HA \rightleftharpoons H_2O_2 + A^- \qquad (7.4)$$

A concerted proton and electron transfer (CPET) has also been reported for the reduction of $O_2^{\bullet -}$ to $HO_2^{\bullet -}$ in acetonitrile in the presence of weak acids such as water[21], although only at high overpotentials.

Boron-doped diamond (BDD) electrodes have found use in the oxidation of pollutants in water treatment applications as well as electroanalytical and bioelectroanalytical sensing, synthesis, catalysis and lithium batteries[14, 22]. BDD electrodes are well suited to electroanalytical applications, in particular due to their low background current, wide potential window and high electrochemical stability[14, 23].

BDD electrodes have been shown to markedly slow the kinetics of the electrochemical reduction of oxygen in *aqueous* media when compared to other electrode materials[3, 4]. Similar observations have also been reported for the electrochemical oxidation of ferrocene[24] and reduction of 1,4-benzoquinone[25] in non-aqueous media. However, to date, there have been no investigations on the electrochemical reduction of oxygen at BDD electrodes in RTILs, despite the increasing importance of these electrodes to a wide variety of applications[14].

In the following, the electrochemical reduction of oxygen was investigated in the ionic liquid 1-ethyl-3-methylimidazolium bis(trifluoromethylsulfonyl)imide

([C_2mim][NTf_2]) on both boron-doped diamond and glassy carbon electrodes. Thus, a comparative study of electrode kinetics at GC and BDD surfaces in ionic liquid media is reported for the fundamental oxygen reduction reaction.

5.2 Experimental

All electrochemical measurements were performed in a thermostated Faraday cage (25 ± 1 °C) using a μAutolab Type II computer-controlled potentiostat (Ecochemie), set to a potential step of 2mV and α value of 0.3. All measurements were recorded using a standard three electrode configuration employing a coiled platinum wire (0.5 mm diameter, 99.99% pure, Goodfellow) counter electrode and a silver wire (0.5 mm diameter, 99.99% pure, Goodfellow) quasi-reference electrode. Boron-doped diamond (r = 1.5 mm, ~10^{20} cm^{-3} boron, Windsor Scientific, D-191-SA) and glassy carbon (r = 1.5 mm, BASi) macrodisk electrodes were used as working electrodes. Prior to use, the working electrodes were polished using 3 and 1 μm spray-diamond lapping compounds (Kehmet) on hard lapping pads (Kehmet). The polished electrodes were then placed in deionised water (resistivity 18.2 MΩ cm at 25 °C, Millipore water systems) in an ultrasonic bath for approximately three minutes to remove any adsorbed material. The electrodes were then rinsed with MeCN and dried using compressed air. Before use, the platinum wire was cleaned in a hot Bunsen flame, while the silver wire was lightly polished using P1000 silicon carbide paper (Flexovit), both wires were then rinsed with MeCN und dried under a compressed air flow.

5. Oxygen reduction in RTILs at Different Electrodes

The experiment was prepared by adding 400 μL of [C_2mim][NTf2] into a 5 mL sample flask and inserting the working, counter and reference electrodes along with two glass Pasteur pipettes, one immersed in the ionic liquid and the other suspended above it. A 20% O_2:N_2 (40:160 cm^3 min^{-1} (ATP)) mixture was prepared *via* a gas mixer fabricated in-house from two needle valve assemblies (Platon). This mixture was then passed through a column of molecular sieves to remove any residual water prior to introduction to the system. The gaseous mixture was bubbled through the RTIL for at least 1 hour before measurements commenced, at which point the gas was allowed to flow over the top of the liquid *via* the second Pasteur pipette.

5.3 Results and Discussion

A 400 μL sample of [C_2mim][NTf_2] was saturated with oxygen by passing 40:160 cm^3 min^{-1} O_2:N_2 through the liquid for at least 1 hour. Bubbling was ceased while CVs were recorded, although a positive pressure of O_2:N_2 was maintained.

Figure 12 shows cyclic voltammograms (CVs) illustrating the voltammetry of O_2 on glassy carbon (GC) in [C_2mim][NTf_2] and how this voltammetry changes with varying scan rate in the 0.01 to 1.00 V s^{-1} range. This has been reported previously[26] but serves as a comparison for later voltammetry at the boron-doped diamond (BDD) electrode. Figure 12 shows the peaks (as measured without background correction) representing the reduction of O_2 to $O_2^{\bullet-}$ (A_{GC}) and the subsequent reoxidation of $O_2^{\bullet-}$ to O_2 (B_{GC})[26]. Very minor features corresponding to

the oxidation of $HO_2^{\bullet}$ (C_{GC}) and HO_2^- (D_{GC}) can also be observed and may stem from reactions after the deprotonation of trace amounts of water[26, 27]. With the exception of peak D_{GC}, all of the peaks increase with increasing scan rate.

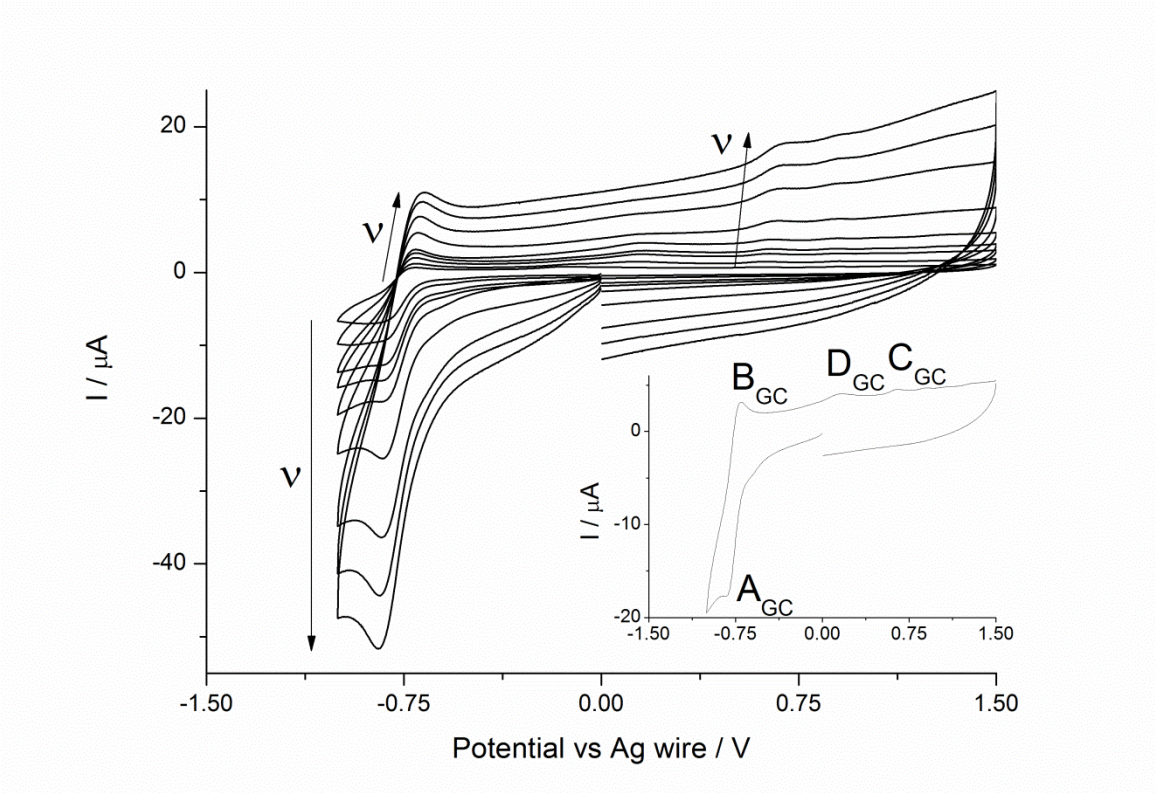


Figure 12 – Scan rate comparison for the reduction of O_2 (20:80 v/v O_2:N_2) in [C_2mim][NTf_2] at a GC electrode (r = 1.5 mm), showing scan rates of 10, 25, 50, 75, 100, 250, 500, 750 and 1000 mV s^{-1}. The inset displays a CV recorded at 100 mV s^{-1}, highlighting the four distinct features.

The HO_2^- species is likely formed[27] via the proton-induced disproportionation of $O_2^{\bullet-}$, as observed in aprotic media[19, 20]. Due to the slow nature of this process, caused by trace water, this peak could only be observed at slow scan rates. A Randles-Ševčík plot (not shown) of the O_2 reduction peak currents *vs.* the square root of the scan rate, ν, yields an approximately linear ($r^2 = 0.980$) relationship. Furthermore, the peak-to-peak separation, ΔE_{pp}, increases with v, showing that

the reduction of O_2 on GC is quasi-reversible[28]. At 100 mV s^{-1}, the reduction of O_2 to $O_2^{\bullet-}$ was found to occur at -0.83 V *vs.* the silver wire quasi-reference, while the oxidation peak occurs at -0.71 V. This then yields a ΔE_{pp} of 120 mV, typical for a quasi-reversible couple. Furthermore, this data is comparable to that previously reported for O_2 reduction in 1-ethyl-3-methylimidazolium tetrafluoroborate, $[C_2mim][BF_4]$, which was also found to be quasi-reversible[29].

The glassy carbon working electrode was then replaced with a BDD working electrode (r = 1.5 mm), while the system remained otherwise unchanged, allowing for a direct comparison between O_2 reduction on glassy carbon and on BDD.

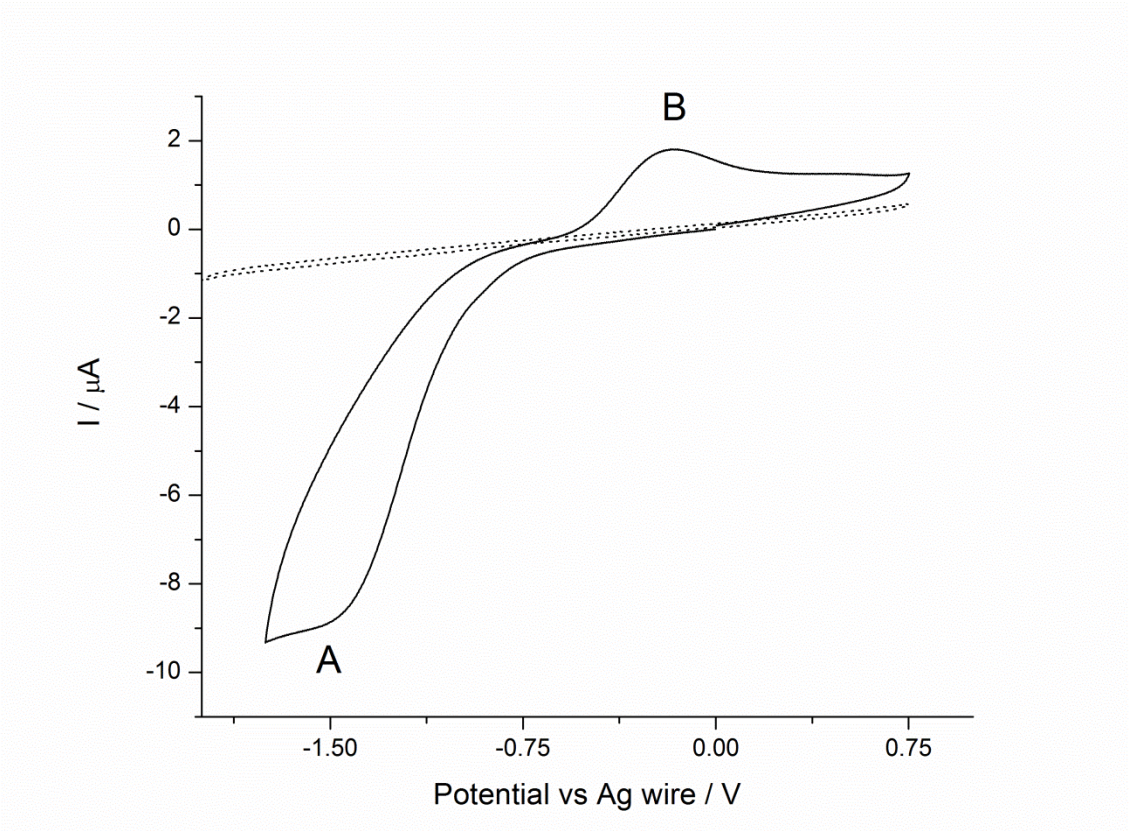


Figure 13 - 100 mV s^{-1} cyclic voltammograms of $[C_2mim][NTf_2]$ under N_2 (· · ·) and 20:80 v/v O_2:N_2 (—), showing O_2 reduction at the BDD electrode (r = 1.5 mm), with potentials quoted *vs.* an Ag wire quasi-reference.

5. Oxygen reduction in RTILs at Different Electrodes

Figure 13 shows a CV of the reduction of O_2 in $[C_2mim][NTf_2]$ at a BDD electrode using a scan rate of 100 mV/s. Figure 13 also shows the voltammetry in the absence of oxygen, under a nitrogen atmosphere. Immediately apparent from the CV of the oxygenated sample are two features; A, which corresponds to the reduction of O_2 to $O_2^{\bullet-}$ and B, which represents the subsequent oxidation of $O_2^{\bullet-}$ to O_2 on the reverse scan. The reduction peak occurs at *ca.* -1.57 V *vs.* the silver wire quasi-reference, while the oxidation peak occurs at -0.18 V, yielding a ΔE_{pp} of *ca.* 1.39 V. This is clearly irreversible voltammetry and exhibits much slower electrode kinetics than for the same system at the GC electrode.

Figure 14 shows the effects of varying the scan rate (v) on the voltammetry of the oxygen reduction at the BDD electrode. The figure shows that an increase in scan rate leads to both an increase in the reductive peak current, A, and an increase in the subsequent oxidative peak current, B. Also visible is an increase in peak-to-peak separation with increasing scan rate, indicating that the voltammetry is irreversible. A Randles-Ševčík plot of reductive peak current *vs.* the square root of scan rate (not shown) yields a linear ($r^2 = 0.985$) relationship, indicating a diffusional system[28].

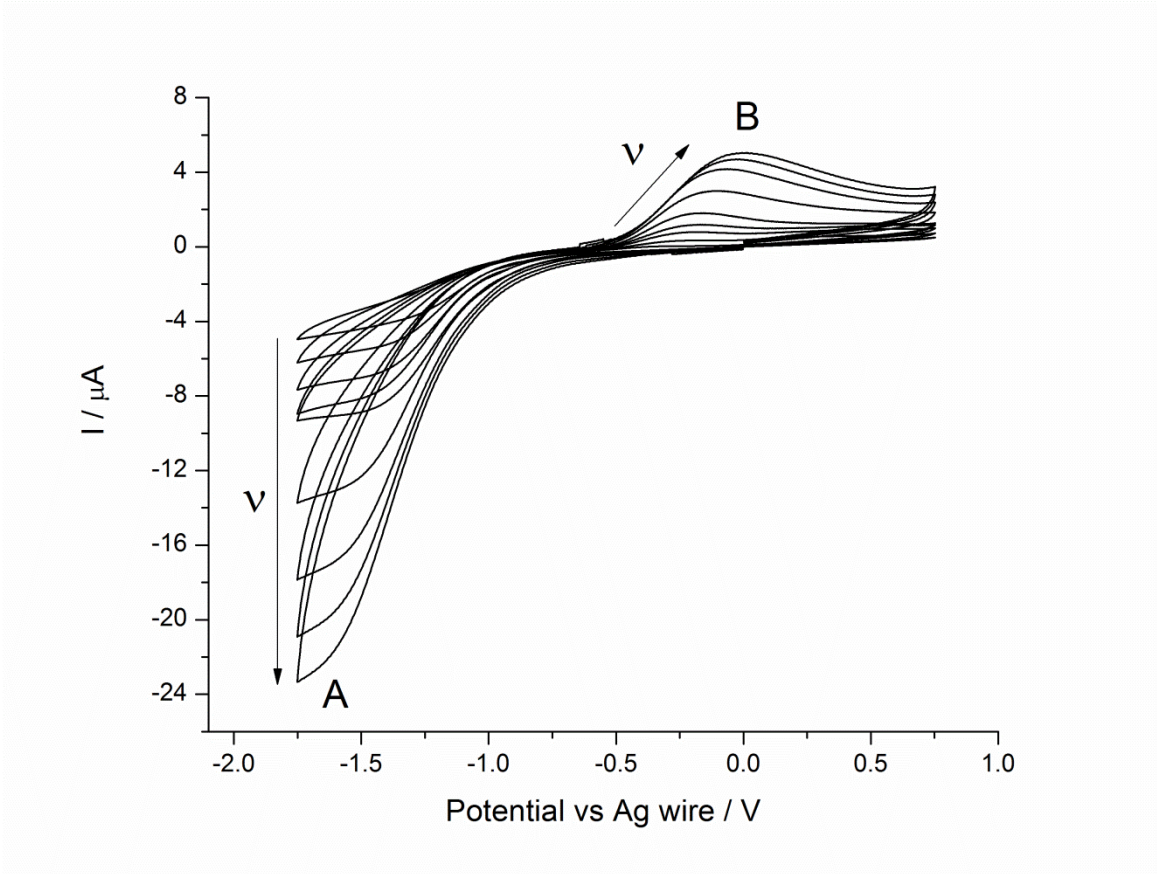


Figure 14 - Cyclic voltammograms investigating the behaviour of the reduction of O_2 (20:80 v/v O_2:N_2) in [C_2mim][NTf_2] at a BDD electrode (r = 1.5 mm), with respect to scan rate (ν). The scan rates studied were 10, 25, 50, 75, 100, 250, 500, 750 and 1000 mV/s.

In order to verify that the reduction feature (A) corresponded to the formation of superoxide and not peroxide, during the voltammetry of O_2 in [C_2mim][NTf_2] on BDD, the solution was saturated with benzoic acid (75 ± 2 mM following the work of He *et al.*[30]) and the scan rate study was repeated. Figure 15 shows the data from this scan rate investigation, with the currents divided by the square root of the scan rate in order to normalise the data for a diffusional system. This data shows a distinct decrease in the backpeak corresponding to the oxidation of $O_2^{\bullet-}$ to O_2, as well as a change in three additional peaks; C, D and E. Peaks C and D correspond to the oxidation of HO_2^- and $HO_2^\bullet$ respectively. Peak E was

observed on GC and BDD in the presence and absence of benzoic acid, only after the reduction of oxygen to either superoxide or peroxide. Peak E was generally broad and ill-formed and was found to decrease upon addition of benzoic acid. Peak E was thus tentatively assigned to the oxidation of the imidazolium cation formed by the deprotonation of the C_2 carbon by either the superoxide or the peroxide anions. Suarez et al. have previously observed the electrochemical oxidation of the imidazolium carbene species[31]. No reduction peaks were observed for the benzoic acid at the potentials studied.

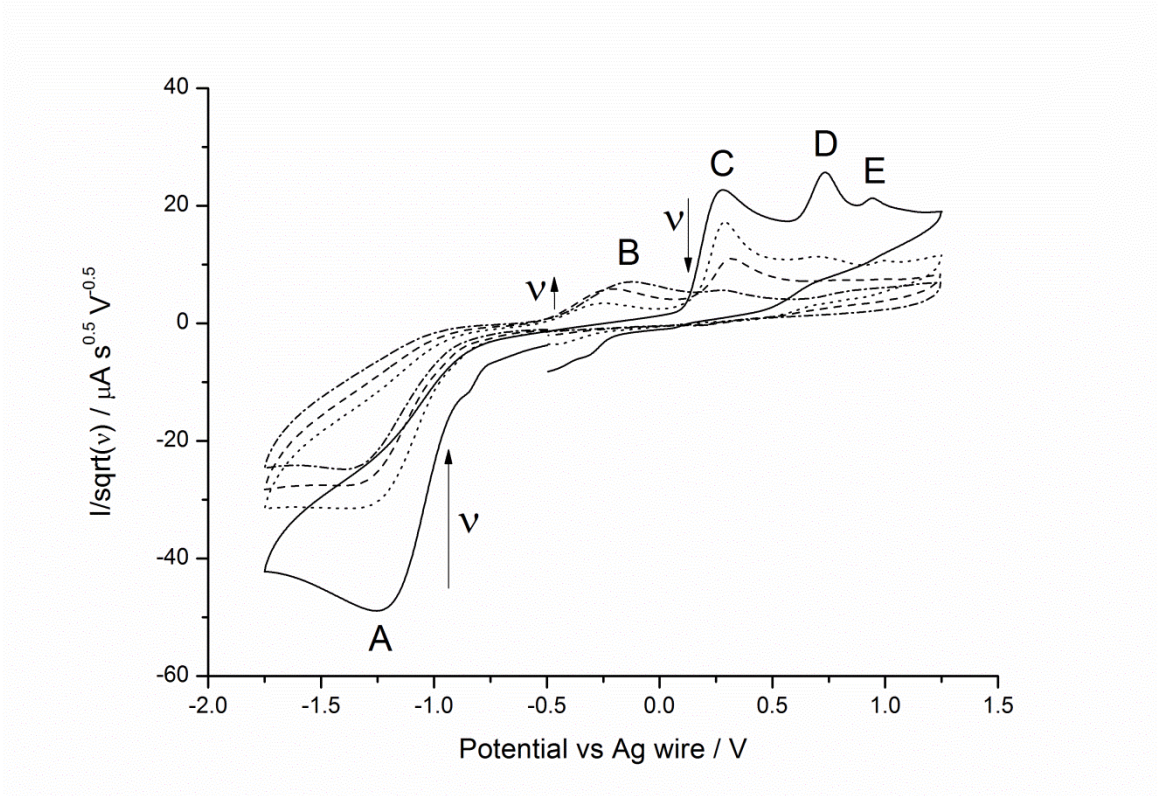


Figure 15 - Cyclic voltammograms of the reduction and subsequent re-oxidation of O_2 (20:80 v/v O_2:N_2), in [C_2mim][NTf_2] saturated with benzoic acid at a BDD electrode (r = 1.5 mm), at scan rates of 10 mV s^{-1} (——), 100 mV s^{-1} (· · ·), 250 mV s^{-1} (– – –) and 1000 mV s^{-1} (· – ·).

5. Oxygen reduction in RTILs at Different Electrodes

The increase in peak A and decrease in peak B with decreasing ν, shown in Figure 15, is the result of the reaction between electrogenerated $O_2^{\bullet-}$ and H^+ from the benzoic acid forming $HO_2^{\bullet}$, which is then further reduced to HO_2^-, *cf.* the two-electron reduction of oxygen in aqueous systems[3] and aprotic systems in the presence of strong acids[19, 20]. The time available for this chemical reaction is obviously much larger at the lower scan rates and is hence manifested as an increase in A. Upon the reverse sweep, B decreases while C and D increase with decreasing ν as at low scan rates all of the $O_2^{\bullet-}$ is converted to HO_2^-, while at faster scan rates less $O_2^{\bullet-}$ is converted. The reduction process is therefore a *ca.* $1e^-$ 'E' process (to the superoxide species) at fast scan rates, changing to a $2e^-$ 'ECCE' process at slow scan rates.

Figure 16 shows the voltammetry of the reduction and subsequent oxidation of O_2 in $[C_2mim][NTf_2]$ at both BDD and GC electrodes ($r_{BDD} = r_{GC} = 1.5$ mm). Apparent from Figure 16 is that the reduction of O_2 on BDD is much more irreversible than that on GC. The decreased kinetics of oxygen reduction on BDD has previously allowed for the electrochemical investigation of species whose Faradaic features would normally be obscured by the interference of atmospheric oxygen[32]. Also of note is the significantly smaller double-layer capacitance observed for the BDD electrode in the ionic liquid, as reported previously for BDD[14].

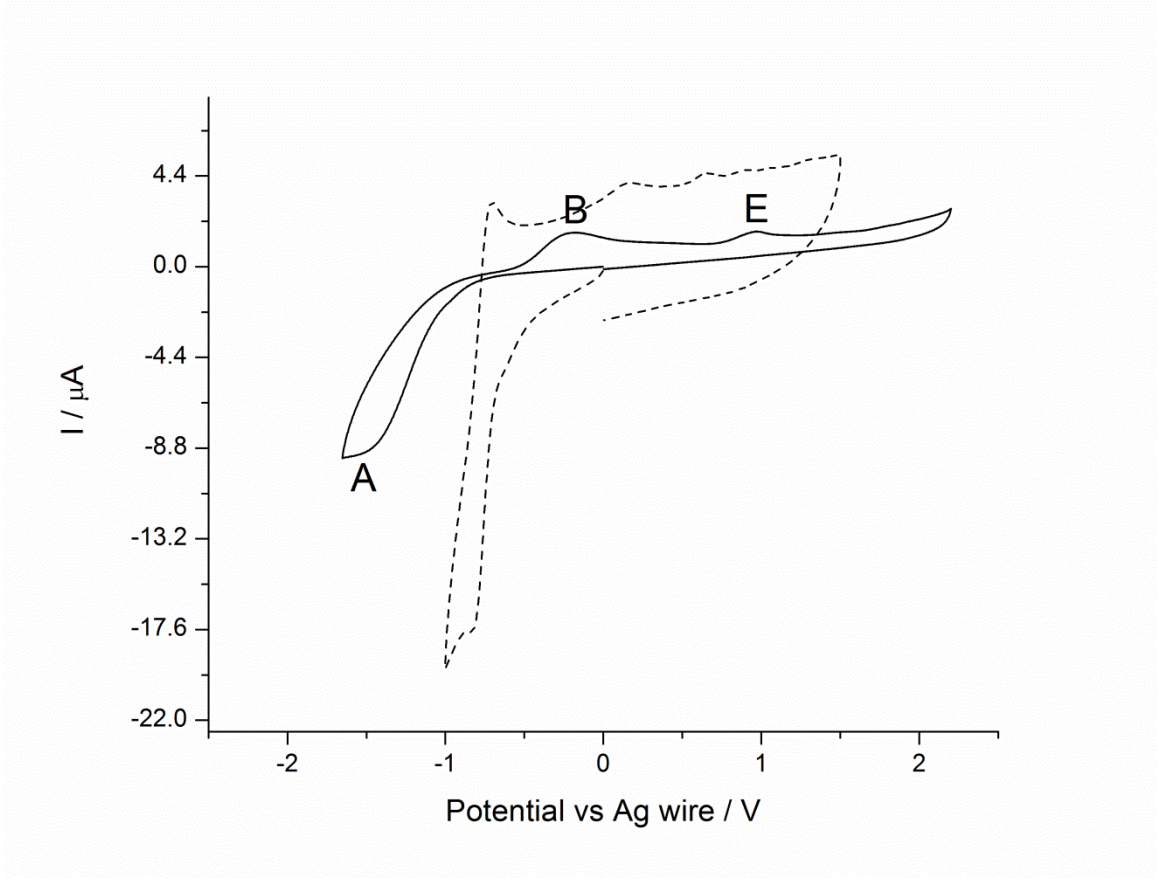


Figure 16 - Overlaid 100 mV s^{-1} cyclic voltammetry for the reduction of O_2 (20:80 v/v O_2:N_2) in [C_2mim][NTf_2] at BDD (r = 1.5 mm, ——) and GC (r = 1.5 mm, – – –) electrodes.

It has been suggested by several authors that the decreased electrode kinetics, as well as the decreasing double-layer capacitance, of highly ordered carbon samples (in particular HOPG), in comparison to disordered sp^2 carbon compounds such as glassy carbon, reflects differences in the density of electronic states (DOS) for the different materials[33-35]. Similar arguments have been extended towards BDD[3, 36], although this case is more complex. Undoped diamond has a large band-gap between its valence and conduction bands and is thus practically an insulator. Doping with boron introduces charge acceptors, or hole dopants, resulting in a semiconducting diamond electrode. These hole dopants,

once incorporated into the diamond lattice, lead to electronic states within the diamond band-gap, increasing the DOS in this region[35, 36]. The number of these "midgap" states is further increased by crystal defects in the film[35, 36]. Hydrogen atoms incorporated into the diamond films during deposition also act as dopants, further increasing the range of midgap states[35, 36]. Furthermore, sp^2 carbon impurities residing in the diamond grain boundaries have also been shown to markedly impact on the reaction kinetics, at least in aqueous systems[37]. The density of states for BDD samples is thus dependant on all of these factors, as highlighted in an excellent discussion by Granger et al[36]. Nonetheless, for practical purposes, the lower DOS for BDD, as compared to that for GC[38], significantly slows down the electrode kinetics of O_2 reduction, leading to the voltammetry observed in the present work. It should be noted that polycrystalline BDD electrodes have been shown to possess microscopic electrical heterogeneity, with conductivity and electron transfer rates varying between individual crystallites and at grain boundaries[39, 40]. These variations were found to be linked to differences in the boron doping level of the individual crystallite phases which make up the polycrystalline BDD electrode. However, these variations are usually averaged out over the surface of the electrode when dealing with macroelectrodes as the individual crystallites typically have dimensions of a few micrometers.

Tafel plots were constructed from 10 mV s^{-1} reduction data on both BDD and GC. Figure 17 shows these Tafel plots for the reduction of O_2 to $O_2^{\bullet -}$ on BDD (a)

and GC (b). The electron transfer coefficients for oxygen reduction can then be extracted from the gradients of the Tafel plots via (7.5)[28];

$$\frac{\partial \ln(I)}{\partial E} = \frac{-(n' + \alpha_{n'}) \cdot F}{R \cdot T} \tag{7.5}$$

where, I is the current, E is the potential, n' the number of electrons passed before the rate limiting step, $\alpha_{n'}$ the electron transfer coefficient of the rate limiting step, F is Faraday's constant, R the universal gas constant and T the temperature.

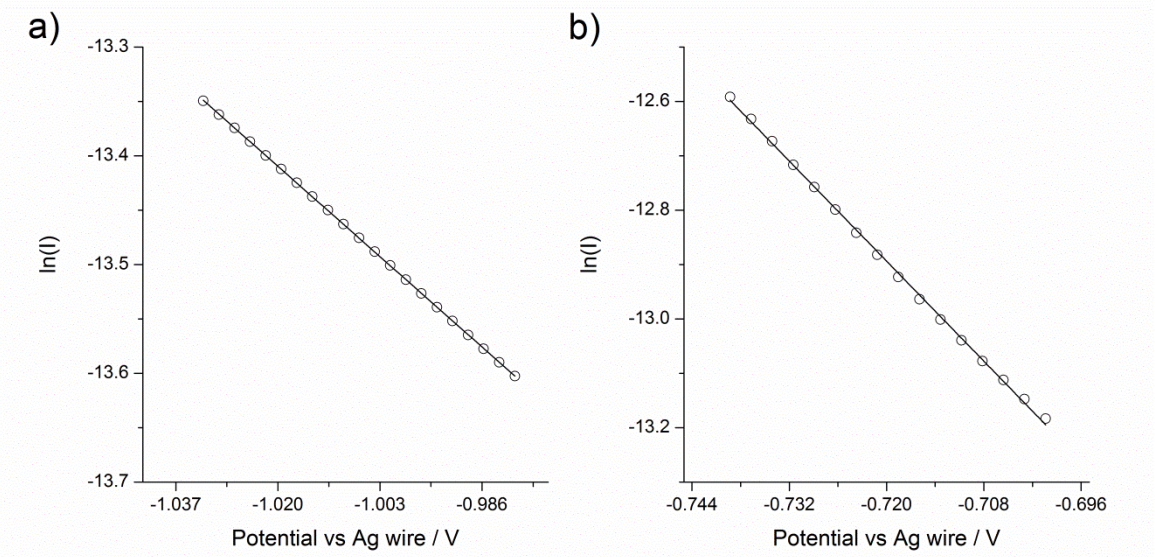


Figure 17 - Tafel plots created using data from 10 mV s^{-1} CVs of the reduction of O_2 to superoxide in [C_2mim][NTf_2] at a) a BDD electrode (r = 1.5 mm) and b) a GC electrode (r = 1.5 mm).

The transfer coefficients for the reduction of oxygen to superoxide (n' = 0) in [C_2mim][NTf_2] on BDD and GC were thus found to be 0.13 and 0.39, respectively. These values for the electron transfer coefficient for O_2 are presented, along with other values from the literature, in Table 5.

Table 5 - Tabulated α values for a range of systems involving different carbon electrodes.

Electrode	Solution	α
GC	0.1M KOH[a]	0.17[3]
GC	0.1M $[N_{2222}][ClO_4]$ in MeCN	0.31[13]
GC	$[C_2mim][NTf_2]$	0.39[*]
GC	$[C_4mim][BF_4]$	0.39[29]
GC	$[C_3mim][BF_4]$	0.42[29]
GC	$[C_4mim][PF_6]$	0.42[13]
GC	$[C_2mim][BF_4]$	0.47[29]
BDD	$[C_2mim][NTf_2]$	0.13[*]
BDD	0.1M KOH	0.14[41]
BDD	0.1M KOH[a]	0.24[3]
BDD	acetamide-urea-ammonium nitrate eutectic melt[b]	0.4[42]
BDD, $C(sp^2)$ modified	0.1M $HClO_4$	0.28 to 0.63[37]
BDD, $C(sp^2)$ modified	0.1M NaOH	0.54 to 0.93[37]
HOPG	0.1M KOH	0.16[41]

[*] This work [a] Simulated $1e^-$ reduction to $O_2^{\bullet-}$, ECE [b] 298 K

This table shows that the transfer coefficient obtained in the present work for O_2 reduction on GC (0.39) matches the values found in the literature for various RTILs (0.39 – 0.47)[13, 29] quite well. Comparison of the transfer coefficient obtained in this chapter on BDD is more difficult, as less attention has been given to O_2 reduction on BDD thus far. However, the value obtained (0.13) is similar to that reported for O_2 reduction at BDD in an aqueous 0.1 M NaOH solution (0.14)[41].

It has thus been demonstrated in this chapter that the reduction of oxygen at BDD and GC electrodes in $[C_2mim][NTf_2]$ occurs *via* the $1e^-$ reduction to superoxide. The kinetics for this process are much slower at the BDD electrode (ΔE_{pp} = 1.39 V) compared to GC (ΔE_{pp} = 0.12 V), presumably due to a lower density of electronic states around the formal potential of O_2 reduction in

$[C_2mim][NTf_2]$. The reduced kinetics for oxygen reduction at BDD could prove very useful for the investigation of systems under atmospheric conditions, where atmospheric oxygen would normally interfere.

5.4 Conclusions

The reduction of O_2 on boron-doped diamond and glassy carbon electrodes was studied in the $[C_2mim][NTf_2]$ ionic liquid. The reduction of oxygen at the boron-doped diamond predominantly involves the $1e^-$ reduction of oxygen to superoxide. Trace water lead to the formation of hydroperoxyl species, most likely formed by the proton-induced disproportionation of the superoxide anion. The formation of the superoxide was verified by repeating the reduction on BDD in the presence of benzoic acid, with a resultant decrease in the superoxide oxidation peak and increase in the peaks ascribed to the oxidation of the hydroperoxyl species. The reduction of oxygen was found to be quasi-reversible on glassy carbon (ΔE_{pp} = 0.12 V) and irreversible on boron-doped diamond (ΔE_{pp} = 1.39 V), with electron transfer coefficients of 0.39 and 0.13, respectively. The significantly slower kinetics observed on the boron-doped diamond electrode compared to those on the glassy carbon are likely related to the lower electronic density of states of BDD around the formal potential of O_2 reduction in $[C_2mim][NTf_2]$, as reported previously in aqueous media[3]. Having investigated the voltammetry of oxygen in the $[C_2mim][NTf_2]$ ionic liquid, the following chapter considers the electrodeposition of Zn(II), onto glassy carbon electrodes, in the $[C_4mPyrr][NTf_2]$ ionic liquid.

References

1. S. Ernst, L. Aldous and R. G. Compton, *Journal of Electroanalytical Chemistry*, 2011, 663, 108-112.
2. E. Yeager, *Journal of Molecular Catalysis*, 1986, 38, 5-25.
3. T. Yano, D. A. Tryk, K. Hashimoto and A. Fujishima, *Journal of the Electrochemical Society*, 1998, 145, 1870-1876.
4. T. Yano, E. Popa, D. A. Tryk, K. Hashimoto and A. Fujishima, *Journal of the Electrochemical Society*, 1999, 146, 1081-1087.
5. D. L. Maricle and W. G. Hodgson, *Analytical Chemistry*, 1965, 37, 1562-1565.
6. D. T. Sawyer, G. Chiericato, C. T. Angelis, E. J. Nanni and T. Tsuchiya, *Analytical Chemistry*, 1982, 54, 1720-1724.
7. M. T. Carter, C. L. Hussey, S. K. D. Strubinger and R. A. Osteryoung, *Inorganic Chemistry*, 1991, 30, 1149-1151.
8. M. C. Buzzeo, O. V. Klymenko, J. D. Wadhawan, C. Hardacre, K. R. Seddon and R. G. Compton, *Journal of Physical Chemistry A*, 2003, 107, 8872-8878.
9. M. C. Buzzeo, O. V. Klymenko, J. D. Wadhawan, C. Hardacre, K. R. Seddon and R. G. Compton, *Journal of Physical Chemistry B*, 2004, 108, 3947-3954.
10. R. G. Evans, O. V. Klymenko, S. A. Saddoughi, C. Hardacre and R. G. Compton, *Journal of Physical Chemistry B*, 2004, 108, 7878-7886.
11. E. I. Rogers, X.-J. Huang, E. J. F. Dickinson, C. Hardacre and R. G. Compton, *J Phys Chem C*, 2009, 113, 17811-17823.
12. X. J. Huang, E. I. Rogers, C. Hardacre and R. G. Compton, *Journal of Physical Chemistry B*, 2009, 113, 8953-8959.
13. I. M. AlNashef, M. L. Leonard, M. C. Kittle, M. A. Matthews and J. W. Weidner, *Electrochemical and Solid-State Letters*, 2001, 4, D16-D18.
14. R. G. Compton, J. S. Foord and F. Marken, *Electroanalysis*, 2003, 15, 1349-1363.
15. Y. Einaga, R. Sato, H. Olivia, D. Shin, T. A. Ivandini and A. Fujishima, *Electrochimica Acta*, 2004, 49, 3989-3995.

16. A. Kraft, *Int J Electrochem Sc*, 2007, 2, 355-385.
17. D. S. Silvester, L. Aldous, M. C. Lagunas, C. Hardacre and R. G. Compton, *Journal of Physical Chemistry B*, 2006, 110, 22035-22042.
18. F. Andre, P. Hapiot and C. Lagrost, *Physical Chemistry Chemical Physics*, 2010, 12, 7506-7512.
19. D. H. Chin, G. Chiericato, E. J. Nanni and D. T. Sawyer, *Journal of the American Chemical Society*, 1982, 104, 1296-1299.
20. C. P. Andrieux, P. Hapiot and J. M. Saveant, *Journal of the American Chemical Society*, 1987, 109, 3768-3775.
21. P. S. Singh and D. H. Evans, *Journal of Physical Chemistry B*, 2005, 110, 637-644.
22. K. E. Toghill and R. G. Compton, *Electroanalysis*, 2010, 22, 1947-1956.
23. M. Yoshimura, K. Honda, T. Kondo, R. Uchikado, Y. Einaga, T. N. Rao, D. A. Tryk and A. Fujishima, *Diamond and Related Materials*, 2002, 11, 67-74.
24. D. J. Riley and G. Pastor-Moreno, *Electrochimica Acta*, 2002, 47, 2589-2595.
25. G. Pastor-Moreno and D. J. Riley, *Electrochemistry Communications*, 2002, 4, 218-221.
26. C. Villagrán, L. Aldous, M. C. Lagunas, R. G. Compton and C. Hardacre, *Journal of Electroanalytical Chemistry*, 2006, 588, 27-31.
27. F. De Giorgio, F. Soavi and M. Mastragostino, *Electrochemistry Communications*, In Press, Accepted Manuscript.
28. R. G. Compton and C. E. Banks, *Understanding voltammetry, 2nd ed.*, World Scientific, Singapore ; London, 2011.
29. D. Zhang, T. Okajima, F. Matsumoto and T. Ohsaka, *Journal of the Electrochemical Society*, 2004, 151, D31-D37.
30. W. He, D. S. Silvester, I. Streeter, L. Aldous, C. Hardacre and R. G. Compton, *Journal of Physical Organic Chemistry*, 2009, 22, 69-76.
31. P. A. Z. Suarez, C. S. Consorti, R. F. De Souza, J. Dupont and R. S. Gonçalves, *Journal of the Brazilian Chemical Society*, 2002, 13, 106-109.
32. Q. Li, C. Batchelor-McAuley, N. S. Lawrence, R. S. Hartshorne and R. G. Compton, *ChemPhysChem*, 2011, 12, 1255-1257.

33. H. Gerischer, R. McIntyre, D. Scherson and W. Storck, *The Journal of Physical Chemistry*, 1987, 91, 1930-1935.
34. R. McIntyre, D. Scherson, W. Storck and H. Gerischer, *Electrochimica Acta*, 1987, 32, 51-53.
35. R. L. McCreery, *Chemical Reviews*, 2008, 108, 2646-2687.
36. M. C. Granger, M. Witek, J. Xu, J. Wang, M. Hupert, A. Hanks, M. D. Koppang, J. E. Butler, G. Lucazeau, M. Mermoux, J. W. Strojek and G. M. Swain, *Analytical Chemistry*, 2000, 72, 3793-3804.
37. J. A. Bennett, J. Wang, Y. Show and G. M. Swain, *Journal of the Electrochemical Society*, 2004, 151, E306-E313.
38. J. Xu, Q. Chen and G. M. Swain, *Analytical Chemistry*, 1998, 70, 3146-3154.
39. K. B. Holt, A. J. Bard, Y. Show and G. M. Swain, *The Journal of Physical Chemistry B*, 2004, 108, 15117-15127.
40. N. R. Wilson, S. L. Clewes, M. E. Newton, P. R. Unwin and J. V. Macpherson, *The Journal of Physical Chemistry B*, 2006, 110, 5639-5646.
41. A. Sarapuu, K. Helstein, D. J. Schififrin and K. Tammeveski, *Electrochemical and Solid-State Letters*, 2005, 8, E30-E33.
42. V. S. Dilimon, N. S. Venkata Narayanan and S. Sampath, *Electrochimica Acta*, 2010, 55, 5930-5937.

6. Electrodeposition and Stripping of Zn(II) in $[C_4mPyrr][NTf_2]$

This chapter investigates the mechanisms for the electrodeposition and stripping of $Zn^{2+}|Zn$ in the $[C_4mPyrr][NTf_2]$ ionic liquid *via* cyclic voltammetry. Tafel analysis shows that the deposition of Zn onto a bulk Zn surface occurs *via* a two electron process, with the first electron transfer being rate determining. The electrodissolution is found to occur *via* a potential-dependant mechanism with the first electron transfer being rate determining near the formal potential, while an intermediate chemical step becomes rate determining at more positive potentials. The work presented in this chapter has been published in the *Journal of Solid State Electrochemistry*[1].

6.1 Introduction

In a multi-electron process, the rate determining step can change with potential, although examples of this effect are rare. Below, the example of the two electron reduction of zinc(II), in the $[C_4mPyrr][NTf_2]$ ionic liquid is used to demonstrate a potential-dependant change in the mechanism of anodic Zn dissolution.

Applying the principle of microscopic reversibility to electron transfer reactions suggests that oxidation and reduction should both occur *via* the same pathway. Consequently, for the generalised multi-electron process;

$$A \pm ne^- \rightleftarrows B \tag{5.1}$$

both the oxidative and back reactions should proceed *via* the same transition state. As such the cathodic (α) and anodic (β) Butler-Volmer electron transfer coefficients, which indicate the position of the transition state, are related *via* $\alpha + \beta = n$, where n represents the total number of electrons transferred. This relationship holds for a given potential, but during a voltammetric experiment the potential is varied, causing changes in the local energetic environment such as altering the electrode solvation and/or double layer properties. Therefore, the relative position of the transition state may vary as the potential changes, resulting in potential-dependent transfer coefficients.

The transfer coefficient can only be measured when Faradaic current is passed. As such it is therefore only possible to measure α at reducing potentials and β at oxidising potentials. Thus for irreversible electrochemical systems, which exhibit highly separated reductive and oxidative peaks, the potentials at which the two transfer coefficients are measured may differ greatly. Thus, it is possible to measure $\alpha + \beta \neq n$ without violating the principle of microscopic reversibility[2-4]. The switch of β with potential for the oxidation of Zn is reported below.

The electrodeposition and anodic dissolution of zinc has been studied previously in aqueous[5-11], molecular organic[12-14] and ionic liquid[15-23] systems, largely in the field of corrosion research. However, there is debate as to the mechanisms of zinc electrodeposition and dissolution in the various solvents.

Cachet and Wiart have studied the anodic dissolution of zinc in aqueous chloride[5] and sulphate[6, 7] solutions, proposing complex mechanisms involving up to

three parallel dissolution paths and up to three adsorbed intermediates; $Zn^{+}_{(ads)}$, $Zn^{2+}_{(ads)}$ and $Zn(OH)^{+}_{(ads)}$.

Banaś et al. studied Zn stripping from a zinc anode in methanolic and aqueous lithium chloride solutions, both in the presence and in the absence of oxygen[12]. In the deoxygenated methanolic system, the anodic dissolution of zinc was found to occur *via* two separate mechanisms, depending on overpotential. The Tafel analysis performed by Banaś et al. yielded slopes of ~40 and ~120 mV/decade, depending on the overpotential. These values correspond to a transfer coefficient of ~1.5 near the formal potential, changing to ~0.5 at higher overpotential. Furthermore, Banaś et al. found that the anodic dissolution of Zn was hindered by the formation of a passivating layer when the methanolic solutions were exposed to oxygen or when the experiment was carried out in de/oxygenated H_2O.

More recent work by Światowska-Mrowiecka and Banaś investigated the anodic stripping of zinc from distinct (0001) and $(11\bar{2}0)$ crystal faces in deoxygenated, methanolic lithium perchlorate solutions[13]. This work found that the anodic dissolution of zinc proceeds *via* a two step mechanism with a fast, quasi-reversible formation of $Zn^{+}_{(ads)}$ followed by the rate determining step yielding Zn^{2+}. Furthermore, in contrast to the earlier work by Banaś et al., the two redox waves were shown to be separated by circa 300 mV[13].

6. Electrodeposition and Stripping of Zn(II) in [C_4mPyrr][NTf_2]

Pérez et al. found that the reduction of Zn^{2+} to Zn(Hg) in 1M aqueous $NaClO_4$ proceeds *via* an EEC mechanism, with electron transfer coefficients of 0.45, 0.52 and 0.982 for the respective steps[8].

Hassan et al. demonstrated that a surface ZnO and $Zn(OH)_2$/ZnO passivating film was formed during the anodic dissolution in aqueous perchlorate solutions, with the passivating nature of the film decreasing upon deoxygenation of the solutions[9-11].

Białłozór and Bandura studied the electrodeposition and stripping of Zn in dimethylsulfoxide (DMSO), N,N-dimethylformamide (DMF) and acetonitrile (MeCN), finding that in all cases the reaction involved two one-electron transfer reactions[14]. Furthermore, while the cathodic transfer coefficient, α, was found to be ~0.5 in all three solvents, the anodic transfer coefficient, β, was determined to be ~0.5 in DMSO and ~1 in DMF and MeCN[14]. This work by Białłozór and Bandura represents the only insights into the electron transfer mechanisms of Zn electrodeposition and stripping in aprotic solvents in the literature and suggests that in all of the solvents studied, the electrodeposition and stripping of Zn proceeds *via* the two-step mechanism[14];

$$Zn^{2+} + e^- \rightleftarrows Zn^+ \tag{5.2}$$

$$Zn^+ + e^- \rightleftarrows Zn \tag{5.3}$$

where the Zn^+ intermediate and possibly the Zn^{2+} intermediate may be adsorbed on the electrode surface. Although this is not mentioned directly in the paper by

Białłozór and Bandura[14], analogy to the protic systems mentioned above suggest that this is a reasonable assumption. Furthermore, Białłozór and Bandura also observed that in MeCN, multicyclic voltammograms yielded decreased reduction peaks as a passivating layer was formed *via* a secondary chemical reaction, whereby it was speculated that anion radicals were formed *via*;

$$Zn^{+} + R \rightleftarrows Zn^{2+} + R^{-} \tag{5.4}$$

and the R^{-} radicals then initiated the polymerisation of solvent molecules and the adsorption of these products on the cathodic scan caused a partial blocking of the electrode surface[14]. However, Białłozór and Bandura did not rule out the possibility that the anion radicals were formed *via* the electrocatalytic reduction of solvent molecules on the freshly deposited zinc.

The electrodeposition of Zn has also been studied in room temperature ionic liquids, with papers describing deposition from chlorozincate[15] & chloroaluminate[16] imidazolium molten salts, choline chloride-based deep eutectic solvents[17-20], tributylmethylammonium bis(trifluoromethylsulfonyl)imide, $[N_{4,4,4,1}][NTf_2]$[21] and *N*-butyl-*N*-methylpyrrolidinium dicyanamide, $[C_4mPyrr][DCA]$[22, 23]. However, these papers focus on the morphologies of Zn deposits, as well as crystal nucleation/growth mechanisms, as opposed to the electron transfer mechanisms involved and are primarily concerned with the electroplating of zinc.

The present work thus investigates the electron transfer mechanisms for the $Zn^{2+}|Zn$ electrodeposition and stripping in a $[C_4mPyrr][NTf_2]$ ionic liquid by cyclic

voltammetry. The $[C_4mPyrr][NTf_2]$ ionic liquid was chosen for its large potential window as well as its persistence under vacuum, which reduces the probability of forming the passivating oxide/hydroxide layers seen previously in aqueous and non-aqueous systems[5-7, 9-14]. Furthermore, the zinc was introduced to the ionic liquid as the bis(trifluoromethylsulfonyl)imide salt, $Zn[NTf_2]_2$, so as to minimise any confusion around Zn(II) speciation[22, 23] and the effects of anions on zinc electrodissolution, seen previously in aqueous[24] and organic[12] systems.

6.2 Experimental

$Zn[NTf_2]_2$ was synthesised *via* a neutralization reaction by adding a 50% molar excess of ZnO to an aqueous solution of $H[NTf_2]$ and stirring overnight until pH-neutral[25, 26]. The resulting slurry was then filtered through a sintered glass frit and the (clear and colourless) filtrate was dried under rotary evaporation and then high vacuum ($P = 0.018 \pm 0.002$ mbar) overnight to yield large white flakes.

Electrochemical measurements were performed in a thermostated (25.0 ± 0.1 °C) Faraday cage, employing a glassy carbon (GC, r = 1.5mm, BASi) working electrode, a platinum mesh (99.9%, Goodfellow) counter electrode and a Ag/Ag^+ reference electrode. The experiment was prepared by placing 100 μl of 100 mM $Zn[NTf_2]_2$ in $[C_4mPyrr][NTf_2]$ into a sample chamber on top of the GC electrode.

6.3 Results and Discussion

A 100 mM solution of $Zn[NTf_2]_2$ in $[C_4mPyrr][NTf_2]$ was placed under vacuum to remove any residual H_2O and O_2 present, as these species have previously been

shown to interfere with electrochemical measurements in ionic liquids.[27-30] Cyclic voltammograms (CVs) were then recorded for the electrodeposition and stripping of Zn at the GC working electrode. One such CV is shown in Figure 18, where the potential was scanned from 0 to -1.8 and back to 0 V (vs. Ag/Ag^+) at a rate of 10 mV/s and a step size of ~1 mV.

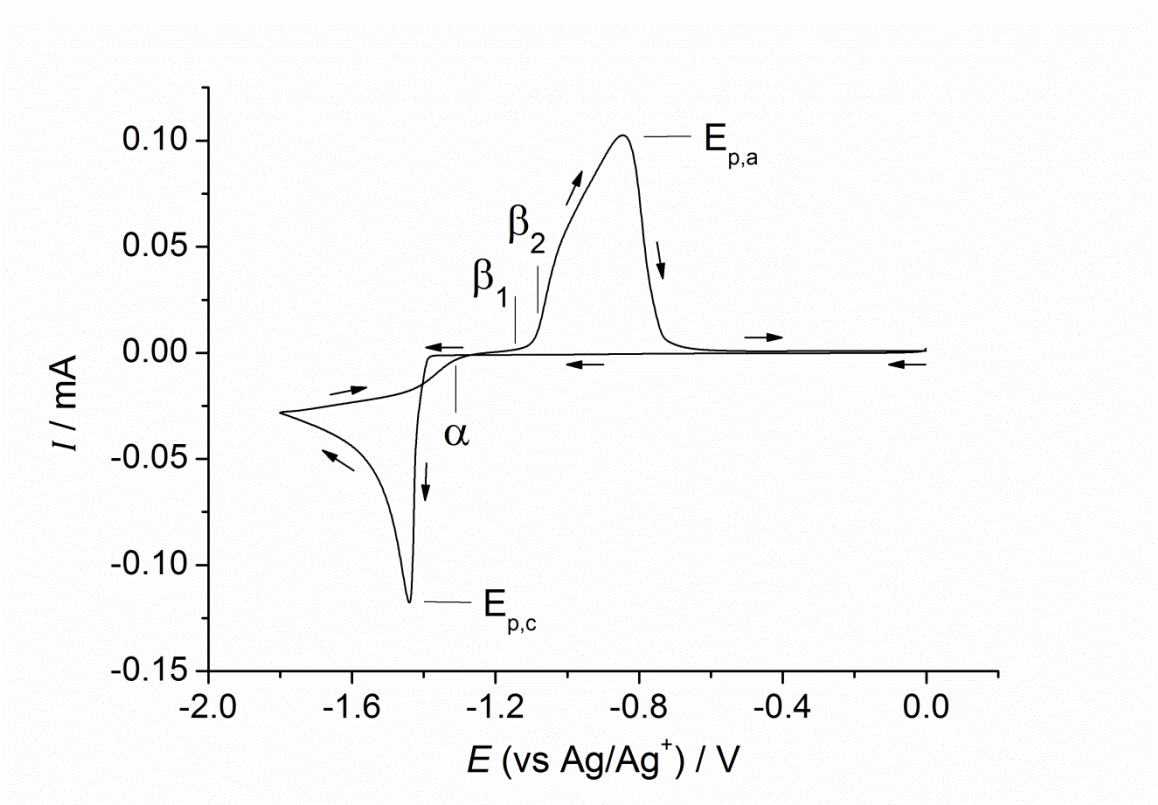


Figure 18 - CV showing the electrodeposition and stripping of $Zn^{2+}|Zn$ onto a GC electrode in $[C_4mPyrr][NTf_2]$, recorded at 25 °C and 10 mV/s. The symbols α, β_1 and β_2 indicate the regions on the curve which gave the Tafel plots described in the text.

Evident in the figure are two peaks, $E_{p,c}$ and $E_{p,a}$, representing the cathodic and anodic processes, respectively. Also evident is the so-called "nucleation loop", where the currents of the forward and reverse sweeps cross over. This nucleation loop is characteristic of systems in which metals are deposited onto foreign

substrates, as a higher overpotential is required for nucleation at the surface than for the growth of an existing deposit.[31] The cathodic and anodic peaks $E_{p,c}$ and $E_{p,a}$ occur at -1.44 and -0.85 V *vs.* Ag/Ag^+, respectively.

The mechanisms behind electrochemical processes can often be elucidated with the help of Tafel analysis where, for a multiple electron mechanism, a plot of $\ln(I)$ vs. E allows the rate limiting step to be determined, for a reduction[32, 33], *via*;

$$\frac{\partial \ln(I)}{\partial E} = \frac{-(n' + \alpha_{n'}) \cdot F}{R \cdot T} \tag{5.5}$$

or for an oxidation[33] *via*;

$$\frac{\partial \ln(I)}{\partial E} = \frac{(n' + \beta_{n'}) \cdot F}{R \cdot T} \tag{5.6}$$

where I is the current, E the potential, n' the number of electrons transferred before the rate limiting step and $\alpha_{n'}$ and $\beta_{n'}$ are the electron transfer coefficients of the rate determining steps for the reduction and oxidation, respectively. F is the Faraday constant, R the universal gas constant and T the temperature.

In order to analyse the mechanisms involved in the electrodeposition and stripping of the $Zn^{2+}|Zn$ couple, omitting the nucleation and growth of Zn on the glassy carbon phase, a plot of $\ln(I)$ vs. E was constructed from the reverse scan shown in Figure 18. This plot yielded three linear Tafel regions, which are highlighted above in Figure 18 and presented as Figure 19 to Figure 21.

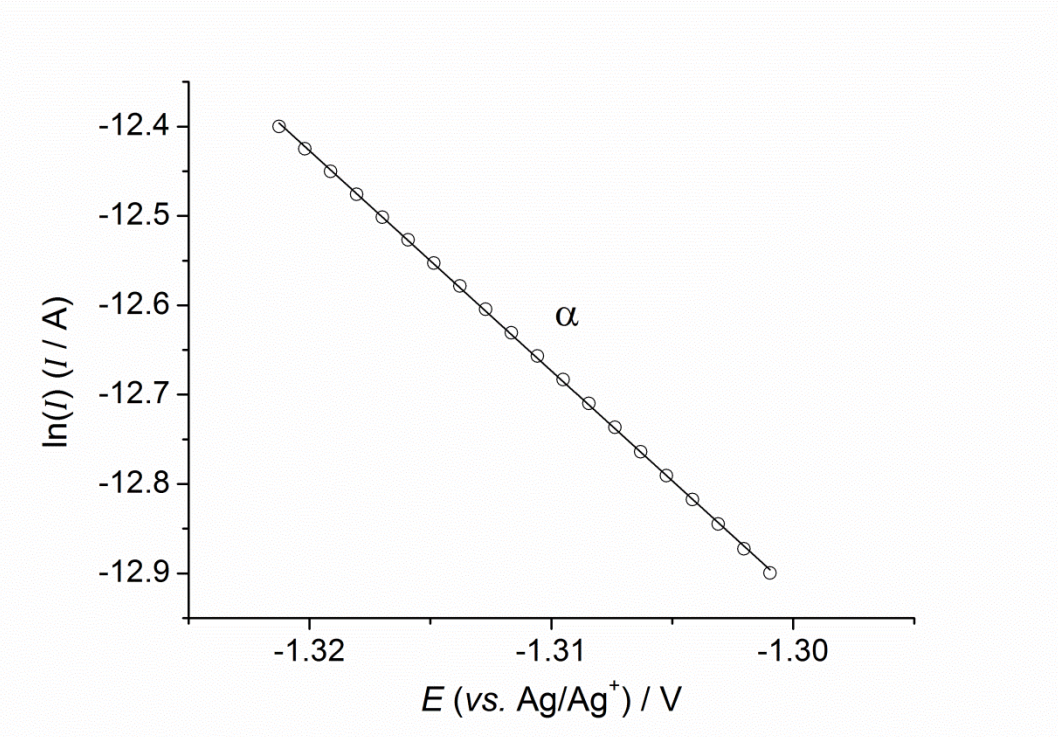


Figure 19 - Tafel plot for the deposition of Zn onto Zn close to the formal potential of the Zn^{2+}|Zn couple.

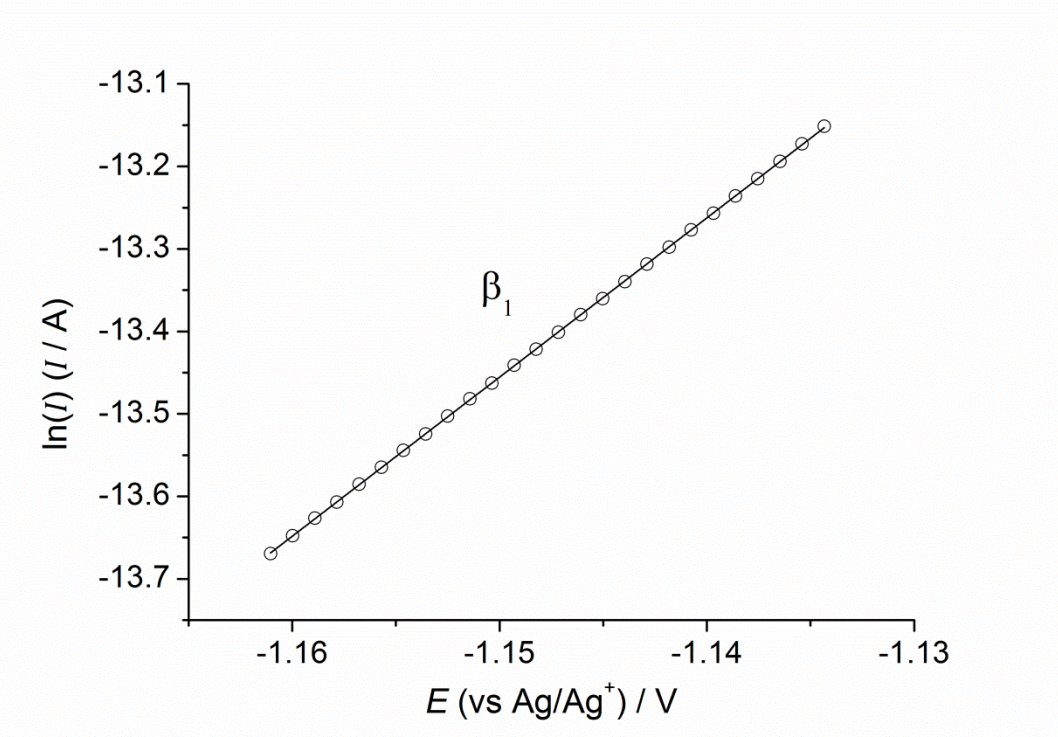


Figure 20 - Tafel plot for the stripping of Zn from Zn close to the formal potential of the Zn^{2+}|Zn couple.

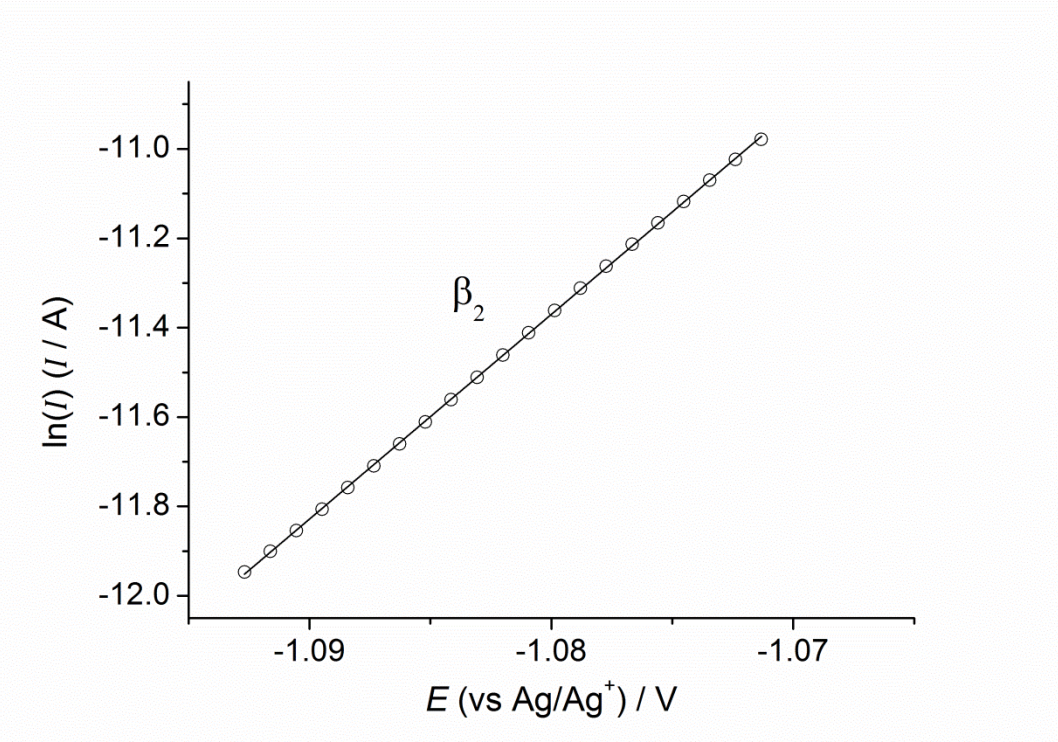


Figure 21 - Tafel plot for the stripping of Zn from Zn further from the formal potential of the Zn^{2+}|Zn couple.

Figure 19 to Figure 21 show Tafel plots of ln(I) vs. E for the deposition and stripping of the Zn^{2+}|Zn couple onto glassy carbon in $[C_4mPyrr][NTf_2]$, constructed using data shown in Figure 18. The figures highlight the three distinct Tafel regions shown as α, β_1 and β_2 in Figure 18. The regression lines for α, β_1 and β_2 in Figure 19 to Figure 21 were found to be $\ln(I)$=-24.62E-44.93, $\ln(I)$=19.30E+8.738 and $\ln(I)$=45.83E+38.13, respectively, having adjusted R^2 values of 0.99981, 0.99998 and 0.99991, respectively. The values of (n_1' + α), (n_2' + β_1) and (n_3' + β_2), obtained from the slopes of the lines of best fit in Figure 19 to Figure 21, *via* (3), were found to be 0.63 ± 0.09, 0.57 ± 0.09 and 1.13 ± 0.07, respectively (where the values and uncertainties were derived from averaged

measurements). The value for the cathodic transfer coefficient (α) of 0.63 ± 0.09 suggests that n_1' equals zero and hence the first electron transfer is rate determining. Thus the electrodeposition of Zn^{2+} onto Zn proceeds *via*;

$$Zn^{2+}_{(RTIL)} + e^- \xrightarrow{slow} Zn^{+}_{(ads/RTIL)} \quad (5.7)$$

$$Zn^{+}_{(ads/RTIL)} + e^- \xrightarrow{fast} Zn_{(s)} \quad (5.8)$$

where the subscripts (RTIL) and (s) refer to the solvated and solid states, respectively, while the subscript (ads/RTIL) refers to the fact that the Zn^+ species may be adsorbed, solvated or a combination of the two. There have been no reports as to the nature of Zn^{2+} and Zn^+ solvation in the $[C_4mPyrr][NTf_2]$ RTIL, however the possibility of ion pairing cannot be ruled out. The value of the anodic transfer coefficient close to the formal potential (β_1), 0.57 ± 0.09, suggests that n_2' is zero and the first electron transfer is again rate-limiting. Thus, the electrodissolution of Zn from the bulk zinc surface at potentials close to the formal potential occurs *via*;

$$Zn_{(s)} \xrightarrow{slow} Zn^{+}_{(ads/RTIL)} + e^- \quad (5.9)$$

$$Zn^{+}_{(ads/RTIL)} \overset{fast}{\rightleftharpoons} Zn^{2+}_{(RTIL)} + e^- \quad (5.10)$$

However, as the potential is swept to increasingly positive values, a shift in the anodic transfer coefficient from 0.57 ± 0.09 (n_2' + β_1) to 1.13 ± 0.07 (n_3' + β_2) implies a change of mechanism, with n_3' = 1, and the stripping occurs *via* an ECE mechanism where the first, now fast, step is given by;

6. Electrodeposition and Stripping of Zn(II) in [C_4mPyrr][NTf_2]

$$\mathrm{Zn}_{(\mathrm{s})} \overset{\text{fast}}{\rightleftharpoons} \mathrm{Zn}^{+}_{(\mathrm{ads/RTIL})} + \mathrm{e}^{-} \tag{5.11}$$

This fast step is then followed by the rate determining chemical step, which may be one of the following;

$$\mathrm{Zn}^{+}_{(\mathrm{ads})} \xrightarrow{\text{slow}} \mathrm{Zn}^{+}_{(\mathrm{RTIL})} \tag{5.12}$$

$$\mathrm{Zn}^{+}_{(\mathrm{RTIL})}(\mathrm{A}) \xrightarrow{\text{slow}} \mathrm{Zn}^{+}_{(\mathrm{RTIL})}(\mathrm{B}) \tag{5.13}$$

$$2\mathrm{Zn}^{+}_{(\mathrm{ads/RTIL})} \xrightarrow{\text{slow}} \mathrm{Zn}_{(\mathrm{s})} + \mathrm{Zn}^{2+}_{(\mathrm{ads/RTIL})} \tag{5.14}$$

representing desorption, a change in solvation (where (A) and (B) represent different solvated states) or disproportionation, respectively. This slow, rate determining, chemical step is then followed by another fast electrochemical step;

$$\mathrm{Zn}^{+}_{(\mathrm{ads/RTIL})} \overset{\text{fast}}{\rightleftharpoons} \mathrm{Zn}^{2+}_{(\mathrm{RTIL})} + \mathrm{e}^{-} \tag{5.15}$$

Thus, the rate determining step of the electrodissolution of Zn switches as the potential is swept further in the positive direction. Note that the stripping of Zn occurs from the bulk Zn surface, not from the GC electrode, at the potentials of β_1 and β_2 as even at $\mathrm{E}_{\mathrm{p,a}}$ approximately 24 layers of Zn remain on the electrode (based on $m/A = Q/nFA$ comparisons to an ideal monolayer of basal plane Zn).

It has been demonstrated in this chapter that the electrodeposition of zinc occurs *via* an EE or ECE mechanism, with the first reduction step being rate limiting. Furthermore, the electrodissolution of the deposited layer occurs either through an EE or ECE mechanism, with the first E step being rate limiting at

potentials near the formal potential and a chemical step becoming rate limiting at more positive potentials.

6.4 Conclusions

The electrodeposition and stripping of the Zn^{2+}|Zn couple onto and from a bulk zinc deposit on a glassy carbon electrode has been investigated in the [C_4mPyrr][NTf_2] ionic liquid. The cathodic and anodic Tafel behaviour was analysed and a single cathodic and two anodic electron transfer coefficients were found to be 0.63 ± 0.09, 0.57 ± 0.09 and 1.13 ± 0.07, respectively. This implies that the electrodeposition of Zn occurs *via* an EE or ECE mechanism with the first step being rate determining, while the electrodissolution of Zn occurs *via* two different mechanisms depending on the applied potential. Close to the formal potential, the stripping occurs *via* an EE or ECE mechanism with a rate determining first step, however, at more positive potentials a chemical step occurring after the initial electron transfer becomes rate limiting and hence the mechanism shifts to an ECE form. Having investigated the electrodeposition and stripping of Zn(II) in the [C_4mPyrr][NTf_2] ionic liquid, the following chapter describes the fabrication of zinc microelectrodes and their electrochemical behaviour.

References

1. S. Ernst, M. Henstridge and R. Compton, *J Solid State Electrochem*, 2012, 16, 2329-2333.
2. J.-M. Savéant and D. Tessier, *Faraday Discussions of the Chemical Society*, 1982, 74, 57-72.
3. D. A. Corrigan and D. H. Evans, *Journal of Electroanalytical Chemistry*, 1980, 106, 287-304.
4. D. Suwatchara, M. C. Henstridge, N. V. Rees and R. G. Compton, *The Journal of Physical Chemistry C*, 2011, 115, 14876-14882.
5. C. Cachet and R. Wiart, *Journal of Electroanalytical Chemistry and Interfacial Electrochemistry*, 1981, 129, 103-114.
6. C. Cachet, F. Ganne, G. Maurin, J. Petitjean, V. Vivier and R. Wiart, *Electrochimica Acta*, 2001, 47, 509-518.
7. C. Cachet, F. Ganne, S. Joiret, G. Maurin, J. Petitjean, V. Vivier and R. Wiart, *Electrochimica Acta*, 2002, 47, 3409-3422.
8. M. Pérez, A. Baars, S. J. M. Zevenhuizen, M. Sluyters-Rehbach and J. H. Sluyters, *Journal of Electroanalytical Chemistry*, 1995, 397, 87-92.
9. H. H. Hassan, *Applied Surface Science*, 2001, 174, 201-209.
10. H. H. Hassan, *Electrochimica Acta*, 2006, 51, 5966-5972.
11. H. H. Hassan, M. A. Amin, S. Gubbala and M. K. Sunkara, *Electrochimica Acta*, 2007, 52, 6929-6937.
12. J. Banaś, K. G. Schütze and E. Heitz, *Journal of the Electrochemical Society*, 1986, 133, 253-259.
13. J. Światowska-Mrowiecka and J. Banaś, *Electrochimica Acta*, 2005, 50, 1829-1840.
14. S. Białłozór and E. T. Bandura, *Electrochimica Acta*, 1987, 32, 891-894.
15. Y.-F. Lin and I. W. Sun, *Electrochimica Acta*, 1999, 44, 2771-2777.
16. J. Dogel and W. Freyland, *Physical Chemistry Chemical Physics*, 2003, 5, 2484.
17. A. P. Abbott, J. C. Barron and K. S. Ryder, *Transactions of the Institute of Metal Finishing*, 2009, 87, 201-207.

18. A. H. Whitehead, M. Polzler and B. Gollas, *Journal of the Electrochemical Society*, 2010, 157, D328-D334.
19. A. P. Abbott, J. C. Barron, G. Frisch, S. Gurman, K. S. Ryder and A. Fernando Silva, *Physical Chemistry Chemical Physics*, 2011, 13, 10224-10231.
20. A. P. Abbott, J. C. Barron, G. Frisch, K. S. Ryder and A. F. Silva, *Electrochimica Acta*, 2011, 56, 5272-5279.
21. P.-Y. Chen and C. L. Hussey, *Electrochimica Acta*, 2007, 52, 1857-1864.
22. M.-J. Deng, P.-Y. Chen, T.-I. Leong, I. W. Sun, J.-K. Chang and W.-T. Tsai, *Electrochemistry Communications*, 2008, 10, 213-216.
23. M.-J. Deng, P.-C. Lin, J.-K. Chang, J.-M. Chen and K.-T. Lu, *Electrochimica Acta*, 2011, 56, 6071-6077.
24. J. Yu, H. Yang, X. Ai and Y. Chen, *Russian Journal of Electrochemistry*, 2002, 38, 321-325.
25. H. Kobayashi, J. Nie and T. Sonoda, *Chemistry Letters*, 1995, 24, 307-308.
26. J. Nie, H. Kobayashi and T. Sonoda, *Catalysis Today*, 1997, 36, 81-84.
27. A. M. O'Mahony, D. S. Silvester, L. Aldous, C. Hardacre and R. G. Compton, *Journal of Chemical and Engineering Data*, 2008, 53, 2884-2891.
28. M. C. Buzzeo, O. V. Klymenko, J. D. Wadhawan, C. Hardacre, K. R. Seddon and R. G. Compton, *Journal of Physical Chemistry A*, 2003, 107, 8872-8878.
29. X. J. Huang, E. I. Rogers, C. Hardacre and R. G. Compton, *Journal of Physical Chemistry B*, 2009, 113, 8953-8959.
30. C. Zhao, A. M. Bond, R. G. Compton, A. M. O'Mahony and E. I. Rogers, *Analytical Chemistry*, 2010, 82, 3856-3861.
31. F. Endres, D. R. MacFarlane and A. P. Abbott, eds., *Electrodeposition from Ionic Liquids*, WILEY-VCH, Weinheim, 2008.
32. J. O. M. Bockris and A. K. N. Reddy, *Modern electrochemistry*, Plenum Press, New York, 1998.
33. R. G. Compton and C. E. Banks, *Understanding voltammetry, 2nd ed.*, World Scientific, Singapore ; London, 2011.

7. Fabrication of Zinc Microelectrodes

The previous chapter described the electrochemical deposition and stripping of zinc(II) in the $[C_4mPyrr][NTf_2]$ ionic liquid at glassy carbon electrodes. This chapter presents data regarding the novel and successful fabrication (from commercial zinc wire) and electrochemistry of zinc microelectrodes. These electrodes are later utilised for the reduction of 1-bromo-4-nitrobenzene in Chapter 9.

7.1 Introduction

The standard procedure for fabricating microdisk electrodes for electrochemical applications involves sealing a wire of appropriate radius into a glass capillary by carefully melting the glass around the wire using a suitably designed electrode furnace[1]. However, this method is obviously not appropriate if either the melting point of the wire material is lower than that of the glass, or the wire material is very sensitive to air or moisture. Both of these points apply to zinc, which has a melting point of 420 °C[2] and is also converted to zinc oxide at elevated temperatures if any water is present[3].

These factors thus explain why there is no evidence in the literature describing the preparation of zinc microelectrodes. However, the group of Scherson have studied *in situ* Raman spectra of Zn passivating films formed electrochemically on individual zinc microparticles of *ca.* 50-120 μm diameter in 1 M aqueous KOH solutions[4]. They achieved this by "spearing" single quasi-spherical particles with

an electrochemically sharpened tungsten tip and then simultaneously recording the electrochemical and Raman signals. There are also reports in the literature which claim to use zinc "microelectrodes", however, these utilise electrodes with diameters of the order of a few mm[5, 6].

The following chapter describes the preparation of zinc microdisk electrodes and briefly compares their behaviour to that reported for single zinc microparticles. The voltammetry of the prepared zinc microelectrodes, in the $[C_4mPyrr][NTf_2]$ ionic liquid, is then compared to that described in Chapter 6 for electrochemically deposited zinc in the same ionic liquid.

7.2 Experimental

The method for preparing the zinc microelectrode involved first connecting a zinc wire (r = 12.5±1.25 μm, 99.0%, Goodfellow), to a length of copper connecting wire (r ≈ 1 mm) using silver epoxy (RS components) and rinsing with acetonitrile (≥ 99.9 %, Sigma-Aldrich) and ethanol (≥ 99.8 %, Sigma-Aldrich) to remove any possible organic contaminants from the surface. This wire assembly was then sealed in a thermally conductive epoxy (Epo-Tek H77, Epoxy Technology) inside a glass Pasteur pipette. The Pasteur pipette was first sealed closed at the thin end, by melting in a hot Bunsen flame, and coated in silicone spray lubricant (Tableau) prior to casting to minimise adhesion of the epoxy to the glass. After filling with epoxy, the entire electrode assembly was centrifuged at 1000 rpm for 3 minutes to remove any trapped air bubbles, before being placed

inside a box oven at 100 °C for 1 hour and then at 120 °C overnight. After removing the glass casing, the electrode was polished flat on a diamond wheel and then P1000, P2500 and finally P4000 silicon carbide paper before fine-polishing on alumina as usual. Preparation of zinc microelectrodes *via* this method was highly successful.

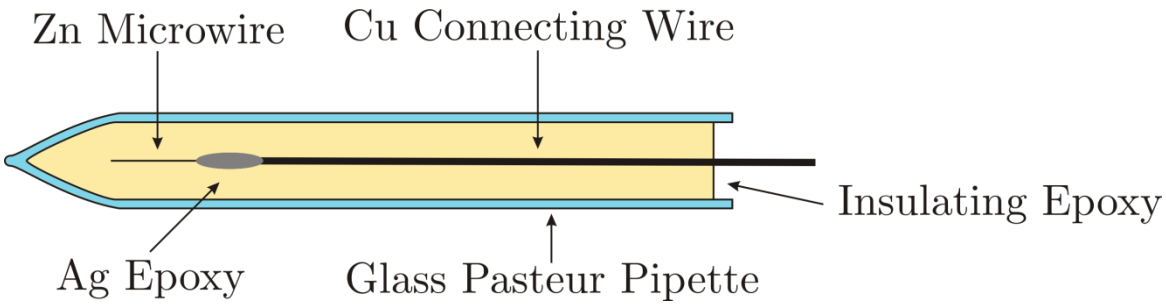


Figure 22 – Schematic detailing the fabrication of zinc microelectrodes.

The voltammetry of aqueous 1.0 M KOH solutions was obtained using a standard three electrode configuration, employing a graphite rod counter electrode and SCE reference. The voltammetry of the zinc microelectrodes in the $[C_4mPyrr][NTf_2]$ ionic liquid (50 μL) was obtained using a standard three electrode configuration, with a platinum wire counter electrode and a Ag/Ag^+ reference electrode. The Ag/Ag^+ reference was prepared, as shown in chapter 3, *via* a modified version of the method of Meng et al.[7], by attaching a 5Å, 1.6mm diameter molecular sieve (Aldrich) to the end of a cut-down glass Pasteur pipette using PTFE heatshrink. The Ag/Ag^+ reference electrode was then filled with a 20 mM solution of Ag[OTf] (>99.95%, Aldrich) in $[C_4mPyrr][NTf_2]$ and a silver wire was immersed in the solution.

7.3 Voltammetry of Zinc Microelectrodes in Aqueous KOH Solutions

A three-necked flask, containing 1.0 M KOH was set up with a zinc microelectrode, graphite rod counter electrode and SCE reference. The solution was de-gassed with nitrogen for at least 30 minutes prior to measurement and kept under a positive pressure of N_2 during measurement.

The potential was first held at −1.65 V for 10 seconds prior to measurement to ensure the zinc surface was completely reduced. The potential was then held at −1.35 V for 2 seconds before scanning from −1.35 to −1.65 to −0.65 and then back to −1.35 V at a scan rate of 100 mV s^{-1}. The resulting CV is shown below in Figure 23.

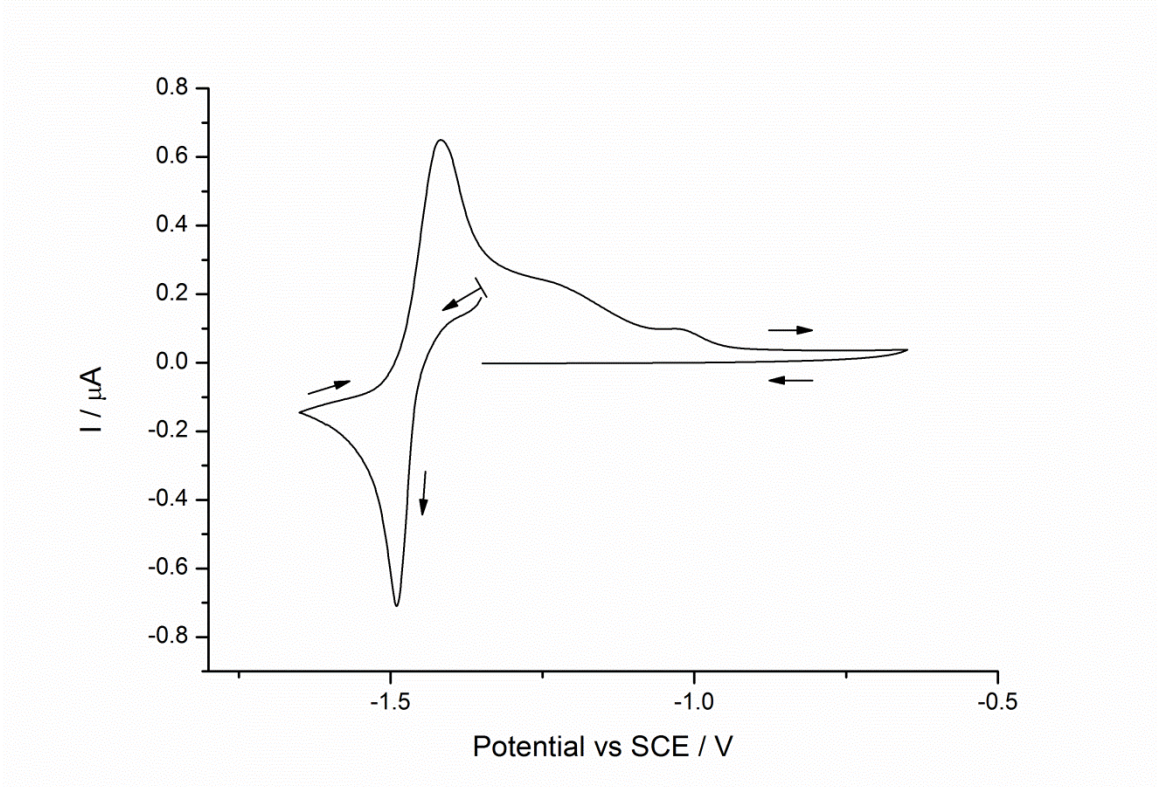


Figure 23 – Voltammetry of the zinc microelectrode (r = 12.5 μm) in a degassed 1.0 M aqueous KOH solution, recorded using a scan rate of 100 mV s^{-1}.

7. Fabrication of Zinc Microelectrodes

Figure 23 shows a single reduction peak at −1.49 V vs. the SCE reference, corresponding to the reduction of zinc(II) formed by holding at −1.35 V before the scan. The reverse sweep then shows three oxidation features, each of smaller magnitude than the preceding, at *ca.* −1.42, −1.24 and −1.03 V, respectively.

This behaviour agrees qualitatively with both that observed by the group of Scherson for single zinc microparticles[8] and with that observed by Cai and Park for zinc macroelectrodes[9]. Initially on the reverse sweep zinc is oxidised to $Zn(OH)_4^{2-}$ and as its concentration increases at the electrode surface, it becomes supersaturated and precipitates onto the electrode to form a pre-passive hydroxide-oxide layer[9]. At this point, the concentration of OH^- in the diffusion layer is depleted and the oxidation of zinc primarily forms the $Zn(OH)_3^-$ species[9]. After the second anodic peak, the remaining current was reported to be the result of the continuous oxidation of zinc in the Zn-doped ZnO film, which is limited in terms of mass transport of both reactants and products through the porous passive layer[9]. Thus, it was demonstrated in this section that the procedure outlined above is well suited for the construction of zinc microelectrodes and is likely also transferrable to other electrode materials for which traditional techniques are not suitable.

7.4 Voltammetry of Zinc Microelectrodes in ionic liquids

Having characterised the zinc microelectrodes in aqueous KOH solutions, their voltammetric behaviour in the $[C_4mPyrr][NTf_2]$ RTIL was examined. As described in Chapter 6, the electrodeposition of Zn^{2+} onto bulk Zn occurs *via*;

$$Zn^{2+}_{(RTIL)} + e^- \xrightarrow{\text{slow}} Zn^{+}_{(ads/RTIL)} \tag{6.1}$$

$$Zn^{+}_{(ads/RTIL)} + e^- \xrightarrow{\text{fast}} Zn_{(s)} \tag{6.2}$$

where the subscript (RTIL) refers to the solvated state, (s) the solid state and (ads/RTIL) to either a solvated or adsorbed state. The electrodissolution of Zn from the bulk zinc surface close to the formal potential then occurs *via*;

$$Zn_{(s)} \xrightarrow{\text{slow}} Zn^{+}_{(ads/RTIL)} + e^- \tag{6.3}$$

$$Zn^{+}_{(ads/RTIL)} \xrightleftharpoons{\text{fast}} Zn^{2+}_{(RTIL)} + e^- \tag{6.4}$$

and the dissolution at potentials further from the formal potential proceeds *via*;

$$Zn_{(s)} \xrightleftharpoons{\text{fast}} Zn^{+}_{(ads/RTIL)} + e^- \tag{6.5}$$

which is then followed by a rate-determining chemical step, which may be one of;

$$Zn^{+}_{(ads)} \xrightarrow{\text{slow}} Zn^{+}_{(RTIL)} \tag{6.6}$$

$$Zn^{+}_{(RTIL)}(A) \xrightarrow{\text{slow}} Zn^{+}_{(RTIL)}(B) \tag{6.7}$$

$$2Zn^{+}_{(ads/RTIL)} \xrightarrow{\text{slow}} Zn_{(s)} + Zn^{2+}_{(ads/RTIL)} \tag{6.8}$$

which is then followed by another fast electrochemical step;

7. Fabrication of Zinc Microelectrodes

$$Zn^{+}_{(ads/RTIL)} \overset{fast}{\rightleftharpoons} Zn^{2+}_{(RTIL)} + e^{-} \qquad (6.9)$$

In order to compare the stripping and re-deposition behaviour of the zinc microelectrodes with the deposition and stripping measured at glassy carbon electrodes, a zinc microelectrode was set up under vacuum with 50 μL of the $[C_4mPyrr][NTf_2]$ ionic liquid. The voltammetry obtained for the electrochemical stripping and deposition of the $Zn^{2+}|Zn$ couple, measured at a scan rate of 10 mV s^{-1}, is shown below in Figure 24.

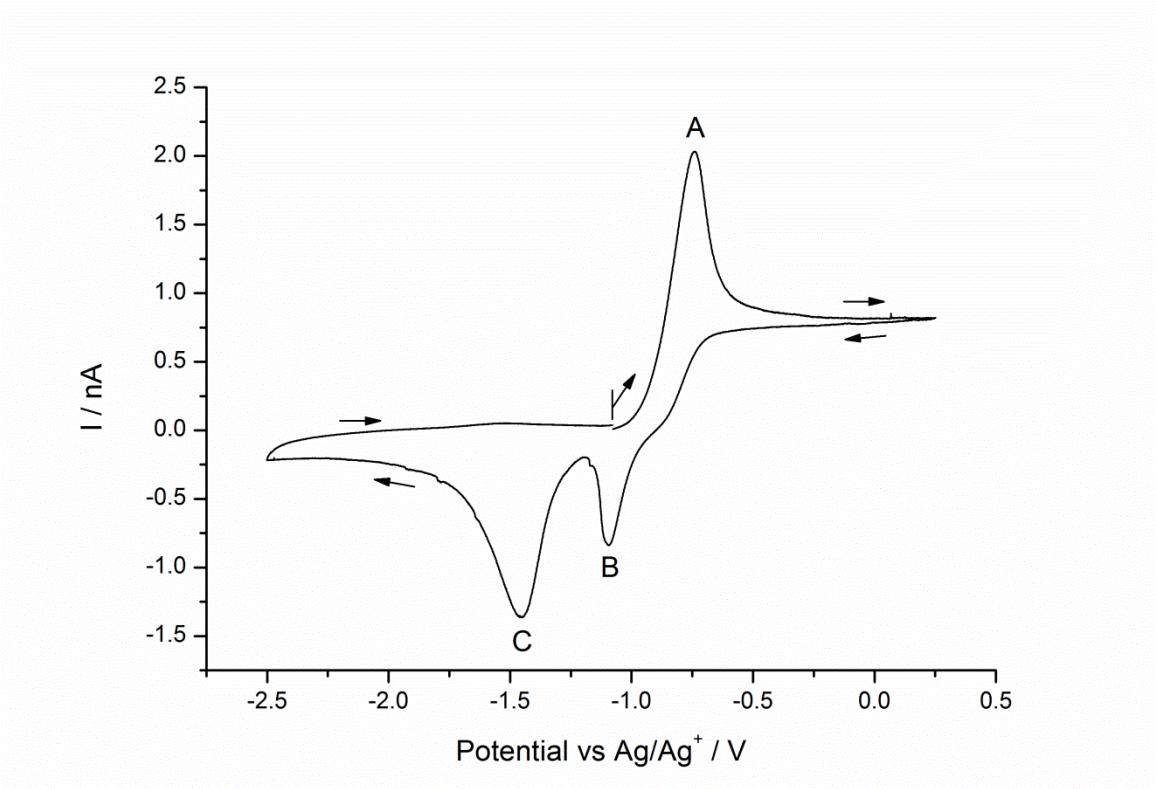


Figure 24 – Voltammetry of the zinc microelectrode (r = 12.5 μm) in the $[C_4mPyrr][NTf_2]$ ionic liquid, recorded under vacuum at a scan rate of 10 mV s^{-1}.

Apparent in the forward (anodic) sweep in Figure 24 is a single oxidation peak (A) at −0.741 V, after which a limiting current is established. On the reverse

(cathodic) sweep, in contrast to the electrodeposition on glassy carbon shown in chapter 6, two reduction peaks are seen (B and C). Peak C occurs at -1.45 V *vs.* the Ag/Ag^+ reference and as such corresponds to the deposition peak observed on glassy carbon (-1.44 V). Peak C is thus ascribed to the redeposition of Zn^{2+} from solution. Furthermore, this reduction begins at potentials less negative to those measured at glassy carbon electrodes as there is no nucleation overpotential required to initiate the deposition, which is evidenced by the lack of a nucleation loop. Peak B, however, occurs at *ca.* -1.09 V and was not observed for the electrodeposition onto glassy carbon. The most likely explanation for this additional peak would be the reduction of an adsorbed Zn^{2+} species formed in the rate-determining chemical step during dissolution. The peak may also be due to an adsorbed Zn^+ species, however this is less likely.

Based on $m/A = Q/nFA$ calculations, the area under peak B corresponds to either 6.35 or 12.7 "monolayers" for $n = 2$ and $n = 1$, respectively, compared to a theoretical monolayer coverage calculated from the coverage of zinc atoms on the (001) surface. Given that the electrode is likely considerably roughened during the electrodissolution, these values are not entirely unreasonable, however, the peak could also represent the reduction of an alternately solvated Zn^+ species, shown in equation (6.7), or the reduction of an oxide layer, but again this is unlikely as the voltammetry was obtained *in vacuo*.

Nonetheless, the main deposition and stripping peaks agree quite well with those seen for the electrodeposition and stripping of Zn(II) at glassy carbon

electrodes. Furthermore, the similarity of the voltammetry of the zinc microelectrodes in aqueous KOH solutions with that in the literature[8, 9] suggests that the technique described above for the fabrication of zinc microelectrodes is appropriate for the task.

7.5 Conclusions

A novel technique was successfully developed for the fabrication of zinc microdisk electrodes from commercially available zinc wire. The procedure was based around the concept of sealing the zinc microwire in a thermally conductive, electrically insulating epoxy resin. The voltammetry of the fabricated zinc microdisk electrodes was then compared with that observed in aqueous KOH solutions for single zinc microparticles and zinc macroelectrodes and good agreement was observed. The voltammetry of the zinc microdisk electrodes was then measured in the $[C_4mPyrr][NTf_2]$ RTIL and compared to that obtained for the deposition of Zn^{2+} at glassy carbon electrodes, presented in chapter 6 and, apart from an extra peak associated with the reduction of an intermediate, similar behaviour was observed. Thus it was concluded that the fabrication of zinc microdisk electrodes *via* the method presented above is appropriate for electrochemical applications. The following chapter investigates the reductions of nitrobenzene, bromobenzene and 1-bromo-4-nitrobenzene in the $[C_4mPyrr][NTf_2]$ ionic liquid at platinum microelectrodes, in order to study their reactivities at inert electrodes before utilising the electrodes described in this chapter.

References

1. K. Stulik, C. Amatore, K. Holub, V. Marecek and W. Kutner, *Pure Appl. Chem.*, 2000, 72, 1483-1492.
2. D. R. Lide, *CRC Handbook of Chemistry and Physics*, CRC Press, Taylor & Francis Group, 89 edn., 2008.
3. A. Weidenkaff, A. W. Reller, A. Wokaun and A. Steinfeld, *Thermochimica Acta*, 2000, 359, 69-75.
4. Q. Shi, J. L. J. Rendek, W.-B. Cai and D. A. Scherson, *Electrochemical and Solid-State Letters*, 2003, 6, E35-E39.
5. N. A. Hampson and A. J. S. McNeil, *Journal of Power Sources*, 1985, 15, 245-260.
6. P. F. Maher, A. J. S. McNeil and N. A. Hampson, *Electrochimica Acta*, 1985, 30, 947-960.
7. Y. Meng, L. Aldous, S. R. Belding and R. G. Compton, *Physical Chemistry Chemical Physics*, 2012, 14, 5222-5228.
8. Q. Shi, L. J. Rendek, W.-B. Cai and D. A. Scherson, *Electrochemical and Solid-State Letters*, 2003, 6, E35.
9. M. Cai and S.-M. Park, *Journal of the Electrochemical Society*, 1996, 143, 2125-2131.

8. Reduction of 1-Bromo-4-nitrobenzene at Platinum Microelectrodes: Probing Altered Reactivity in Room-Temperature Ionic Liquids

This chapter primarily describes the electrochemical reduction of 1-bromo-4-nitrobenzene (*p*-$BrC_6H_4NO_2$) at platinum microelectrodes in the *N*-butyl-*N*-methylpyrrolidinium bis(trifluoromethylsulfonyl)imide ([C_4mPyrr][NTf_2]) ionic liquid, in order to probe the reactivity of *p*-$BrC_6H_4NO_2$. The reductions of nitrobenzene ($C_6H_5NO_2$) and bromobenzene (C_6H_5Br) are also investigated to better understand the mechanism of *p*-$BrC_6H_4NO_2$ reduction. Radical anions of 1-bromo-4-nitrobenzene are shown to be reactive in the [C_4mPyrr][NTf_2] room temperature ionic liquid by means of voltammetric measurements. In particular, they are shown to react *via* a DISP type mechanism such that the electrolysis of *p*-$BrC_6H_4NO_2$ occurs consuming between one and two electrons per reactant molecule, leading to the formation of the nitrobenzene radical anion and bromide ions. This behaviour is a stark contrast to that in conventional non-aqueous solvents such as acetonitrile, dimethyl sulfoxide or *N,N*-dimethylformamide, which suggests that the ionic solvent promotes the reactivity of the radical anion, probably *via* the stabilisation of the charged products. The work presented in this chapter has been published in *Physical Chemistry Chemical Physics*[1].

8.1 Introduction

Room-temperature ionic liquids show significantly changed properties in comparison to conventional, molecular, non-aqueous solvents in terms of physical

properties[2] tuneability[3, 4], greenness[5], recyclability[6] and negligible room temperature volatility[7]. Accordingly, they have been increasingly adopted in synthetic procedures ranging from laboratory benchtops to scaled up industrial reactions[8]. On the other hand, the measurement of physiochemical reaction parameters, both kinetic and thermodynamic, has lagged significantly[9].

The use of voltammetry as a ready means of obtaining quantitative data on a variety of processes in RTILs has been demonstrated previously[9]. In the following, this approach is developed to probe changed solute reactivity between RTIL solvents and conventional, molecular, aprotic solvents such as acetonitrile, dimethyl sulfoxide, *N,N*-dimethylformamide, etc. In particular, cyclic voltammetry can easily fingerprint a stable species generated electrochemically so this approach is well-suited for identifying changed reactivity between these different solvent systems. Specifically, species which are reactive in RTILs but are (at least kinetically) stable in conventional media are of interest.

The area of radical ion (both cation and anion) chemistry is well-explored voltammetrically in conventional solvents[9-18]. Such measurements show that, for example, the radical anion of nitrobenzene, $C_6H_5NO_2^{\bullet-}$, is stable both in ionic liquid media[19] and in aprotic molecular solvents[20-22]. Complementary to the electrochemical data, electron spin resonance (ESR) confirms the formation of a persistent radical anion species[23, 24]. Similarly, nitrotoluene radical anions are also seen to be generally stable[25]. On the other hand, the introduction of halogen substituents onto the nitrobenzene ring can have different effects. Introduction of

an iodine substituent leads to radical ions which are usually reactive, whereas chlorinated species are much more stable[26, 27]. In the case of the bromo-nitrobenzenes, the radical anion stability depends on the site of the substituent with respect to the ortho-, meta- or para- positions[26-28]. However, 1-bromo-4-nitrobenzene (*p*-$BrC_6H_5NO_2$) radical anions are stable in acetonitrile, dimethyl sulfoxide and *N,N*-dimethylformamide[20-22]. In the following, the voltammetry of *p*-$BrC_6H_5NO_2$ in the $[C_4mPyrr][NTf_2]$ ionic liquid is investigated and it is shown that, in contrast, it undergoes reduction leading to debromination and the loss of Br^- with the formation of the radical anion of nitrobenzene via a DISP-type mechanism, with the reaction occurring on the timescale of seconds.

8.2 Experimental

Electrochemical measurements were performed in a thermostated (25.0 ± 0.1 °C) Faraday cage, using a μAutolab Type III computer-controlled potentiostat (Ecochemie). All measurements were obtained using a standard three electrode configuration, utilising platinum (Pt, $r \approx 5$ μm, BASi) working electrodes, a platinum wire (99.9%, Goodfellow) counter electrode and a Ag/Ag^+ reference electrode (see below). Prior to use the working electrode was polished using 1, 0.3 and 0.05 μm alumina lapping compounds (Buehler) on soft lapping pads (Buehler) before being placed in deionised water (resistivity ~ 18.2 MΩ cm at 25 °C, Millipore water systems) in an ultrasonic bath for ~3 minutes to remove any adsorbed material. The working electrode was then rinsed thoroughly with MeCN

and dried using compressed nitrogen. Before use, the counter electrode was cleaned in a hot Bunsen flame before being rinsed thoroughly with MeCN.

Electrode radii were calibrated by measuring chronoamperometric transients in a 2 mM solution of ferrocene in MeCN and then fitting the transients using the Shoup-Szabo approximation[29] and the literature value of 2.3×10^{-9} m^2 s^{-1} for the diffusion coefficient of Fc[30]. Transients measured in $[C_4mPyrr][NTf_2]$ were obtained by first holding the potential at -1.0 V for 5 s and then stepping to a potential of -2.0 V and recording the current response for 5 s, using a sample time of 0.01 s.

The Ag/Ag^+ reference electrode was prepared following a modified version of the method of Meng et al.[31] which involved attaching a 5Å, 1.6mm diameter molecular sieve to the end of a cut-down glass Pasteur pipette using PTFE heatshrink. The Ag/Ag^+ reference electrode was then filled with a 20 mM solution of Ag[OTf] in $[C_4mPyrr][NTf_2]$ and a silver wire was immersed in the solution. Experiments were prepared by placing 50 μL of solution into a chamber on top of the electrode, placing under vacuum for at least 2 hours before measurement, and remained *in-vacuo* for the duration of the experiment. Cyclic voltammograms (CVs) were background-subtracted (using a linear baseline) and filtered using an FFT function to remove high frequency electrical noise Modelling of voltammetric data was carried out using software described elsewhere[9].

8.3 Results and Discussion

In order to better understand and simulate the reduction of *p*-$BrC_6H_4NO_2$ in the $[C_4mPyrr][NTf_2]$ ionic liquid, the electrochemical reductions of $C_6H_5NO_2$ and C_6H_5Br in $[C_4mPyrr][NTf_2]$ are first presented.

Electrochemical reduction of nitrobenzene in $[C_4mPyrr][NTf_2]$

A 15.9 mM solution of $C_6H_5NO_2$ in $[C_4mPyrr][NTf_2]$ was placed under vacuum to remove oxygen and water, which interfere with electrochemical experiments in RTILs[32, 33]. Cyclic voltammograms (CVs) were then recorded for the reduction of nitrobenzene in the $[C_4mPyrr][NTf_2]$ ionic liquid.

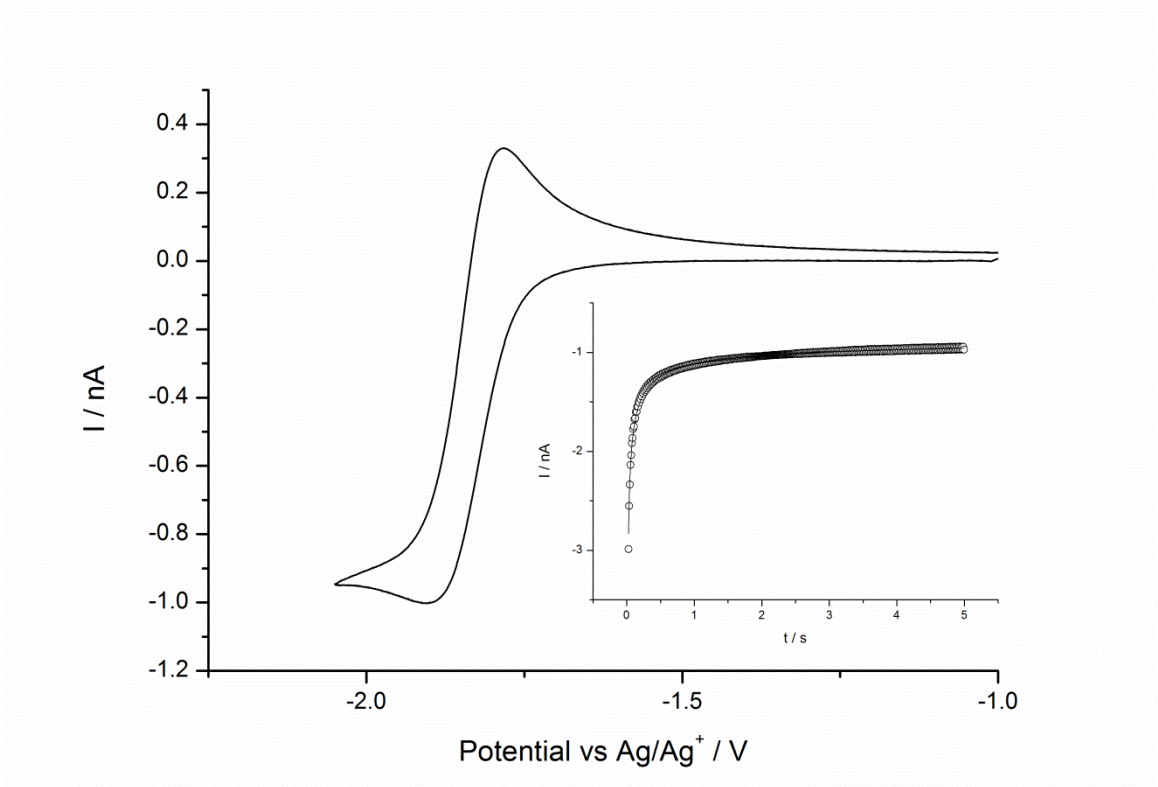


Figure 25 - Cyclic voltammogram of 15.9 mM $C_6H_5NO_2$ in $[C_4mPyrr][NTf_2]$ at a Pt microdisk (radius = 5.1 μm) at a scan rate of 100 mV s^{-1}. Inset: Chronoamperometric transients for the reduction of 15.9 mM $C_6H_5NO_2$ in $[C_4mPyrr][NTf_2]$ at a Pt microdisk (radius = 5.4 μm), showing the experimental data (circles) and Shoup-Szabo fit (line).

8. Reduction of 1-Bromo-4-nitrobenzene at Platinum Microelectrodes

Figure 25 shows a CV of 15.9 mM nitrobenzene in $[C_4mPyrr][NTf_2]$, recorded at a scan rate of 100 mV s^{-1}, where the potential was scanned between -1 and -2.05 V. The CV shows single reduction and oxidation peaks at -1.91 and -1.78 V *vs.* the Ag/Ag^+ reference, respectively.

Chronoamperometric transients were then recorded for the reduction of nitrobenzene and the experimental data was fitted using the Shoup-Szabo approximation[29] to simultaneously determine the diffusion coefficient, D, and the number of electrons, n, transferred in the reduction. Figure 25 (inset) shows a typical chronoamperogram for the reduction of the 15.9 mM $C_6H_5NO_2$ solution.

As the radius of the electrode and the initial concentration of the solution were known, fitting *via* the Shoup-Szabo expression allows for the simultaneous determination of D and nc. Chronoamperometric transients measured at ~10 minute intervals showed that nc was found to decrease with time under vacuum as the compound was slowly removed from solution, however, a diffusion coefficient of $(3.4 \pm 0.1) \times 10^{-11}$ m^2 s^{-1} was reproducibly obtained, showing that D is independent of concentration. Plotting nc *vs.* t then allowed for the extrapolation of nc to $t = 0$, where $c = c_0$, and thus n was determined as approximately equal to one, which suggests that the electrode process is;

$$C_6H_5NO_2 + e^- \rightleftharpoons C_6H_5NO_2^{\bullet -} \qquad (8.1)$$

where the stability of the radical anion is suggested by the pronounced backpeak in Figure 25.

8. Reduction of 1-Bromo-4-nitrobenzene at Platinum Microelectrodes

In order to confirm that $n = 1$, CVs were simulated as a single electron transfer, as suggested by the chronoamperometric data. The value for the electron transfer coefficient, α, was calculated, *via* Tafel analysis[34, 35] of the voltammetry, to be 0.63 ± 0.03 and this value was incorporated in the model, along with the value for $D(C_6H_5NO_2)$ of 3.4 × 10^{-11} m^2 s^{-1} determined *via* chronoamperometry. The concentration of the solution at the time that the voltammetry was measured could be estimated from the chronoamperometric data and thus these values were also incorporated into the simulation. The voltammetry was initially simulated with $D(C_6H_5NO_2^{\bullet-}) = D(C_6H_5NO_2)$, however the simulated backpeaks did not match the experimental voltammetry. Given that the diffusion coefficients of charged species have been shown to significantly differ from their neutral counterparts in RTILs in many cases[2], $D(C_6H_5NO_2^{\bullet-})$ was then considered as a fitting parameter. The fitting parameters were thus the anion radical diffusion coefficient, $D(C_6H_5NO_2^{\bullet-}) = (1.1 \pm 0.1) \times 10^{-11}$ m^2 s^{-1}, the heterogeneous rate constant, $k_0 = (7 \pm 1) \times 10^{-5}$ m s^{-1}, and the formal potential, $E_0 = -1.81 \pm 0.01$ V. Figure 26 shows a comparison between the experimental and simulated voltammetry at 10 and 100 mV s^{-1} scan rates. As shown in Figure 26, the experimental data is well simulated as a one-electron reduction using the values obtained via chronoamperometry and Tafel analysis as a starting point. The reduction was thus assigned as the one electron reduction of nitrobenzene to its radical anion, as has been previously shown for nitrobenzene in a range of aprotic solvents[20, 36, 37] and in the ionic liquid 1-butyl-2,3-dimethylimidazolium

bis(trifluoromethylsulfonyl)imide, $[C_4dmim][NTf_2]$[19]. The fitting parameters used in the simulation of $C_6H_5NO_2$ are used below for the interpretation of the voltammetry of *p*-$BrC_6H_4NO_2$.

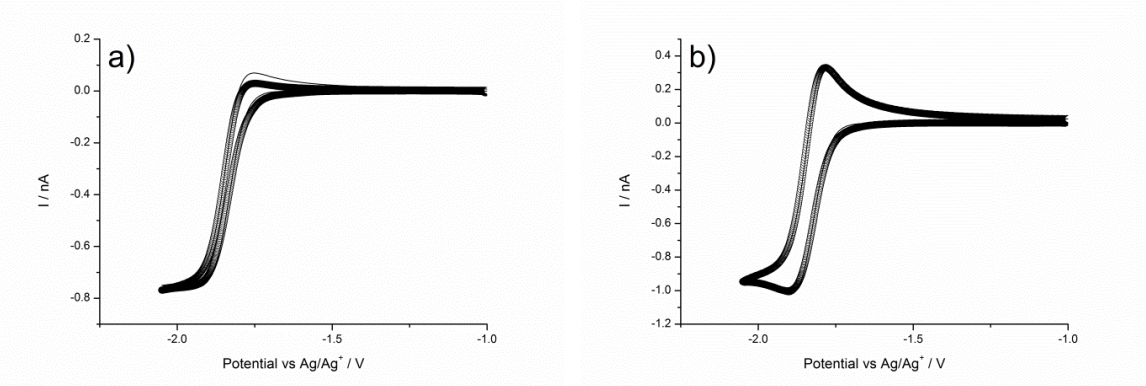


Figure 26 - Comparison of experimental (circles) and simulated (lines) data for scan rates of a) 10 mV s^{-1} and b) 100 mV s^{-1}.

Electrochemical reduction of bromobenzene in $[C_4mPyrr][NTf_2]$

A 12.8 mM solution of C_6H_5Br in [C4mPyrr][NTf2] was then placed under vacuum and investigated *via* cyclic voltammetry. However, no Faradaic features were visible in the resulting voltammetry. This was rationalised as the result of fast loss of material from the solution phase into the gas phase, given the larger vapour pressure and lower boiling point reported for C_6H_5Br than for $C_6H_5NO_2$. The vapour pressure at 25°C and the boiling point at atmospheric pressure of nitrobenzene are 0.274 Torr (0.365 mbar) and 210.8 ± 0.0 °C, respectively, while for bromobenzene these values are 4.12 (5.49 mbar)Torr and 154.2 ± 9.0 °C, respectively (Calculated using Advanced Chemistry Development (ACD/Labs) Software V11.02 (© 1994-2013 ACD/Labs), *via* Scifinder). Therefore, in order to measure the *qualitative* voltammetry of C_6H_5Br, solutions of much higher

concentration were investigated so that a small amount of material remained in solution for voltammetric study, albeit of unknown concentration. Figure 27 shows the electrochemical reduction of 0.95 M C_6H_5Br in $[C_4mPyrr][NTf_2]$.

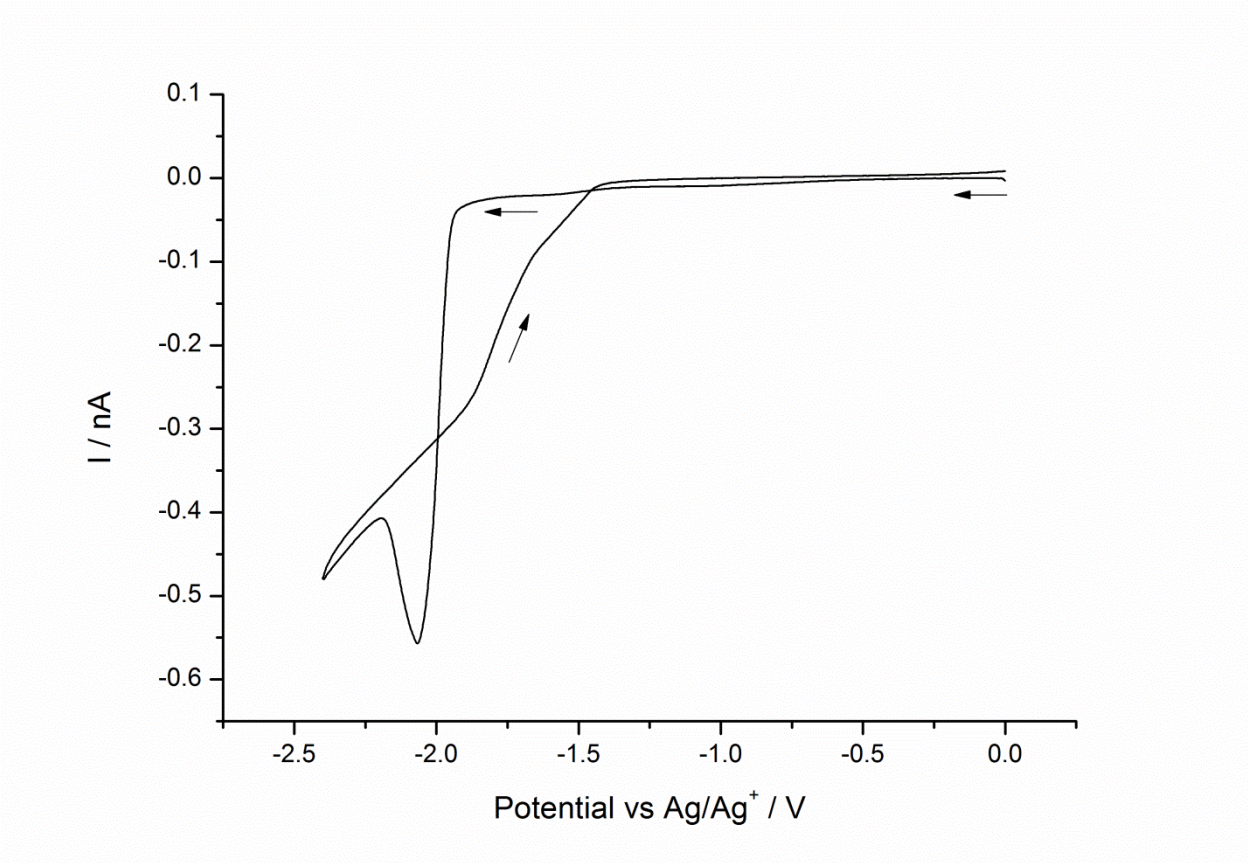


Figure 27 - Cyclic voltammetry of 0.95 M C_6H_5Br in $[C_4mPyrr][NTf_2]$ at a Pt microdisk (radius = 5.4 μm) at a scan rate of 10 mV s^{-1}.

Apparent in Figure 27 is a single reduction peak at -2.07 V with no accompanying backpeak, as well as a crossover in the forward and reverse sweep currents indicative of a change of the electrode surface. Furthermore, the reductive wave diminishes and shifts to more negative potentials on successive scans until the signal is no longer detectable. These observations together then imply a modification of the surface[38]. Due to this surface fouling, no further

experiments were performed using the C_6H_5Br compound. Nevertheless, the potentials at which there is an onset of C_6H_5Br reduction were noted as being significantly more negative than for nitrobenzene. This is important in rationalising the reduction of *p*-$BrC_6H_5NO_2$, which is presented below.

Electrochemical reduction of 1-bromo-4-nitrobenzene in [C_4mPyrr][NTf_2]

After studying the electrochemistry of $C_6H_5NO_2$ and C_6H_5Br in the [C_4mPyrr][NTf_2] ionic liquid, the voltammetry of *p*-$BrC_6H_4NO_2$ was investigated. Figure 28 shows the cyclic voltammetry of a 5.4 mM solution of *p*-$BrC_6H_4NO_2$ in the [C_4mPyrr][NTf_2] ionic liquid at a scan rate of 100 mV s^{-1}.

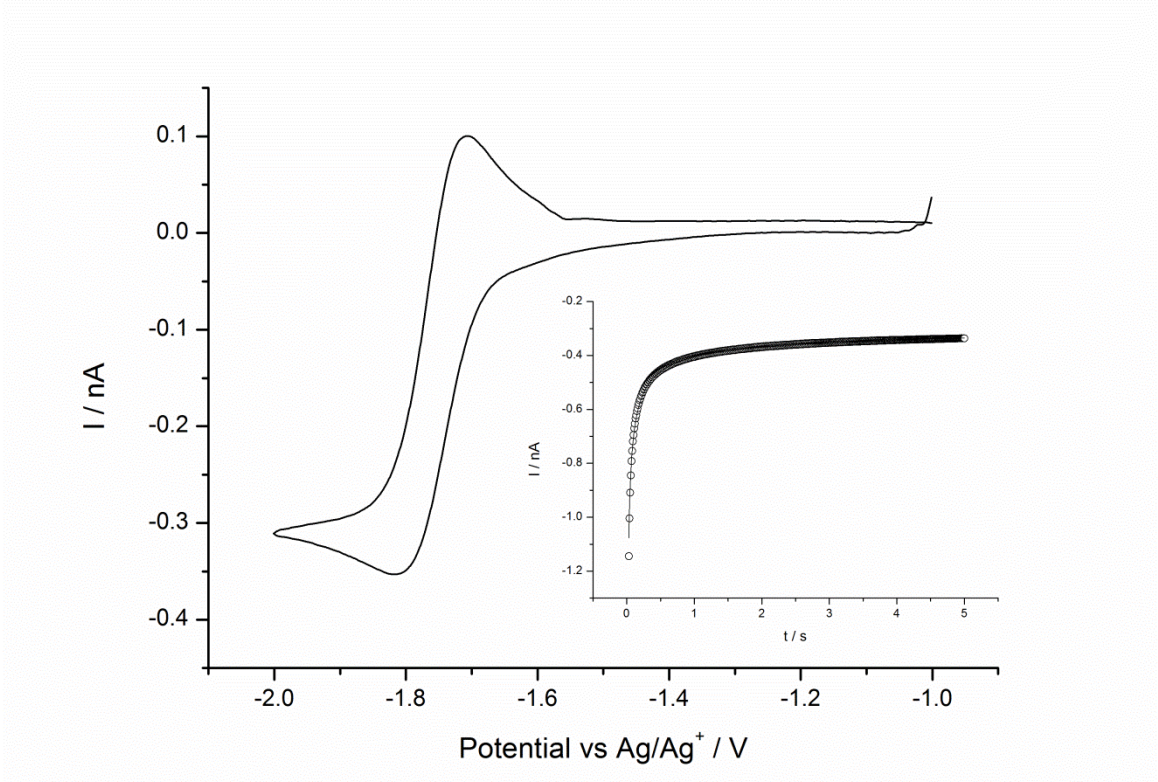


Figure 28 - Cyclic voltammetry of 5.4 mM *p*-$BrC_6H_4NO_2$ in [C_4mPyrr][NTf_2] at a Pt microdisk (radius = 5.0 μm) at a scan rate of 100 mV s^{-1}. Inset: Chronoamperogram for the reduction of 5.4 mM *p*-$BrC_6H_4NO_2$ in [C_4mPyrr][NTf_2] at a Pt microdisk (radius = 5.0 μm), showing the experimental (circles) and Shoup-Szabo fitted (line) transients.

8. Reduction of 1-Bromo-4-nitrobenzene at Platinum Microelectrodes

Figure 28 shows that the reduction and oxidation peaks occur at -1.8 and -1.7 V, respectively. Also evident in the voltammetry is a shoulder on the reduction wave and a sharper than expected current decrease after the oxidation peak. This behaviour at potentials positive of the redox couple is likely caused by an adsorption/desorption type process[35]. CVs were then recorded at a range of scan rates between 5 and 1000 mV s^{-1}, as shown in Figure 29.

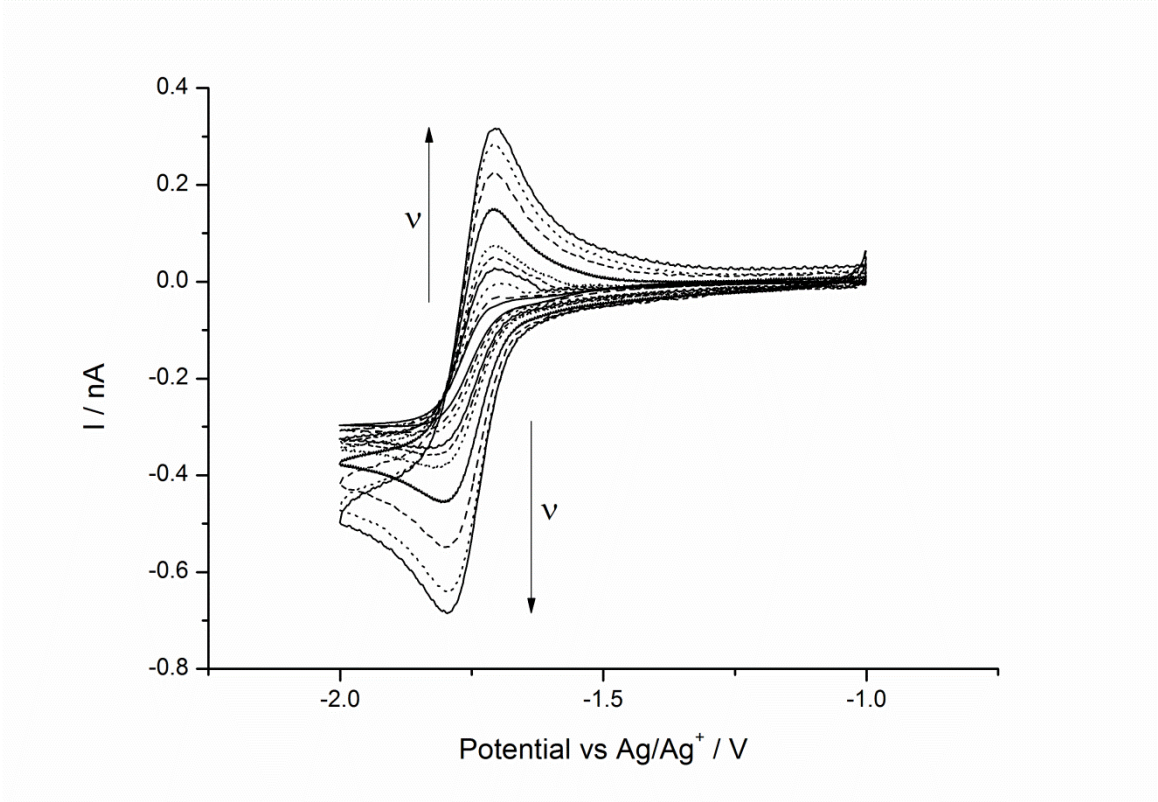


Figure 29 - Cyclic voltammetry of 5.4 mM *p*-$BrC_6H_4NO_2$ in [C_4mPyrr][NTf_2] at a Pt microdisk (radius = 5.0 μm) at scan rates of 5, 10, 25, 50, 75, 100, 250, 500, 750 and 1000 mV s^{-1}.

Figure 29 shows the effects of scan rate, v, on the voltammetry of *p*-$BrC_6H_4NO_2$ in the [C_4mPyrr][NTf_2] ionic liquid. It is apparent from the figure that as the scan rate is increased the voltammetry becomes increasingly well-defined. This indicates that the reduction wave shoulder and faster than expected current decay

after the backpeak are likely caused by a combination of adsorption/desorption, as at faster scan rates these processes are relatively outrun.

Chronoamperometric transients were then measured for the reduction of *p*-$BrC_6H_4NO_2$ and the experimental data was fitted using the Shoup-Szabo approximation to simultaneously determine the diffusion coefficient and the number of electrons transferred in the reduction. Figure 28 (inset) shows a typical chronoamperogram for the reduction of 5.4 mM *p*-$BrC_6H_4NO_2$.

As described in Chapter 1 and elsewhere[29, 39], fitting the experimental transient *via* the Shoup-Szabo approximation allows for the simultaneous determination of D and nc. Analogous to the experimental procedure for $C_6H_5NO_2$, long timescale chronoamperometric transients were measured at ~10 minute intervals and each transient was independently fitted using the Shoup-Szabo approximation. The fitting of transients with short measurement times did not yield reproducible results and hence transients were measured for 5 s. The fitting of transients with long measurement times then yielded a reproducible diffusion coefficient of $(1.8 \pm 0.1) \times 10^{-11}$ m^2 s^{-1}, while nc was again found to decrease with time under vacuum. Extrapolation of the nc *vs.* t data to overcome issues relating to solute volatility, as for $C_6H_5NO_2$, allowed for the determination of nc at $t = 0$, showing that, for *p*-$BrC_6H_5NO_2$, n was between one and two.

In order to determine the mechanism for the reduction of *p*-$BrC_6H_4NO_2$, it was necessary to simulate the voltammetric data. Initially, the voltammetry was simulated as a one-electron reduction, as for nitrobenzene, however, the one-

electron model was found to be insufficient in fitting the experimental data. The experimental data was then simulated assuming a pure two-electron reduction, however, the simulated voltammograms were again unable to describe the data and it was evident that a more complicated mechanism was involved. Plotting the log of the peak currents, $\log(I_p)$, *vs.* the log of the scan rate, $\log(v)$, for the experimental voltammetry and for the one- and two-electron simulations allows comparison of the experimental peak currents with the working curves for both mechanisms.

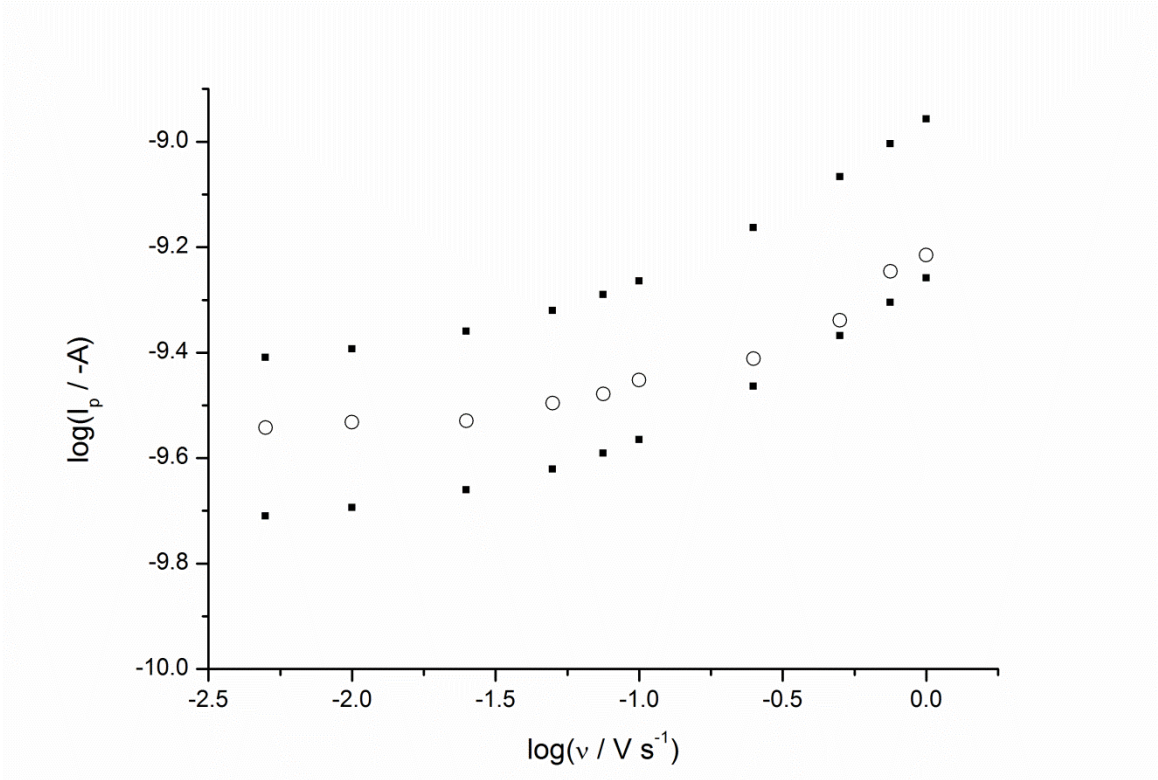


Figure 30 - Comparison of the experimentally determined peak currents (circles) with those simulated using one-electron (lower squares) and two-electron (upper squares) models, with scan rate. The scan rates shown are 5, 10, 25, 50, 75, 100, 250, 500, 750 and 1000 mV s^{-1}.

This is demonstrated in Figure 30, which shows the experimentally obtained peak currents varying between the two limiting cases, of one-electron and two-electron reduction, with scan rate. This indicates that a chemical step may be involved in the reaction scheme and also justifies why the short time chronoamperometric transients were unable to yield a reproducible diffusion coefficient when fitted with the Shoup-Szabo approximation.

The variation of the experimental peak current between the one electron and simple two-electron limits, shown in Figure 30, suggests that either an ECE or DISP type mechanism is occurring. The generalised ECE mechanism for a reduction is represented as follows;

$$A + e^- \rightleftharpoons B \tag{8.2}$$

$$B \rightarrow C \tag{8.3}$$

$$C + e^- \rightleftharpoons D \tag{8.4}$$

The two generalised DISP mechanisms for the case of a reduction are then represented by;

$$A + e^- \rightleftharpoons B \tag{8.5}$$

$$B \rightarrow C \tag{8.6}$$

$$B + C \rightarrow A + D \tag{8.7}$$

where the distinction between DISP1 and DISP2 depends on which of the two homogeneous steps are rate determining. If (8.6) is rate determining the mechanism is DISP1, while if (8.7) is the rate determining step, the mechanism is

DISP2. The DISP2 case can be distinguished voltammetrically as the forward peak potential shows a concentration dependence as well as a scan rate dependence of ~20 mV decades, compared to the ~30 mV decades observed for both ECE and DISP1 processes[35]. The ECE and DISP1 schemes are often difficult to differentiate between voltammetrically when the second electron transfer is highly driven, as both have a chemical step which is rate-determining and show the same dependence of peak potential with scan rate[35].

The experimental voltammetry was then simulated using both ECE and DISP1 schemes. The mechanisms assumed for the ECE and DISP1 reduction of *p*-$BrC_6H_4NO_2$ in the $[C_4mPyrr][NTf_2]$ ionic liquid are shown below.

$$p\text{-}BrC_6H_4NO_2 + e^- \rightleftharpoons \left[p\text{-}BrC_6H_4NO_2\right]^{\bullet -} \tag{8.8}$$

$$\left[p\text{-}BrC_6H_4NO_2\right]^{\bullet -} + HS \xrightarrow{\text{slow}} C_6H_5NO_2 + S^{\bullet} + Br^- \tag{8.9}$$

$$C_6H_5NO_2 + e^- \rightleftharpoons C_6H_5NO_2^{\bullet -} \tag{8.10}$$

where HS refers to the solvent system. For the DISP1 mechanism, step (8.10) is replaced with;

$$\left[p\text{-}BrC_6H_4NO_2\right]^{\bullet -} + C_6H_5NO_2 \overset{\text{fast}}{\rightleftharpoons} p\text{-}BrC_6H_4NO_2 + C_6H_5NO_2^{\bullet -} \tag{8.11}$$

Note that reaction (8.11) is fully driven in the pure DISP1 case, whereas in the present system under study the reaction will be in equilibrium with both reactants and products present because $C_6H_5NO_2$ and *p*-$BrC_6H_4NO_2$ have clearly similar reduction potentials. The fitting parameters used to simulate the

experimental voltammetry *via* the ECE and DISP1 mechanisms shown above are presented in Table 6 and Table 7, respectively, where the values D, c_0, E_0, k_0, k_f and α refer to the diffusion coefficients, initial concentrations, formal potentials, heterogeneous rate constants, homogeneous rate constants and electron transfer coefficients, respectively, for steps involving the species *p*-$BrC_6H_4NO_2$, $[p\text{-}BrC_6H_4NO_2]^{\bullet-}$, $C_6H_5NO_2$ and $C_6H_5NO_2^{\bullet-}$. The parameter $k_f(1)$ represents a pseudo-first order rate constant for the chemical step, as the solvent is present in large excess.

Simulations for the ECE and DISP1 reduction of *p*-$BrC_6H_4NO_2$ were constructed such that the simulated diffusion coefficients for *p*-$BrC_6H_4NO_2$ and $C_6H_5NO_2$ were those obtained from the Shoup-Szabo fitting of long time chronoamperometric transients and the parameters for the 2nd heterogeneous step of the ECE mechanism were the same as those determined *via* the one-electron simulation of $C_6H_5NO_2$. As a complex adsorption/desorption mechanism was clearly influencing the experimental voltammetry, simulations were limited to the fitting of the forward scan. A comparison of experimental peak currents to those simulated using the ECE mechanism is presented in Figure 31. It is evident that the simulated peak currents are not too dissimilar from those obtained from experimental voltammetry, however, the fact that the second electron transfer is not highly driven, leading to slightly split-wave behaviour, would seem to indicate that an ECE mechanism is ill-suited to describe the electrochemical reduction of *p*-$BrC_6H_4NO_2$ in $[C_4mPyrr][NTf_2]$.

Table 6 - Parameters employed in the ECE simulation of *p*-$BrC_6H_4NO_2$ voltammetry.

Chemical Species	*p*-$BrC_6H_5NO_2$	[*p*-$BrC_6H_5NO_2$]$^{\bullet-}$	$C_6H_5NO_2$	$C_6H_5NO_2^{\bullet-}$
D / m^2 s^{-1}	$(1.8\pm0.1)\times10^{-11}$	$(5.0\pm0.5)\times10^{-12}$	$(3.4\pm0.1)\times10^{-11}$	$(1.1\pm0.1)\times10^{-11}$
c_{bulk} / mM	5.4±0.5	0	0	0

Homogeneous reactions	$k_f(1)$ / s^{-1}
B +HS → C	1.0±0.1

Heterogeneous reactions	E_0 / V	k_0 / m s^{-1}	α
A + e$^-$ → B	-1.74±0.01	$>1\times10^{-3}$ *	0.5±0.1
C + e$^-$ → D	-1.81±0.01	$(7\pm1)\times10^{-5}$	0.63±0.03

* Not rate determining.

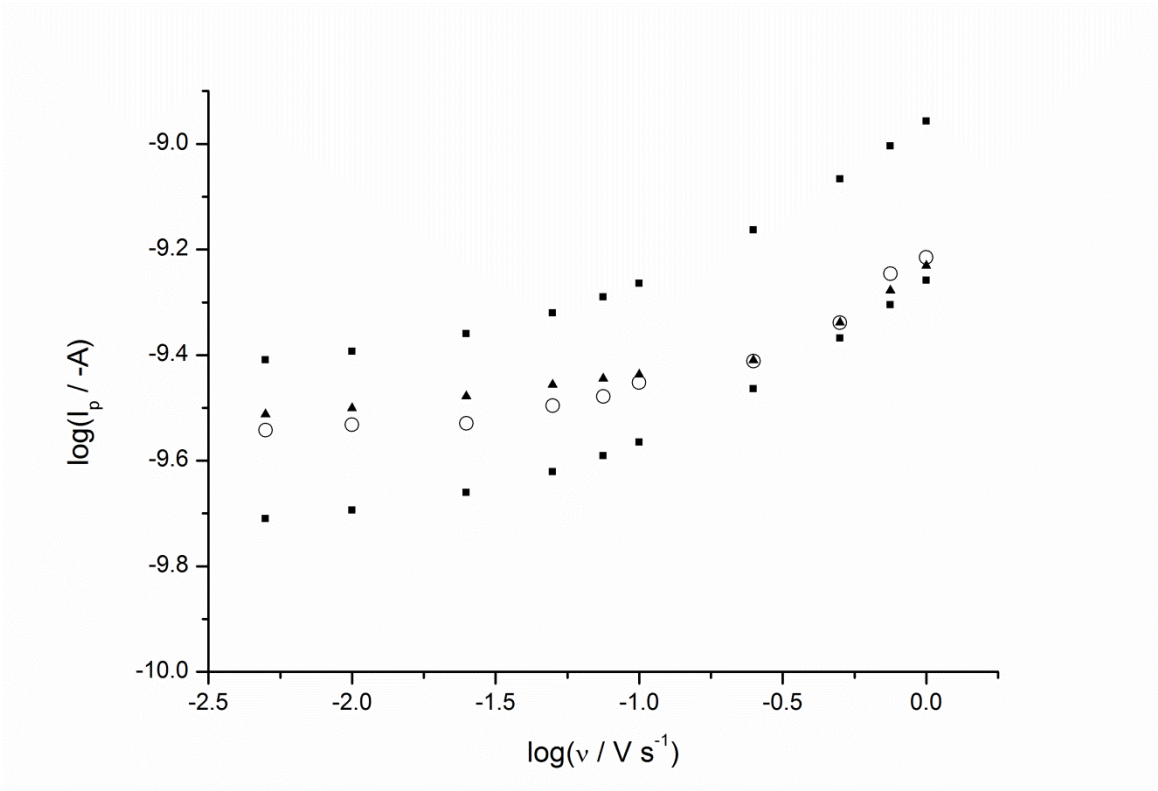


Figure 31 - Comparison of reduction peak currents obtained from experiment (circles) and from ECE simulations (triangles) as well as for the two limiting cases of one-electron (lower squares) and two-electron (upper squares) reductions.

It is also important to note that the experimental peak currents yield a less well-defined working curve due to a steady decrease in concentration over the timescale of the scan rate dependence study. The order of the scan rates studied was random, to avoid the concentration drop adding to the scan rate dependency, in the order 10, 100, 5, 750, 50, 250, 75, 500, 25 and 1000 mV s^{-1}, respectively. The experimental voltammetry was then simulated using the DISP1 mechanism and the comparisons between experimental and simulated peak currents are shown in Figure 32.

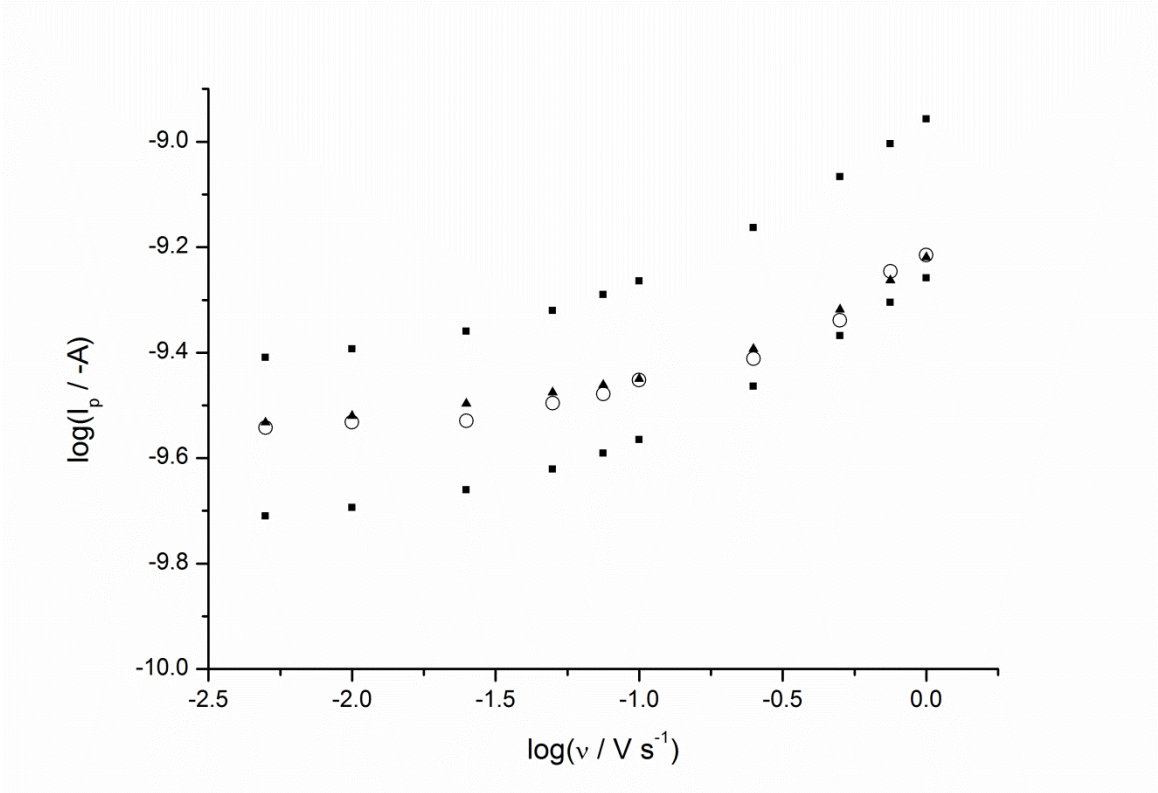


Figure 32 - Comparison of reduction peak currents obtained from experiment (circles) and from DISP1 simulations (triangles) as well as for the two limiting cases of one-electron (lower squares) and two-electron (upper squares) reductions.

Table 7 - Parameters employed in the DISP1 simulation of p-$BrC_6H_4NO_2$ voltammetry.

Chemical Species	p-$BrC_6H_5NO_2$	$[p\text{-}BrC_6H_5NO_2]^{\bullet-}$	$C_6H_5NO_2$	$C_6H_5NO_2^{\bullet-}$
D / $m^2\ s^{-1}$	$(1.8\pm0.1)\times10^{-11}$	$(5.0\pm0.5)\times10^{-12}$	$(3.4\pm0.1)\times10^{-11}$	$(1.1\pm0.1)\times10^{-11}$
c_{bulk} / mM	5.4±0.5	0	0	0
Homogeneous reactions	$k_f(1)$ / s^{-1}	$k_f(2)$ / $m^3\ mol^{-1}\ s^{-1}$		
B +HS → C	1.0±0.1			
B + C → A + D		$>1\times10^{10}$ *		
Heterogeneous reactions	E_0 / V	k_0 / m s^{-1}	α	
A + e^- → B	-1.74±0.01	$>1\times10^{-3}$ *	0.5±0.1	

* Not rate determining.

As shown in Figure 32, the data simulated *via* the DISP1 mechanism describes the experimental peak currents to a larger extent than the voltammetry simulated *via* the ECE mechanism. As such, the electrochemical reduction of p-$BrC_6H_5NO_2$ in the $[C_4mPyrr][NTf_2]$ ionic liquid appears to occur *via* a DISP1 mechanism, with simulations describing the experimental data well given the large parameter-space inherent in the simulation of multi-step mechanisms.

It is of interest to compare the voltammetry of p-$BrC_6H_4NO_2$ in $[C_4mPyrr][NTf_2]$ with that reported for the photo-electrochemical reduction of p-$BrC_6H_4NO_2$ in MeCN[22-24, 27]. The studies in MeCN showed that, in the absence of light, p-$BrC_6H_4NO_2$ was reduced via an electrochemically reversible one-electron reduction and that the resulting anion radical had a lifetime of at least 10 s[23]. Furthermore, irradiation of the system with light corresponding to absorption

bands in the radical anion, led to the observation of significant photocurrents. These photocurrents were shown to be due to the reduction of nitrobenzene after photo-induced dissociation of Br^- from the anion radical followed by hydrogen abstraction from the solvent[24]. In light of these results, the present voltammetry, which was recorded in the absence of light inside a Faraday cage, is all the more interesting as it shows that the *p*-$BrC_6H_4NO_2$ molecule has an altered reactivity in the $[C_4mPyrr][NTf_2]$ ionic liquid, compared to MeCN. The most obvious explanation for this enhanced reactivity is that the ionic nature of the RTIL allows for much better solvation and stabilisation of the bromide anion and $C_6H_5NO_2$ radical anion as compared to the solvation by MeCN because possible counter-ions are present in much higher concentration than the supporting electrolyte in MeCN. Furthermore, the bromide anion can be envisaged to coordinate much more strongly with the pyrrolidinium cation than the sterically hindered bis(trifluoromethylsulfonyl)imide anion, as corroborated by examining the melting points of $[C_4mPyrr][NTf_2]$ and $[C_4mPyrr]Br$, which are 186 K[40] and 490 K[41], respectively. It has thus been demonstrated in this chapter that the electrochemical reduction of *p*-$BrC_6H_5NO_2$ in the $[C_4mPyrr][NTf_2]$ ionic liquid occurs via a DISP1 mechanism in the absence of light, which illustrates the possibility for enhanced reactivity of the *p*-$BrC_6H_5NO_2$ in the $[C_4mPyrr][NTf_2]$ ionic liquid compared to that in MeCN.

8.4 Conclusions

The reductions of $C_6H_5NO_2$, C_6H_5Br and *p*-$BrC_6H_4NO_2$ were studied in the $[C_4mPyrr][NTf_2]$ ionic liquid *via* cyclic voltammetry, chronoamperometry and voltammetric simulation. $C_6H_5NO_2$ was found to be reduced *via* a one-electron mechanism to form the stable radical anion, analogous to the behaviour in a range of aprotic solvents and the $[C_4dmim][NTf_2]$ RTIL. The reduction of C_6H_5Br was found to occur at potentials negative to those of $C_6H_5NO_2$ and multiple scans were found to modify the electrode surface. The reduction of *p*-$BrC_6H_4NO_2$ was then examined experimentally and *via* voltammetric simulations employing the analysis of the reductions of $C_6H_5NO_2$ and C_6H_5Br. It was shown that reduction proceeds *via* a DISP type mechanism in which the parent molecule is reduced by one electron to form the anion radical, at which point debromination occurs in a rate-determining chemical step, with the fast scavenging of a hydrogen atom from the solvent system, to yield nitrobenzene, which is then reduced to its radical anion. This shows significant contrast to the behaviour observed in aprotic solvents as the debromination was observed in the absence of light. Thus, it was shown that the *p*-$BrC_6H_4NO_2$ radical anion exhibits a changed reactivity in the $[C_4mPyrr][NTf_2]$ ionic liquid compared to molecular non-aqueous solvents, which was rationalised in terms of much better solvation and stabilisation of Br^- in the RTIL, as coordination with the RTIL cation is highly favoured. The following chapter now investigates the electrochemical reduction of *p*-$BrC_6H_4NO_2$ in the $[C_4mPyrr][NTf_2]$ RTIL at zinc microelectrodes, which were described in Chapter 7.

References

1. S. Ernst, K. R. Ward, S. E. Norman, C. Hardacre and R. G. Compton, *Physical Chemistry Chemical Physics*, 2013, 15, 6382-6389.
2. D. S. Silvester and R. G. Compton, *Zeitschrift für Physikalische Chemie*, 2006, 220, 1247-1274.
3. J. D. Holbrey and K. R. Seddon, *Journal of the Chemical Society - Dalton Transactions*, 1999, 2133-2139.
4. L. Xiong, A. M. Fletcher, S. G. Davies, S. E. Norman, C. Hardacre and R. G. Compton, *Chem. Commun. (Cambridge, U. K.)*, 2012, 48, 5784-5786.
5. M. J. Earle and K. R. Seddon, *Pure and Applied Chemistry*, 2000, 72, 1391-1398.
6. Z.-L. Shen, S.-J. Ji and T.-P. Loh, *Tetrahedron Letters*, 2005, 46, 3137-3139.
7. M. J. Earle, J. M. S. S. Esperança, M. A. Gilea, J. N. C. Lopes, L. P. N. Rebelo, J. W. Magee, K. R. Seddon and J. A. Widegren, *Nature*, 2006, 439, 831-834.
8. N. V. Plechkova and K. R. Seddon, *Chemical Society Reviews*, 2008, 37, 123-150.
9. E. O. Barnes, A. M. O'Mahony, S. R. Belding and R. G. Compton, *Journal of Chemical & Engineering Data*, 2009, 55, 2219-2224.
10. J.-M. Savéant, *Tetrahedron*, 1994, 50, 10117-10165.
11. J. M. Savéant, *Acc. Chem. Res.*, 1993, 26, 455-461.
12. L. Dunsch, *Zeitschrift für Chemie*, 1974, 14, 463-468.
13. J. Heinze, *Angewandte Chemie*, 1984, 96, 823-840.
14. M. V. B. Zanoni, E. I. Rogers, C. Hardacre and R. G. Compton, *Int. J. Electrochem. Sci.*, 2009, 4, 1607-1627.
15. V. A. Nikitina, R. R. Nazmutdinov and G. A. Tsirlina, *J. Phys. Chem. B*, 2011, 115, 668-677.
16. A. P. Doherty and C. A. Brooks, *ACS Symp. Ser.*, 2003, 856, 410-420.
17. J. Heinze, *Angewandte Chemie*, 1993, 105, 1327-1349.
18. G. Zeppenfeld, M. Stephan, L. Dunsch and H. G. Döge, *Acta Polymerica*, 1979, 30, 664-669.

19. D. S. Silvester, A. J. Wain, L. Aldous, C. Hardacre and R. G. Compton, *Journal of Electroanalytical Chemistry*, 2006, 596, 131-140.
20. W. Kemula and R. Sioda, *Bull. Acad. Pol. Sci., Ser. Sci. Chim.*, 1962, 10, 507-512.
21. J. G. Lawless and M. D. Hawley, *Journal of Electroanalytical Chemistry and Interfacial Electrochemistry*, 1969, 21, 365-375.
22. J. A. Cooper and R. G. Compton, *Electroanalysis*, 1998, 10, 1182-1187.
23. R. G. Compton, R. A. W. Dryfe and A. C. Fisher, *Journal of Electroanalytical Chemistry*, 1993, 361, 275-278.
24. R. G. Compton and R. A. W. Dryfe, *Journal of Electroanalytical Chemistry*, 1994, 375, 247-255.
25. L. Álvarez-Griera, I. Gallardo and G. Guirado, *Electrochimica Acta*, 2009, 54, 5098-5108.
26. R. G. Compton, R. A. W. Dryfe, J. C. Eklund, S. D. Page, J. Hirst, L. Nei, G. W. J. Fleet, K. Y. Hsia, D. Bethell and L. J. Martingale, *Journal of the Chemical Society, Perkin Transactions 2*, 1995, 0, 1673-1677.
27. R. G. Compton, R. A. W. Dryfe and A. C. Fisher, *Journal of the Chemical Society, Perkin Transactions 2*, 1994, 0, 1581-1587.
28. E. O. Barnes, Y. Wang, J. G. Limon-Petersen, S. R. Belding and R. G. Compton, *Journal of Electroanalytical Chemistry*, 2011, 659, 25-35.
29. D. Shoup and A. Szabo, *Journal of Electroanalytical Chemistry and Interfacial Electrochemistry*, 1982, 140, 237-245.
30. M. Sharp, *Electrochimica Acta*, 1983, 28, 301-308.
31. Y. Meng, L. Aldous, S. R. Belding and R. G. Compton, *Physical Chemistry Chemical Physics*, 2012, 14, 5222-5228.
32. C. Zhao, A. M. Bond, R. G. Compton, A. M. O'Mahony and E. I. Rogers, *Analytical Chemistry*, 2010, 82, 3856-3861.
33. A. M. O'Mahony, D. S. Silvester, L. Aldous, C. Hardacre and R. G. Compton, *Journal of Chemical and Engineering Data*, 2008, 53, 2884-2891.
34. J. O. M. Bockris and A. K. N. Reddy, *Modern electrochemistry*, Plenum Press, New York, 1998.
35. R. G. Compton and C. E. Banks, *Understanding voltammetry, 2nd ed.*, World Scientific, Singapore ; London, 2011.

36. P. Zuman and Z. Fijalek, *Journal of Electroanalytical Chemistry*, 1990, 296, 583-588.

37. A. Pelekourtsa, N. Missaelidis and D. Jannakoudakis, *Chim. Chron.*, 1997, 26, 39-48.

38. V. Jouikov and J. Simonet, *Electrochemistry Communications*, 2010, 12, 331-334.

39. L. Xiong, A. M. Fletcher, S. Ernst, S. G. Davies and R. G. Compton, *Analyst*, 2012, 137, 2567-2573.

40. D. R. MacFarlane, P. Meakin, J. Sun, N. Amini and M. Forsyth, *The Journal of Physical Chemistry B*, 1999, 103, 4164-4170.

41. C. Jagadeeswara Rao, K. A. Venkatesan, K. Nagarajan, T. G. Srinivasan and P. R. Vasudeva Rao, *Electrochimica Acta*, 2009, 54, 4718-4725.

9. Reduction of 1-Bromo-4-nitrobenzene at Zinc Microelectrodes: Utilising the Changed Reactivity of 1-Bromo-4-nitrobenzene in RTILs to Form Arylzincs

The previous chapter described the reduction of several functionalised benzenes, including 1-bromo-4-nitrobenzene (*p*-$BrC_6H_4NO_2$), at platinum microelectrodes. This chapter extends the investigation of the electrochemical reduction of *p*-$BrC_6H_4NO_2$ to study the reduction at zinc microelectrodes in the *N*-butyl-*N*-methylpyrrolidinium bis(trifluoromethylsulfonyl)imide ([C_4mPyrr][NTf_2]) ionic liquid *via* cyclic voltammetry. The reduction is found to occur *via* an EC type mechanism, where *p*-$BrC_6H_4NO_2$ is first reduced by one electron, quasi-reversibly, to yield the corresponding radical anion. The radical anions then react with the Zn electrode to form arylzinc products. Introduction of carbon dioxide into the system leads to reaction with the arylzinc species, fingerprinting the formation of the latter. This method thus demonstrates a proof-of-concept of the formation of functionalised arylzinc species. The work presented in this chapter has been published in *Physical Chemistry Chemical Physics*.

9.1 Introduction

Functionalised arylzinc compounds are of potential wide use in synthetic organic chemistry; however, their chemical synthesis typically involves multiple reagents and catalysts, volatile flammable solvents and long reaction times[1-5]. The

electrosynthesis of arylzinc compounds is limited to systems employing nickel or cobalt catalysts in various mixtures of acetonitrile, *N*,*N*-dimethylformamide and pyridine with various additives[6-8] and as such these electrochemical methods maintain most of the drawbacks of their chemical analogues.

Despite these drawbacks, there is no evidence in the literature that the electrochemical preparation of these compounds has been attempted in room temperature ionic liquids (RTILs). Room-temperature ionic liquids are highly advantageous when used as a solvent for electrosynthesis due to their low volatility[9] and flammability[10], high thermal stability[11], recyclability[12], large electrochemical windows[13] and intrinsic conductivity[13], removing the need for added supporting electrolyte. Importantly, RTILs are also able to stabilise otherwise reactive compounds and intermediates which cannot be easily investigated using conventional aprotic solvents[14], as well as strongly influence the reactivity of radical anions[15-17].

As stated in Chapter 1, microelectrodes are well suited to investigating both heterogeneous and homogeneous processes in room temperature ionic liquids. In Chapter 8, it was demonstrated that electrochemically formed 1-bromo-4-nitrobenzene radical anions (*p*-$BrC_6H_4NO_2^{\bullet-}$) generated using a *platinum* electrode exhibited a changed solution-phase reactivity in the $[C_4mPyrr][NTf_2]$ room-temperature ionic liquid, compared to conventional aprotic molecular solvents[16]. This resulted in debromination of the radical anions in the absence of light as a result of the better solvation and stabilisation of the bromide anion by the RTIL.

In the following, the changed reactivity of *p*-$BrC_6H_4NO_2$ in the $[C_4mPyrr][NTf_2]$ ionic liquid is exploited, *via* reduction at *zinc* microelectrodes in order to provide proof-of-concept of the formation of arylzinc compounds.

9.2 Experimental

Electrochemical measurements were performed in a thermostated (25.0 ± 0.1 °C) Faraday cage, using a μAutolab Type III computer-controlled potentiostat (Ecochemie). All measurements were obtained using a standard three electrode setup, utilising a platinum wire (99.9%, Goodfellow) counter electrode and Ag/Ag^+ reference electrode (see below). The working electrodes used were platinum (Pt, r = 5.45 μm, BASi) and zinc (Zn, $r \approx 12.5$ μm) microelectrodes. The preparation of the zinc microelectrodes was previously described in Chapter 7. Prior to use the working electrodes were polished using 1, 0.3 and 0.05 μm alumina lapping compounds (Buehler) on soft lapping pads (Buehler) and were then placed in EtOH in an ultrasonic bath for ~2 minutes to remove any adsorbed material. The working electrode was then further rinsed with EtOH and dried using compressed nitrogen. Before use, the counter electrode was cleaned in a hot Bunsen flame before being rinsed thoroughly with MeCN.

The Ag/Ag^+ reference electrode was prepared as described previously, by attaching a 5Å, 1.6mm diameter molecular sieve (Aldrich) to the end of a cut-down glass Pasteur pipette using PTFE heatshrink (TE Connectivity). The

Ag/Ag^+ reference electrode was then filled with a 20 mM solution of Ag[OTf] in $[C_4mPyrr][NTf_2]$ and a silver wire was immersed in the solution.

Experiments were prepared by placing 50 μL of sample solution into a small chamber on top of the working electrode, constructed by attaching a section of disposable micropipette tip over the electrode tip. The working electrode and sample were then placed into a glass T-shaped cell, described previously, and the counter and reference electrodes fed into the sample from above. One arm of the T-shaped cell was then connected to a rotary vacuum pump and the sample was placed under vacuum ($P = 0.018 \pm 0.002$ mbar) for at least 3 hours before measurement and remained *in-vacuo* for the duration of the experiment. It is highly desirable for ionic liquid systems to be studied *in-vacuo* to reduce the water[22] and oxygen[23] concentrations in the RTIL to acceptably low levels. Moreover, several gasses which were previously thought to be electrochemically benign, such as argon, nitrogen and carbon dioxide, have since been shown to alter the mass transport properties of RTILs[23-25]. Prior to first use it was necessary to activate the Zn microelectrode by scanning to from 0 to -3.2 V *vs.* the Ag/Ag^+ reference to remove a passivating film. Following *in-vacuo* experiments, the atmosphere inside the cell was switched to flow 200 ± 10 cm^3 min^{-1} CO_2 over the sample for at least 30 minutes prior to measurements and maintained throughout the experiment. Cyclic voltammograms (CVs) were filtered using an FFT function, within the GPES software, to remove high frequency electrical noise.

9.3 Results and Discussion

Electrochemical reduction of *p*-$BrC_6H_4NO_2$ in $[C_4mPyrr][NTf_2]$ under vacuum

A 13.5 mM solution of *p*-$BrC_6H_4NO_2$ in $[C_4mPyrr][NTf_2]$ was placed under vacuum for 3 hours to remove water and dissolved gasses[22, 23]. Cyclic voltammograms (CVs) were then measured for the reduction of *p*-$BrC_6H_4NO_2$ in the ionic liquid at the zinc microelectrode.

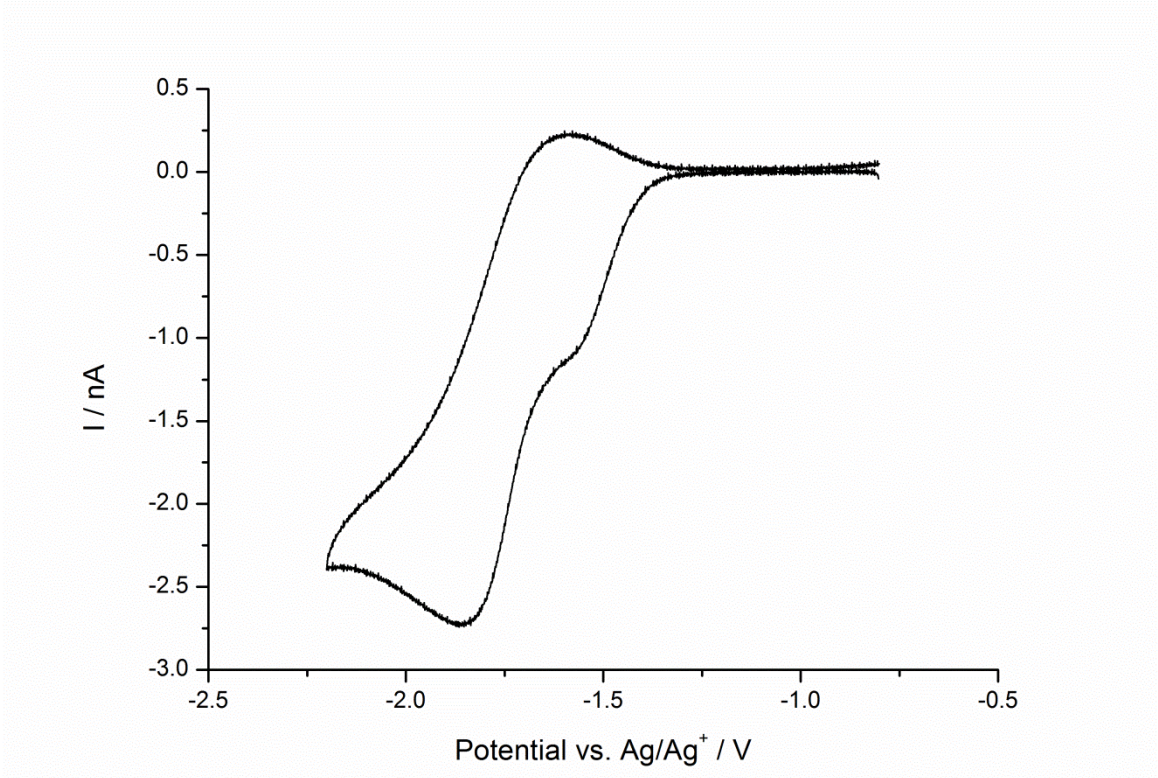


Figure 33 - Cyclic voltammogram of 13.5 mM *p*-$BrC_6H_4NO_2$ in $[C_4mPyrr][NTf_2]$ on a Zn microelectrode (r = 12.5 μm) at a scan rate of 100 mV s^{-1}.

Figure 33 shows a CV of 13.5 mM *p*-$BrC_6H_4NO_2$ in $[C_4mPyrr][NTf_2]$, measured at 100 mV s^{-1}, with the potential scanned from -0.8 to -2.2 V. The CV shows reduction and oxidation peaks at -1.86 and -1.59 V *vs.* the Ag/Ag^+ reference, respectively. Also evident in the voltammogram is a shoulder on the reduction

wave, which suggests possible adsorption of the *p*-$BrC_6H_4NO_2$ radical anion at the electrode surface, which was observed for *p*-$BrC_6H_4NO_2$ in [C_4mPyrr][NTf_2] for platinum microelectrodes in Chapter 8. As the scan rate is increased, shown in Figure 34, this adsorption process is kinetically disfavoured and thus the shoulder on the reduction wave is no longer observed.

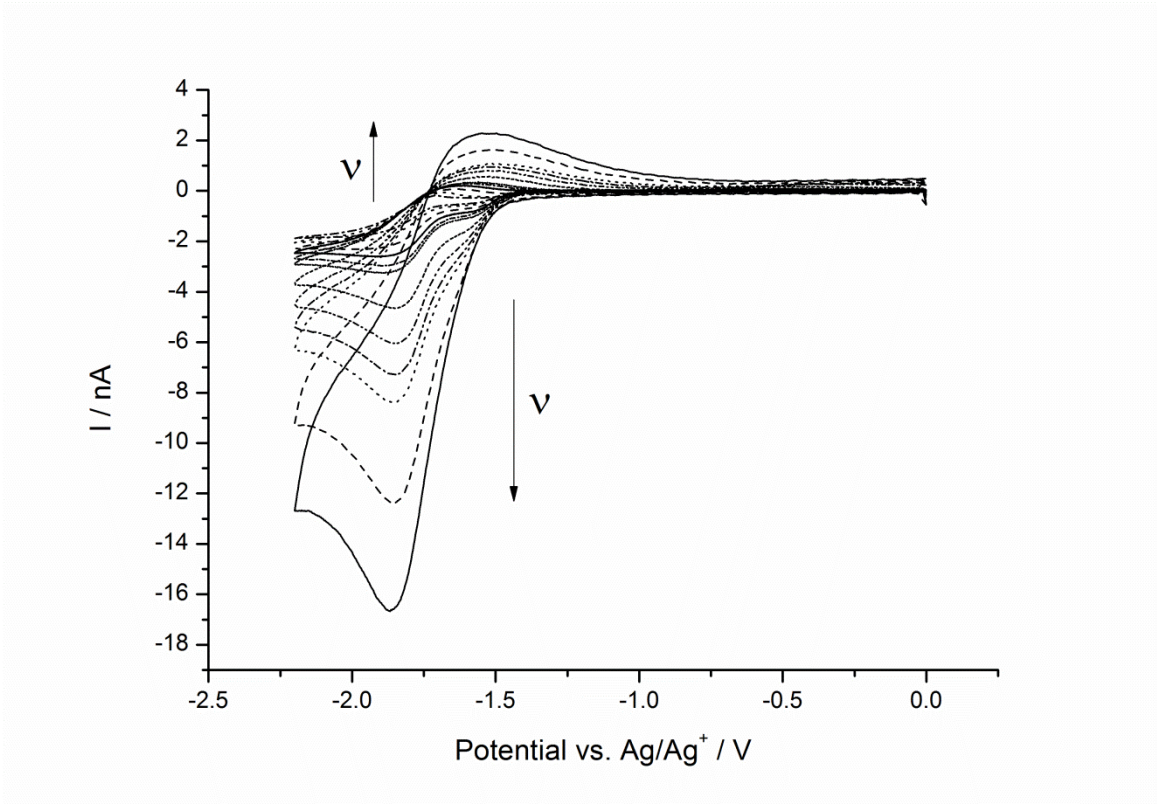


Figure 34 - Cyclic voltammograms of 13.5 mM *p*-$BrC_6H_4NO_2$ in [C_4mPyrr][NTf_2] on a Zn microelectrode (r = 12.5 μm) at scan rates of 5, 10, 25, 50, 75, 100, 250, 500, 750, 1000, 2500 and 5000 mV s^{-1}.

In contrast to the voltammetry of *p*-$BrC_6H_4NO_2$ in [C_4mPyrr][NTf_2] at Pt microelectrodes (see Chapter 8), the CVs on Zn show a significantly smaller backpeak. As the diffusion coefficients of *p*-$BrC_6H_4NO_2$ and its radical anion would be unchanged between the two experiments, this smaller than expected

backpeak may be resultant of either slower kinetics on zinc and/or a change in mechanism with respect to that on platinum.

However, the observed decrease in the electron transfer kinetics on the zinc electrode, as evidenced by the increase in peak-to-peak separation with respect to Pt (peak to peak separation at 1 V s^{-1} = 319 mV on Zn & 87 mV on Pt), cannot account for the observed decrease in the magnitude of the backpeak, as one electron simulations using software described previously[26] showed that fits yielding the measured peak-to-peak separation resulted in a significantly larger backpeak than that measured experimentally.

Consequently, the alteration of the backpeak must likely in part be ascribed to the consumption of the reduced product. This is most probably related to the formation of arylzinc species and the proposed mechanism is thus an EC-type mechanism where;

$$p\text{-}BrC_6H_4NO_2 + e^- \rightleftharpoons \left[p\text{-}BrC_6H_4NO_2\right]^{\bullet -} \tag{9.1}$$

$$2\left[p\text{-}BrC_6H_4NO_2\right]^{\bullet -} + Zn \rightleftharpoons \text{Products} \tag{9.2}$$

where the reduction of p-$BrC_6H_4NO_2$ is electrochemically quasi-reversible, forming the p-$BrC_6H_4NO_2^{\bullet -}$ radical anion, and the follow-up chemical reaction removes p-$BrC_6H_4NO_2^{\bullet -}$ from the diffusion layer, accounting for the decreased backpeak with respect to that observed on platinum[16]. The products may include $BrZn(C_6H_4NO_2)$ and/or $Zn(C_6H_4NO_2)_2$ and bromide ions.

9. Reduction of 1-Bromo-4-nitrobenzene at Zinc Microelectrodes

It was shown in Chapter 8 that the reduction of *p*-$BrC_6H_4NO_2$ in $[C_4mPyrr][NTf_2]$ at *platinum* microelectrodes proceeds *via* a DISP-type mechanism;

$$p\text{-}BrC_6H_4NO_2 + e^- \rightleftharpoons \left[p\text{-}BrC_6H_4NO_2\right]^{\bullet -} \tag{9.3}$$

$$\left[p\text{-}BrC_6H_4NO_2\right]^{\bullet -} + HS \xrightarrow{\text{slow}} C_6H_5NO_2 + S^{\bullet} + Br^- \tag{9.4}$$

$$\left[p\text{-}BrC_6H_4NO_2\right]^{\bullet -} + C_6H_5NO_2 \overset{\text{fast}}{\rightleftharpoons} p\text{-}BrC_6H_4NO_2 + C_6H_5NO_2^{\bullet -} \tag{9.5}$$

where HS refers to the solvent system. As the system under study is the same as that used in the work on platinum, this DISP-type mechanism cannot be neglected and as such a combination of the two mechanisms likely occur, with the rate constants of the chemical steps controlling their relative proportions.

Electrochemical reduction of *p*-$BrC_6H_4NO_2$ in $[C_4mPyrr][NTf_2]$ under CO_2

In order to chemically 'trap' the arylzinc species likely formed in (9.2)[27, 28], CO_2 was added to the cell such that;

$$Zn(C_6H_4NO_2)_2 + 2CO_2 \rightarrow Zn^{2+} + 2O_2NC_6H_4COO^- \tag{9.6}$$

or

$$BrZn(C_6H_4NO_2) + CO_2 \rightarrow ZnBr^+ + O_2NC_6H_4COO^- \tag{9.7}$$

The Zn^{2+} released in (9.6)/(9.7) will then be reduced to zinc at the electrode surface, as the potentials of *p*-$BrC_6H_4NO_2$ reduction are significantly negative of those required for Zn^{2+} reduction[29], *via*;

$$Zn^{2+}_{(RTIL)} + e^- \xrightarrow{slow} Zn^{+}_{(ads/RTIL)} \tag{9.8}$$

$$Zn^{+}_{(ads/RTIL)} + e^- \rightleftharpoons Zn_{(s)} \tag{9.9}$$

where the subscripts (ads), (RTIL) and (s) refer to the adsorbed, solvated and solid states, respectively. The following section thus examines the effects of changing the atmosphere in the cell from vacuum to CO_2.

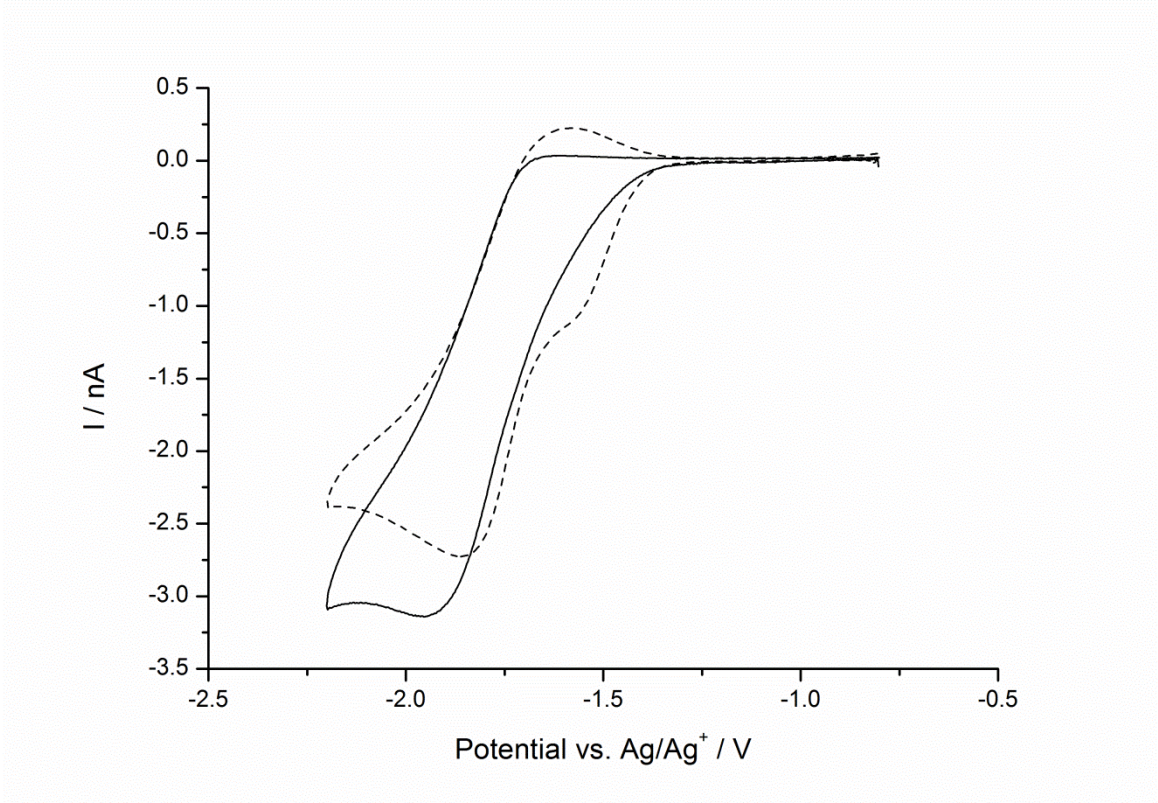


Figure 35 - Cyclic voltammograms of 13.5 mM *p*-$BrC_6H_4NO_2$ in $[C_4mPyrr][NTf_2]$ on a Zn microelectrode (r = 12.5 μm) at a scan rate of 100 mV s^{-1} under both vacuum (dotted line) and CO_2 (solid line) atmospheres.

The atmosphere in the cell was switched from vacuum conditions (0.018 ± 0.002 mbar) to a flow of 200 ± 10 cm^3 min^{-1} CO_2. This flow rate was maintained for at least 30 minutes prior to, as well as during, measurements. Figure 35 shows

the voltammetry of 13.5 mM *p*-$BrC_6H_4NO_2$ in [C_4mPyrr][NTf_2], measured at 100 mV s^{-1} with the potential scanned from -0.8 to -2.2 V, under both vacuum and CO_2 atmospheres.

Figure 35 shows that 30 minutes under a CO_2 atmosphere is sufficient for almost complete loss of the backpeak. Therefore, the addition of CO_2 to the system irreversibly traps the arylzinc species formed in (9.2), driving the reaction to favour the products and thus there is significantly less *p*-$BrC_6H_4NO_2^{\bullet-}$ in the diffusion layer to oxidise back to *p*-$BrC_6H_4NO_2$ on the reverse sweep. Furthermore, the peak potential under CO_2 is shifted to a more negative potential and the reduction currents are increased. The former is partly due to the loss of the adsorption feature, but the latter is due to the reduction of Zn(II) formed in (9.6)/(9.7). It should be noted, that while it has been reported[24] that dissolved CO_2 can lead to increased diffusion coefficients in RTILs, control experiments at a 5.45 μm platinum electrode, shown below in Figure 36, demonstrate that the increase in reduction currents related purely to diffusional effects is minimal, even after 2 hours. Importantly, the control experiment at the platinum microelectrode also shows that the addition of CO_2 to the system does *not* lead to the loss of the backpeak at the platinum electrode.

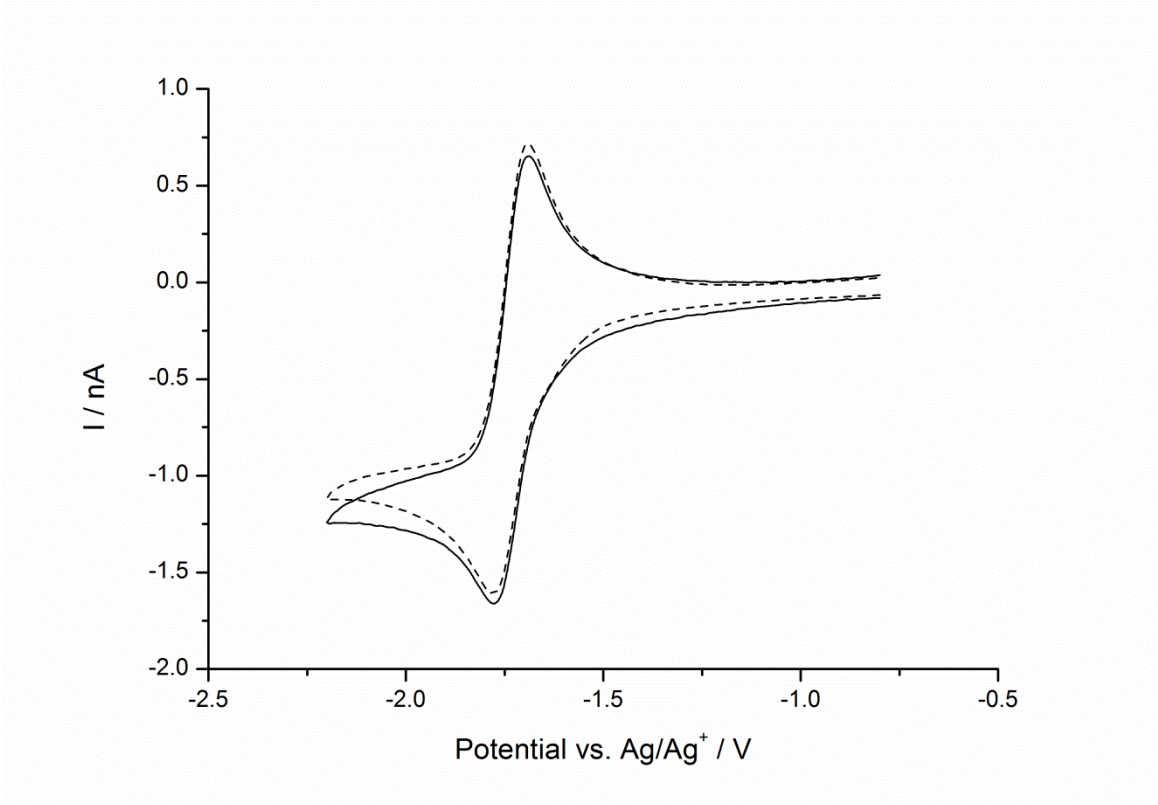


Figure 36 - Cyclic voltammograms of 13.5 mM *p*-$BrC_6H_4NO_2$ in [C_4mPyrr][NTf_2] at a 5.45 μm Pt microelectrode at a scan rate of 1 V s^{-1} under both vacuum (dotted line) and CO_2 (solid line) atmospheres.

It has thus been demonstrated in this work that the reduction of *p*-$BrC_6H_4NO_2$ at zinc electrodes in [C_4mPyrr][NTf_2] occurs *via* an EC-type mechanism in which the *p*-$BrC_6H_4NO_2$ is reduced quasi-reversibly by one electron to form the corresponding radical anion, which then reacts with the zinc electrode surface to form the corresponding arylzinc species. The addition of CO_2 to the cell then traps the arylzinc species.

9.4 Conclusions

The reduction of p-$BrC_6H_4NO_2$ was studied at Zn microelectrodes in the $[C_4mPyrr][NTf_2]$ ionic liquid *via* cyclic voltammetry. The reduction was found to occur *via* an EC-type mechanism, where p-$BrC_6H_4NO_2$ is reduced by one electron to yield the radical anion, which then reacts with the Zn electrode to form arylzinc products. Upon switching the atmosphere in the cell from vacuum to carbon dioxide, the backpeak was found to decrease as the carbon dioxide traps the arylzinc species, likely forming the deprotonated 4-nitrobenzoic acid and Zn^{2+}, which is then also reduced. This method thus demonstrates a proof-of-concept of the formation of functionalised arylzinc species without the need for supporting electrolytes or additional catalysts.

References

1. F. F. Kneisel, M. Dochnahl and P. Knochel, *Angewandte Chemie International Edition*, 2004, 43, 1017-1021.
2. L.-Z. Gong and P. Knochel, *Synlett*, 2005, 2005, 267-270.
3. K. Abiraj, G. R. Srinivasa and D. C. Gowda, *Synlett*, 2004, 2004, 0877-0879.
4. F. F. Kneisel, H. Leuser and P. Knochel, *Synthesis*, 2005, 2005, 2625-2629.
5. H. Fillon, C. Gosmini and J. Périchon, *Journal of the American Chemical Society*, 2003, 125, 3867-3870.
6. S. Sibille, V. Ratovelomanana and J. Perichon, *Journal of the Chemical Society, Chemical Communications*, 1992, DOI: 10.1039/c39920000283, 283-284.
7. C. Gosmini, Y. Rollin, J. Y. Nédélec and J. Périchon, *The Journal of Organic Chemistry*, 2000, 65, 6024-6026.
8. H. Fillon, E. Le Gall, C. Gosmini and J. Périchon, *Tetrahedron Letters*, 2002, 43, 5941-5944.
9. M. J. Earle, J. M. S. S. Esperança, M. A. Gilea, J. N. C. Lopes, L. P. N. Rebelo, J. W. Magee, K. R. Seddon and J. A. Widegren, *Nature*, 2006, 439, 831-834.
10. R. S. Kühnel, N. Böckenfeld, S. Passerini, M. Winter and A. Balducci, *Electrochimica Acta*, 2011, 56, 4092-4099.
11. C. Maton, N. De Vos and C. V. Stevens, *Chemical Society Reviews*, 2013, 42, 5963-5977.
12. Z.-L. Shen, S.-J. Ji and T.-P. Loh, *Tetrahedron Letters*, 2005, 46, 3137-3139.
13. D. R. MacFarlane, P. Meakin, J. Sun, N. Amini and M. Forsyth, *The Journal of Physical Chemistry B*, 1999, 103, 4164-4170.
14. D. S. Silvester, L. Aldous, M. C. Lagunas, C. Hardacre and R. G. Compton, *Journal of Physical Chemistry B*, 2006, 110, 22035-22042.
15. F. Andre, P. Hapiot and C. Lagrost, *Physical Chemistry Chemical Physics*, 2010, 12, 7506-7512.

16. S. Ernst, K. R. Ward, S. E. Norman, C. Hardacre and R. G. Compton, *Physical Chemistry Chemical Physics*, 2013, 15, 6382-6389.
17. C. Lagrost, S. Gmouh, M. Vaultier and P. Hapiot, *The Journal of Physical Chemistry A*, 2004, 108, 6175-6182.
18. J. Heinze, *Angewandte Chemie International Edition in English*, 1991, 30, 170-171.
19. P. Hapiot and C. Lagrost, *Chemical Reviews*, 2008, 108, 2238-2264.
20. M. I. Montenegro, *Res. Chem. Kinet.*, 1994, 2, 1-80.
21. Q. Shi, J. L. J. Rendek, W.-B. Cai and D. A. Scherson, *Electrochemical and Solid-State Letters*, 2003, 6, E35-E39.
22. A. M. O'Mahony, D. S. Silvester, L. Aldous, C. Hardacre and R. G. Compton, *Journal of Chemical and Engineering Data*, 2008, 53, 2884-2891.
23. C. Zhao, A. M. Bond, R. G. Compton, A. M. O'Mahony and E. I. Rogers, *Analytical Chemistry*, 2010, 82, 3856-3861.
24. L. E. Barrosse-Antle, C. Hardacre and R. G. Compton, *The Journal of Physical Chemistry B*, 2009, 113, 2805-2809.
25. L. E. Barrosse-Antle, L. Aldous, C. Hardacre, A. M. Bond and R. G. Compton, *The Journal of Physical Chemistry C*, 2009, 113, 7750-7754.
26. E. O. Barnes, A. M. O'Mahony, S. R. Belding and R. G. Compton, *Journal of Chemical & Engineering Data*, 2009, 55, 2219-2224.
27. K. Kobayashi and Y. Kondo, *Organic Letters*, 2009, 11, 2035-2037.
28. Y. Tsuji and T. Fujihara, *Chemical Communications*, 2012, 48, 9956-9964.
29. S. Ernst, M. Henstridge and R. Compton, *J Solid State Electrochem*, 2012, 16, 2329-2333.

Overall Conclusions

The work presented in this thesis has examined the electrochemical behaviour of a number of species, both surface-bound and in the solution phase, in various room-temperature ionic liquids, in order to identify systems which show altered reactivities in room-temperature ionic liquids, compared to that in conventional, molecular, aprotic solvents.

The fact that the size of ionic liquid ions can markedly affect the voltammetric response of surface-bound species was demonstrated. The electroactivity of anthraquinonyl films in RTILs was strongly correlated with the size of the RTIL cation, such that the $AQ_L^{\bullet-}|AQ_L^{2-}$ redox process became increasingly suppressed with increasing cation size. Steric hindrance of additional cations prevented charge compensation and hence inhibited the electroactivity of the film. This demonstrated that the RTIL plays a critical role in controlling the voltammetric response of surface-immobilised species.

Beyond the role of the RTIL on the electrochemical response, the influence of electrode material was also investigated, by studying the reduction of O_2 on boron-doped diamond and glassy carbon electrodes in the $[C_2mim][NTf_2]$ ionic liquid. The reduction of oxygen at the boron-doped diamond was found to predominantly involve the one electron reduction of oxygen to superoxide and this was verified by repeating the reduction on BDD in the presence of benzoic acid, with a resultant decrease in the superoxide oxidation peak and increase in the

peaks ascribed to the oxidation of hydroperoxyl species. The reduction of oxygen was found to be quasi-reversible on glassy carbon (ΔE_{pp} = 0.12 V) and irreversible on boron-doped diamond (ΔE_{pp} = 1.39 V), with electron transfer coefficients (α) of 0.39 and 0.13, respectively. The significantly slower kinetics observed on the boron-doped diamond electrode were related to the lower electronic density of states of BDD around the formal potential of O_2 reduction in $[C_2mim][NTf_2]$.

Having evaluated the nature of both the ionic liquid solvent and the working electrode, the electrodeposition and stripping of the $Zn^{2+}|Zn$ couple onto and from a bulk zinc deposit on a glassy carbon electrode was investigated in the $[C_4mPyrr][NTf_2]$ ionic liquid and it was shown that the electrochemical stripping mechanism was dependant on the applied overpotential. The electrodeposition of Zn was found to occur *via* an EE or ECE mechanism with the first step being rate determining. Close to the formal potential, the electrochemical stripping of Zn occurs *via* an EE or ECE mechanism with a rate determining first step, however, at more positive potentials a chemical step occurring after the initial electron transfer becomes rate limiting and hence the mechanism shifts to an ECE form.

Having investigated the electrodeposition and stripping of Zn(II) at glassy carbon electrodes in the $[C_4mPyrr][NTf_2]$ ionic liquid, a novel technique was successfully developed for the fabrication of zinc microdisk electrodes from commercially available zinc wire. The voltammetry of the fabricated zinc microdisk electrodes was compared with that observed in aqueous KOH solutions

for single zinc microparticles and zinc macroelectrodes, with good agreement being observed. The voltammetry of the zinc microdisk electrodes was also compared to that obtained for the deposition of Zn^{2+} at glassy carbon electrodes and, apart from an extra peak associated with the reduction of an intermediate, similar behaviour was observed. The zinc microdisk electrodes were prepared in order to study the electrochemical reduction of functionalised benzenes as a route towards the electrochemical synthesis of arylzinc compounds. However, it was first desirable to evaluate the voltammetric behaviour of several of these compounds at inert platinum microelectrodes.

The reductions of $C_6H_5NO_2$, C_6H_5Br and *p*-$BrC_6H_4NO_2$ were thus studied in the $[C_4mPyrr][NTf_2]$ ionic liquid, at platinum microelectrodes, *via* cyclic voltammetry, chronoamperometry and voltammetric simulation. $C_6H_5NO_2$ was found to be reduced *via* a one-electron mechanism to form the stable radical anion, analogous to the behaviour in a range of aprotic solvents. The reduction of C_6H_5Br was found to occur at potentials negative to those of $C_6H_5NO_2$ and multiple scans were found to modify the electrode surface. The reduction of *p*-$BrC_6H_4NO_2$ was shown to proceed *via* a DISP type mechanism, in which the parent molecule is reduced by one electron to form the anion radical, at which point debromination occurs in a rate-determining chemical step involving the fast scavenging of a hydrogen atom from the solvent system to yield nitrobenzene, which is then reduced to its radical anion. This shows significant contrast to the behaviour observed in conventional non-aqueous solvents as the debromination was observed in the absence of light.

Overall Conclusions

Thus, it was shown that the *p*-$BrC_6H_4NO_2$ radical anion exhibits a changed reactivity in the [C_4mPyrr][NTf_2] ionic liquid compared to molecular non-aqueous solvents, which was rationalised in terms of much better solvation and stabilisation of the bromide anion in the RTIL as coordination with the RTIL cation is highly favoured.

The reduction of p-$BrC_6H_4NO_2$ was then studied at Zn microelectrodes in the [C_4mPyrr][NTf_2] ionic liquid, *via* cyclic voltammetry. The reduction was found to occur *via* an EC-type mechanism, where p-$BrC_6H_4NO_2$ is reduced by one electron to yield the radical anion, which then reacts with the Zn electrode to form arylzinc products. These arylzinc species were then 'trapped' with CO_2, likely forming the deprotonated 4-nitrobenzoic acid and Zn^{2+}, which is then also reduced. This method thus demonstrated a proof-of-concept of the formation of functionalised arylzinc species without the need for supporting electrolytes or additional catalysts.

Overall, it has been shown in this thesis that the oft-taken view that the reactivity of a given species in an ionic liquid will mimic that in conventional aprotic solvents is not always the case. Reactivities can be markedly different between RTILs and aprotic solvents and can also be highly dependent on the specific ionic liquid employed. These observations show that further investigations to probe the altered reactivity of electrochemical systems in room-temperature ionic liquids have the potential to discover novel and widely applicable chemistry.

Appendix

This appendix presents the derivations of some key equations used within this thesis.

Derivation of Fick's Laws

In order to derive Fick's first law, in one dimension, we initially consider the diffusive flux, j_d (mol m^{-2} s^{-1}), of a material moving through a fixed volume of area A (m^2) and length x (m), in response to an arbitrary concentration gradient at time t. In order to achieve this, we acknowledge that at two distinct distances, x = x and x = x + δx, there are a certain number of molecules $N_{(x)}$ and $N_{(x + \delta x)}$, respectively. Given that the molecules in these two terms are equally likely to move, *via* Brownian motion, in the x and $-x$ directions, the net flux through the point x is given by;

$$j_d = \frac{1}{A} \frac{\frac{N_{(x)}}{2} - \frac{N_{(x+\delta x)}}{2}}{\delta t} \tag{11.1}$$

Multiplying the right hand side of (11.1) by $\delta x^2 \,/\, \delta x^2$ then yields;

$$j_d = \frac{\delta x^2}{2A\delta x^2} \frac{N_{(x)} - N_{(x+\delta x)}}{\delta t} \tag{11.2}$$

As the concentration, c, is given by $c = N \,/\, A\delta x$, (11.2) becomes;

$$j_d = \frac{\delta x^2}{2\delta x} \frac{c_{(x)} - c_{(x+\Delta x)}}{\delta t} \tag{11.3}$$

which, upon rearranging yields;

$$j_{\mathrm{d}} = -\frac{\delta x^2}{2\delta t}\frac{c_{(\mathrm{x}+\delta\mathrm{x})} - c_{(\mathrm{x})}}{\delta x} \tag{11.4}$$

As the diffusion coefficient, D, (in one dimension) is defined as $\delta x^2 \,/\, 2\delta t$, (11.4) simplifies to;

$$j_{\mathrm{d}} = -D\frac{c_{(\mathrm{x}+\delta\mathrm{x})} - c_{(\mathrm{x})}}{\delta x} \tag{11.5}$$

which, in the limit of $(\delta x, \delta t) \rightarrow (0,0)$, yields;

$$j_{\mathrm{d}} = -D\frac{\partial c}{\partial x} \tag{11.6}$$

which is Fick's first law.

Fick's second law compliments (11.6) by considering the change in concentration of a species with respect to time. We initially consider that the change in concentration at position x, with respect to time, is a combination of the flux into and out of an arbitrarily small element of length dx, such that;

$$\frac{\partial c}{\partial t} = \frac{j_{(x)} - j_{(x+dx)}}{dx} \tag{11.7}$$

The flux at point $x + dx$ can be expressed in terms of the flux at x *via*;

$$j_{(x+dx)} = j_{(x)} + \frac{\partial j_{(x)}}{\partial x}dx \tag{11.8}$$

which, when substituted into (11.7) yields;

$$\frac{\partial c}{\partial t} = \frac{j_{(x)} - \left(j_{(x)} + \dfrac{\partial j_{(x)}}{\partial x} dx \right)}{dx} \tag{11.9}$$

which simplifies to;

$$\frac{\partial c}{\partial t} = -\frac{\partial j_{(x)}}{\partial x} \tag{11.10}$$

the right hand side of which is simply the spatial partial derivative of Fick's first law, (11.6), such that;

$$\frac{\partial c}{\partial t} = -\frac{\partial}{\partial x}\left(-D \frac{\partial c}{\partial x} \right) \tag{11.11}$$

which, assuming D is not dependant on x, simplifies to;

$$\frac{\partial c}{\partial t} = D \frac{\partial^2 c}{\partial x^2} \tag{11.12}$$

which is Fick's second law.

In three dimensions, (11.12) is represented as;

$$\frac{\partial c}{\partial t} = D \cdot \nabla^2 c \tag{11.13}$$

where ∇^2 is the Laplacian operator for the second differential and depends on the coordinate system used.

Derivation of the Nernst Equation

In order to derive the Nernst equation, we first consider that for a given redox reaction the maximum electric work, W, is related to the applied potential, E, *via*;

$$W = qE \tag{11.14}$$

where q is the electrical charge passed. By definition, the Gibb's energy, ΔG, is equal to the negative value of the maximum electric work, such that;

$$\Delta G = -qE \tag{11.15}$$

The charge passed for a given redox reaction is given by;

$$q = nF \tag{11.16}$$

where n is the number of electrons transferred in the reaction and F is the Faraday constant, which represents the charge of one mole of electrons. Substituting (11.16) into (11.15) then leads to;

$$\Delta G = -nFE \tag{11.17}$$

which, under standard conditions, becomes;

$$\Delta G^{\circ} = -nFE^{\circ} \tag{11.18}$$

Given that;

$$\Delta G = \Delta G^{\circ} + RT \ln Q \tag{11.19}$$

where R is the universal gas constant, T the temperature and Q the reaction quotient which, for the reaction;

$$\mathrm{aA} + \mathrm{bB} \rightleftharpoons \mathrm{cC} + \mathrm{dD} \tag{11.20}$$

is given by the product of the activities of each component, such that;

$$Q = \frac{a_{\mathrm{C}}^{\mathrm{c}} a_{\mathrm{D}}^{\mathrm{d}}}{a_{\mathrm{A}}^{\mathrm{a}} a_{\mathrm{B}}^{\mathrm{b}}} \tag{11.21}$$

where the activities, a_j, are related to the concentrations, $[j]$, by the so-called 'activity coefficient, γ_j, such that;

$$a_j = \gamma_j [j] \tag{11.22}$$

Substituting (11.17) and (11.18) into (11.19) then yields;

$$-nFE = -nFE^{\circ} + RT \ln\left(\frac{a_{\mathrm{C}}^{\mathrm{c}} a_{\mathrm{D}}^{\mathrm{d}}}{a_{\mathrm{A}}^{\mathrm{a}} a_{\mathrm{B}}^{\mathrm{b}}}\right) \tag{11.23}$$

which can be simplified to;

$$E = E^{\circ} + \frac{RT}{nF} \ln\left(\frac{a_{\mathrm{A}}^{\mathrm{a}} a_{\mathrm{B}}^{\mathrm{b}}}{a_{\mathrm{C}}^{\mathrm{c}} a_{\mathrm{D}}^{\mathrm{d}}}\right) \tag{11.24}$$

which is the Nernst equation. However, in electrochemical experiments, it is common to work with solutions of high ionic strength. Consequently, during the electrochemical experiment, the activity coefficients will effectively be constant.

As such, these may be combined with the standard potential to give the so-called 'formal potential', E_f°. Equation (11.24) then becomes;

$$E = E_f^\circ + \frac{RT}{nF}\ln\left(\frac{[\mathrm{A}]^{\mathrm{a}}[\mathrm{B}]^{\mathrm{b}}}{[\mathrm{C}]^{\mathrm{c}}[\mathrm{D}]^{\mathrm{d}}}\right) \tag{11.25}$$

Finally, it should also be noted that it is often more convenient to work with decadal logs such that the Nernst equation is often written as;

$$E = E_f^\circ + \frac{2.303RT}{nF}\log\left(\frac{[\mathrm{A}]^{\mathrm{a}}[\mathrm{B}]^{\mathrm{b}}}{[\mathrm{C}]^{\mathrm{c}}[\mathrm{D}]^{\mathrm{d}}}\right) \tag{11.26}$$

Derivation of the Butler-Volmer Equation

In order to derive the Butler-Volmer equation, we first consider that the net rate, R, of the reaction;

$$\mathrm{A} + \mathrm{e}^- \underset{k_b}{\overset{k_f}{\rightleftharpoons}} \mathrm{B} \tag{11.27}$$

depends on both the forward, k_f, and backward, k_b, rate constants, such that;

$$R = k_f[\mathrm{A}] - k_b[\mathrm{B}] \tag{11.28}$$

where the concentration terms describe the surface concentrations of A and B. As the net rate of reaction can also be described in terms of the electrons transferred we can state that;

$$\frac{i}{FA} = k_f[\mathrm{A}] - k_b[\mathrm{B}] \tag{11.29}$$

and thus;

$$i = FA(k_f[\mathrm{A}] - k_b[\mathrm{B}]) \tag{11.30}$$

Under equilibrium conditions, the rates of the forward and backward reaction must be equal, such that;

$$k_f[\mathrm{A}] = k_b[\mathrm{B}] \tag{11.31}$$

Rearranging (11.31) and taking logarithms on both sides then gives;

$$\ln(k_b) - \ln(k_f) = \ln\left(\frac{[\mathrm{A}]}{[\mathrm{B}]}\right) \tag{11.32}$$

As the system is at equilibrium, we can rearrange the Nernst equation (11.24) to yield;

$$\ln\left(\frac{[\mathrm{A}]}{[\mathrm{B}]}\right) = \frac{F}{RT}(E - E^{\circ}) \tag{11.33}$$

Substituting (11.33) into (11.32) then gives;

$$\ln(k_b) - \ln(k_f) = \frac{F}{RT}(E - E^{\circ}) \tag{11.34}$$

which can then be rearranged such that;

$$\frac{RT}{F}\left(\ln(k_b) + \ln\left(\frac{1}{k_f}\right)\right) = E - E^{\circ} \tag{11.35}$$

Differentiating both sides with respect to E then yields;

Appendix

$$\frac{RT}{F}\left(\frac{d}{dE}\ln(k_b)+\frac{d}{dE}\ln\left(\frac{1}{k_f}\right)\right)=1 \tag{11.36}$$

where the two terms on the left hand side are called symmetry factors and are usually represented as;

$$\frac{RT}{F}\left(\frac{d}{dE}\ln\left(\frac{1}{k_f}\right)\right)=\alpha \tag{11.37}$$

$$\frac{RT}{F}\left(\frac{d}{dE}\ln(k_b)\right)=1-\alpha \quad (or\,\beta) \tag{11.38}$$

Integration of (11.37) then yields;

$$\ln\left(\frac{1}{k_f}\right)=\frac{\alpha F}{RT}E+\text{constant} \tag{11.39}$$

which, given (11.31), if $k_f=k_b=k^\circ$ at $E=E^\circ$, then leads to;

$$k_f=k^\circ\exp\left(-\frac{\alpha F}{RT}(E-E^\circ)\right) \tag{11.40}$$

$$k_b=k^\circ\exp\left(\frac{(1-\alpha)F}{RT}(E-E^\circ)\right) \tag{11.41}$$

Substituting (11.40) and (11.41) into (11.30) then yields;

$$i=FAk^\circ\left([\mathrm{A}]\exp\left(-\frac{\alpha F}{RT}(E-E^\circ)\right)-[\mathrm{B}]\exp\left(\frac{(1-\alpha)F}{RT}(E-E^\circ)\right)\right) \tag{11.42}$$

which is the Butler-Volmer equation.